

THESIS FOR THE DEGREE OF DOCTOR OF PHILOSOPHY

# Quantum Optics with Propagating Microwaves in Superconducting Circuits

IO-CHUN, HOI

(許耀銓)

Department of Microtechnology and Nanoscience  
CHALMERS UNIVERSITY OF TECHNOLOGY  
Göteborg, Sweden 2013

Quantum Optics with Propagating Microwaves in Superconducting Circuits  
IO-CHUN, HOI  
ISBN 978-91-7385-878-6

©IO-CHUN, HOI, 2013

Doktorsavhandlingar vid Chalmers tekniska högskola  
Ny serie nr 3559  
ISSN 0346-718X

Experimental Mesoscopic Physics Group  
Quantum Device Physics Laboratory  
Department of Microtechnology and Nanoscience - MC2  
Chalmers University of Technology  
SE-412 96 Göteborg, Sweden  
Telephone: +46 (0)31 - 772 1000

ISSN 1652-0769  
Technical Report MC2-242

Chalmers Reproservice  
Göteborg, Sweden 2013

Quantum Optics with Propagating Microwaves in Superconducting Circuits  
IO-CHUN, HOI  
Department of Microtechnology and Nanoscience  
Chalmers University of Technology, 2013

## Abstract

We address recent advances in quantum optics with propagating microwaves in superconducting circuits. This research field exploits on the fact that the coupling between a superconducting artificial atom and propagating microwave photons in a one-dimensional (1D) open transmission line can be made strong enough to observe quantum effects, *without* using any cavity to confine the microwave photons.

We embed an artificial atom, a superconducting transmon qubit, in a 1D open transmission line and investigate the scattering properties of coherent microwaves. When an input coherent state, with an average photon number much less than 1, is on resonance with the artificial atom, we observe extinction of up to 99% in the forward propagating field. We observe the strong nonlinearity of the artificial atom and under strong driving we observe the Mollow triplet. We also study the statistics of the reflected and transmitted beams, which are predicted to be non-classical states. In particular, we demonstrate photon antibunching in the reflected beam by measuring the second-order correlation function. By applying a second control tone, we observe the Autler-Townes splitting and a giant cross-Kerr effect. Furthermore, we demonstrate fast operation of a single-photon router using the Autler-Townes splitting. This device provides important steps towards the realization of a quantum network. This thesis describes the motivation, theoretical background, design, implementation and measurement results.

**Keywords:** quantum optics, microwave photons, superconducting circuits, superconducting artificial atom, qubit, Mollow triplet, antibunching, second-order correlation function, Autler-Townes splitting, cross-Kerr effect, photon router, quantum network, transmon, Josephson junction, SQUID.

## List of appended publications

**This thesis is based on the work contained in the following papers:**

**I: Demonstration of a single-photon router in the microwave regime.**

Io-Chun Hoi, C.M. Wilson, Göran Johansson, Tauno Palomaki, Borja Peropadre, Per Delsing  
Phys. Rev. Lett. 107, 073601 (2011)

**II: Generation of nonclassical microwave states using an artificial atom in 1D open space.**

Io-Chun Hoi, Tauno Palomaki, Göran Johansson, Joel Lindkvist, Per Delsing and C.M. Wilson  
Phys. Rev. Lett. 108, 263601 (2012)

**III: Giant cross-Kerr effect for propagating microwaves induced by an artificial atom.**

Io-Chun Hoi, Anton F. Kockum, Tauno Palomaki, Thomas M. Stace, Bixuan Fan, Lars Tornberg, Sankar R. Sathyamoorthy, Göran Johansson, Per Delsing and C.M. Wilson  
Phys. Rev. Lett. 111, 053601 (2013)

**IV: Microwave quantum optics with an artificial atom in one-dimensional open space.**

Io-Chun Hoi, C.M. Wilson, Göran Johansson, Joel Lindkvist, Borja Peropadre, Tauno Palomaki and Per Delsing  
New Journal of Physics 15, 025011 (2013)

**V: Scattering of coherent states on a single artificial atom.**

B. Peropadre, J. Lindkvist, I.-C. Hoi, C.M. Wilson, J. Garcia-Ripoll, P. Delsing and G. Johansson  
New Journal of Physics 15, 035009 (2013)

**VI: Breakdown of the cross-Kerr scheme for photon counting.**

Bixuan Fan, A.F. Kockum, J. Combes, G. Johansson, I.-C. Hoi, C. M. Wilson, P. Delsing, G. J. Milburn and T. M. Stace  
Phys. Rev. Lett. 110, 053601 (2013)

Other papers not included in this thesis:

**VII: Exploring circuit quantum electrodynamics using a widely tunable superconducting resonator.**

M. Sandberg, F. Persson, I.-C. Hoi, C.M. Wilson, and P. Delsing.  
Physica Scripta, T137, 014018 (2009)

**VIII: Coupling of an erbium spin ensemble to a superconducting resonator.**

M. U. Staudt, I.-C. Hoi, P. Krantz, M. Sandberg, M. Simoen, P. Bushev, N. Sangouard, M. Afzelius, V.S. Shumeiko, G. Johansson, P. Delsing, C. M. Wilson  
Journal of Physics B: Atomic, Molecular and Optical Physics, 45, 124019 (2012)

# Preface

Quantum optics is a science that investigates light-matter interactions. In the past few decades, impressive experimental techniques have enabled experiments where it is possible to address and manipulate individual atoms and photons. This led to the Nobel Prize in Physics 2012, “for ground-breaking experimental methods that enable measuring and manipulation of individual quantum systems”. The Nobel laureate Serge Haroche controlled the photons with Rydberg atom(s). The other Nobel laureate, David J. Wineland, did the opposite, manipulating ion(s) using laser light. In this thesis, I use a different approach to investigate atom-light interaction. In particular, I study the interaction of a single artificial atom and propagating microwave photons in a one-dimensional (1D) open waveguide based on superconducting circuits.

The thesis is organized in the following way. Chapter 1 is intended for non-expert readers. This chapter gives the reader an overview of the scientific background and motivation for the work. It includes a brief history of the research field and some important concepts. Chapter 2 describes the theory for the framework of the thesis: the interaction of an artificial atom and the propagating electromagnetic (EM) field in a 1D waveguide based on superconducting circuits. This includes a description of the superconducting artificial atom, as well as how to achieve strong coupling between the atom and the propagating field. I also discuss photon-photon interactions via a three-level atom and the second-order correlation of different microwave states. Chapter 3 describes the design that would allow strong coupling between the atom and the propagating field. Fabrication and measurement techniques will also be discussed. Chapter 4 shows the main experimental results, comparing to the theoretical predictions in chapter 2. Chapter 4 is divided into two sections. The first section investigates various quantum-optical effects with a single artificial atom in the microwave regime. The second section demonstrates quantum applications based on these effects. Chapter 5 gives the conclusion and suggestions for possible future work.

Io-Chun Hoi  
Gothenburg, August 2013



# Contents

<b>Abstract</b>	<b>iii</b>
<b>List of appended publications</b>	<b>iv</b>
<b>Preface</b>	<b>vi</b>
<b>1 Introduction and Motivation</b>	<b>1</b>
1.1 Quantum Computing . . . . .	1
1.2 Superconductivity and the Josephson Effect . . . . .	3
1.3 Quantum Optics with Superconducting Circuits . . . . .	5
1.4 Quantum Network . . . . .	8
<b>2 Theoretical Background</b>	<b>11</b>
2.1 Superconducting Artificial Atom . . . . .	11
2.1.1 The Single Cooper-Pair Box (SCB) . . . . .	14
2.1.2 The Transmon . . . . .	18
2.2 1D Coplanar Waveguide Transmission Line . . . . .	22
2.3 Interaction of a Two-Level Atom and EM Fields . . . . .	24
2.3.1 Dipole Coupling of a SCB . . . . .	24
2.3.2 A SCB in a 1D Open Transmission Line . . . . .	26
2.3.3 A SCB in a Quantized Field: Dressed States . . . . .	31
2.3.4 A SCB at the end of a 1D Transmission Line . . . . .	34
2.4 Interaction of Two EM Fields via a Three-Level Atom . . . . .	37
2.4.1 The Electromagnetically Induced Transparency . . . . .	40
2.4.2 The Cross-Kerr Effect . . . . .	40
2.4.3 Photon Detection with Cross-Kerr Scheme . . . . .	42
2.5 Second-Order Correlation . . . . .	43
2.5.1 Photon Statistics of Different Light Sources . . . . .	44
2.5.2 Antibunched and Superbunched States . . . . .	47

<b>3</b>	<b>Experimental Techniques</b>	<b>50</b>
3.1	Sample Design . . . . .	50
3.2	Fabrication . . . . .	52
3.3	Measurement Setup . . . . .	55
3.3.1	Microwaves . . . . .	55
3.3.2	Cryogenics . . . . .	58
<b>4</b>	<b>Experimental Results</b>	<b>60</b>
4.1	Quantum Optics with Propagating Microwaves . . . . .	60
4.1.1	Single-Atom Scattering . . . . .	60
4.1.2	Tunable Artificial Atom . . . . .	67
4.1.3	Mollow Triplet and Autler-Townes Splitting . . . . .	68
4.2	Quantum Applications at the Single-Photon Level . . . . .	72
4.2.1	The Single-Photon Router . . . . .	72
4.2.2	The Photon-Number Filter . . . . .	76
4.2.3	The Cross-Kerr Phase Shift . . . . .	81
<b>5</b>	<b>Conclusion and Future Work</b>	<b>87</b>
	<b>Appendix A: Symbols and Abbreviations</b>	<b>91</b>
	<b>Appendix B: Three-Level Rotating-Wave Approximation</b>	<b>96</b>
	<b>Appendix C: Deviation of <math>t</math> and <math>r</math> in Section 2.3.2</b>	<b>99</b>
	<b>Appendix D: <math>g^{(2)}</math> Measurements Using Linear Amplifiers</b>	<b>107</b>
	<b>Appendix E: Fabrication Recipe</b>	<b>111</b>
	<b>Appendix F: Calculations on Cross-Kerr Effect</b>	<b>113</b>
	<b>Acknowledgements</b>	<b>117</b>
	<b>Bibliography</b>	<b>118</b>
	<b>Appended Paper</b>	<b>129</b>

# Chapter 1

## Introduction and Motivation

In this chapter, I will give a background overview of the following sections: quantum computing, superconductivity and quantum optics with superconducting circuits. In each section, I will briefly illustrate the developments of the field and the main concepts. At the end, I will discuss the motivation of my work: building a quantum network with superconducting circuits.

### 1.1 Quantum Computing

The development of important concepts in quantum computing is briefly outlined in Table 1.1. Basically, a quantum computer (QC) could perform some specific computations (see Table 1.1) much faster than a classical computer since a quantum computer makes use of quantum resources, such as superposition (Fig. 1.1B) and entanglement to perform operations on data.

Year	Milestones
1982	Quantum computing was first mentioned by Richard Feynman [1]
1985	David Deutsch proved the existence of a universal QC [2]
1994	Shor shows the power of factorizing large integers with a QC [3]
1995	Shor shows the quantum error correction [4].
1996	Grover shows the power of searching unsorted data with a QC [5]
2000	DiVincenzo proposed criteria for the implementation of a QC [6]

*Table 1.1: Important concepts in quantum computing.*

The fundamental building block of a quantum computer is the quantum bit, qubit for short. In a quantum computer, it plays a role similar to that of a classical bit in an ordinary computer. A qubit is a two-level system, represented by two

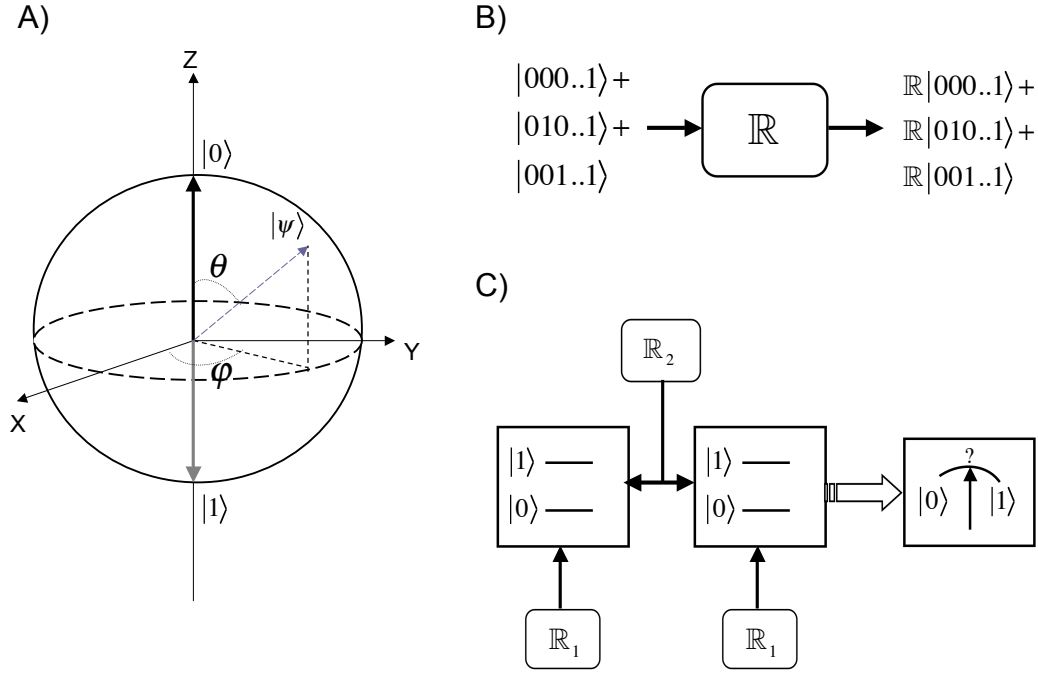


Figure 1.1: A) Bloch sphere. The north and south poles represent the ground and excited states, respectively. The state  $|\Psi\rangle$  is displayed on the Bloch sphere. B) The operator  $\mathbb{R}$  operates on every input states and provides massive parallelism. C) A quantum processor is made of coupled qubits, each qubit having a separate coherent control.  $\mathbb{R}_1$  and  $\mathbb{R}_2$  represent single-qubit and two-qubit gates, respectively. The state can be read out by a projective measurement.

orthogonal states denoted by  $|0\rangle, |1\rangle$ . The qubit can also be in a superposition of the two states [7],

$$|\Psi\rangle = \cos(\theta/2)e^{-i\varphi/2}|0\rangle + \sin(\theta/2)e^{i\varphi/2}|1\rangle. \quad (1.1)$$

The state  $|\Psi\rangle$  is described by a point on a unit sphere, called the Bloch sphere, in which  $\varphi, \theta$  are the angles defined in Fig. 1.1A. The standard model for a qubit is a spin 1/2 particle, with a magnetic moment  $\mu_{01}$ , in a magnetic field  $\vec{B} = (B_x, B_y, B_z)$ . The corresponding Hamiltonian [8] is

$$H = -\mu_{01}(B_x\sigma_x + B_y\sigma_y + B_z\sigma_z) = -\frac{\hbar}{2}(\omega_x\sigma_x + \omega_y\sigma_y + \omega_z\sigma_z), \quad (1.2)$$

where  $\sigma_i$  are the Pauli matrices and  $\omega_i = 2\mu_{01}B_i/\hbar$ ,  $i = x, y, z$ . Any two-level system can be described by Eq. (1.2), with an offset energy. The time evolution of the state  $|\Psi(t)\rangle$  is governed by the Schrödinger equation [8]. The state

$|\Psi\rangle$  precesses around the vector  $\vec{\omega} = (\omega_x, \omega_y, \omega_z)$ , with a frequency of  $|\vec{\omega}|$ . By changing the direction or strength of the magnetic field, arbitrary rotations can be performed, which act as single qubit gates. Coherent qubit manipulation is achieved by applying a nonadiabatic magnetic field pulse. The pulse strength and the pulse width determine the rotation angle. The state can then be read out by a projective measurement. By coupling multiple qubits, and realizing multi-qubits gates, a quantum processor can be realized (see Fig. 1.1C).

## 1.2 Superconductivity and the Josephson Effect

### Simple Picture

The discovery and development of superconductivity is briefly outlined in Table 1.2. To first order, superconductivity can be understood from the pairwise interaction between electrons. When a superconductor is cooled below its critical temperature  $T_c$ , an effective positive attraction between electrons, mediated by phonons, may dominate over the Coulomb repulsion. The electrons form pairs, known as Cooper pairs [9]. They condense into a collective ground state, described by one common macroscopic wave function,  $\Psi_s$ . The superconducting gap, denoted by  $\Delta_s$ , is the minimum energy required to break a Cooper pair.

Year	Milestones
1911	Zero resistance of mercury was discovered [10]
1933	Superconductor expelled applied magnetic fields (Meissner effect) [11]
1935	Meissner effect was phenomenologically described [12]
1957	Microscopic theory, known as BSC theory was established [9]
1962	Josephson Effect was discovered [13]
1986	High $T_c$ superconductor was discovered [14]

Table 1.2: Important discoveries in superconductivity.

### The Josephson Effect and the SQUID

A Josephson junction is a weak link between two superconductors [13, 15]. Often the superconductors are separated by a thin oxide barrier. The wavefunction of these two superconductors can interact or couple through the weak link. This interaction allows a Josephson current to pass through the barrier with no DC resistance. This current depends on the phase difference,  $\phi$ , between the two wave functions of the electrodes. The voltage drop across the junction,  $V$ , is related to

the time derivative of  $\phi$ . More specifically, we can write the dc Josephson equation and the ac Josephson equation, as follows [16]:

$$I = I_c \sin \phi; \quad \frac{d\phi}{dt} = \frac{2e}{\hbar} V. \quad (1.3)$$

Two Josephson junctions connected in a loop form a Superconducting Quantum Interference Device (SQUID) [17]. The phase difference of the two junctions depend on the externally applied flux,  $\Phi_{ext}$ . Assuming no other inductance in the loop, we have

$$\phi_2 - \phi_1 = 2\pi\Phi_{ext}/\Phi_0, \quad (1.4)$$

where  $\phi_i$  is the phase difference across each junction ( $i = 1, 2$ ) and  $\Phi_0 = h/(2e)$  is the flux quantum. The total current is the sum of the two supercurrents,

$$I = I_{c1} \sin \phi_1 + I_{c2} \sin \phi_2. \quad (1.5)$$

Together with Eq. (1.4), we can rewrite Eq. (1.5) in the following form,

$$I = (I_{c1} - I_{c2}) \sin(\pi\Phi_{ext}/\Phi_0) \cos \phi_s + (I_{c1} + I_{c2}) \cos(\pi\Phi_{ext}/\Phi_0) \sin \phi_s, \quad (1.6)$$

where  $\phi_s = (\phi_1 + \phi_2)/2$ . In the case of symmetric Josephson junctions, where  $I_{c1} = I_{c2} = I_c$ , Eq. (1.6) becomes

$$I = 2I_c |\cos(\pi\Phi_{ext}/\Phi_0)| \sin \phi_s. \quad (1.7)$$

If we define

$$I_{cs}(\Phi_{ext}) = 2I_c |\cos(\pi\Phi_{ext}/\Phi_0)|; \quad \phi_s = \phi, \quad (1.8)$$

Eq. (1.7) becomes

$$I = I_{cs}(\Phi_{ext}) \sin \phi. \quad (1.9)$$

This is the same as the dc Josephson equation in Eq. (1.3), but with a flux dependent critical current. Therefore, we can view the SQUID as a single effective Josephson junction with a tunable critical current. If we take the time derivative of Eq. (1.9), assuming a constant flux, we get

$$\frac{dI}{dt} = 2I_c |\cos(\pi\Phi_{ext}/\Phi_0)| \cos \phi \frac{d\phi}{dt}. \quad (1.10)$$

For small excitation, where  $I \ll I_{cs}$ , we have  $\cos \phi \sim 1$ . Together with the ac Josephson Eq. (1.3), Eq. (1.10) becomes

$$V = \frac{\hbar}{4eI_c |\cos(\pi\Phi_{ext}/\Phi_0)|} \frac{dI}{dt}. \quad (1.11)$$

Therefore, for small excitation, we can treat a SQUID as a tunable inductor with inductance,

$$L_J(\Phi_{ext}) = \frac{\hbar}{4eI_c |\cos(\pi\Phi_{ext}/\Phi_0)|}. \quad (1.12)$$

In reality, we should also consider the capacitance across the junction. Therefore, our SQUID model should consist of a tunable inductance,  $L_J$ , in parallel with the junction capacitance,  $C_J$ . To calculate the coupling energy stored in the Josephson junction,  $U(\phi)$ , we can integrate the electrical work done by a current source changing the phase. By using Eq. (1.3), we have

$$U(\phi) = \int_0^t IV dt' = \int_0^t (I_c \sin \phi) \left( \frac{\hbar}{2e} \frac{d\phi}{dt'} \right) dt' = E_J (1 - \cos \phi), \quad (1.13)$$

where  $E_J \equiv \hbar I_c / 2e$ . The critical current  $I_c$  or the Josephson energy  $E_J$  indicates how strongly the phases of the two superconducting electrodes are coupled through the weak link. We know that  $E_J$  is proportional to  $I_c$  and together with Eq. (1.6), we have

$$E_J(\Phi_{ext}) = E_{J,max} |\cos(\pi\Phi_{ext}/\Phi_0)| \sqrt{1 + \Lambda^2 \tan^2(\pi\Phi_{ext}/\Phi_0)}, \quad (1.14)$$

where

$$E_{J,max} = E_{J1} + E_{J2}; \quad \Lambda = \frac{E_{J1} - E_{J2}}{E_{J1} + E_{J2}}. \quad (1.15)$$

The parameter  $\Lambda$  above describes the asymmetry of the SQUID.

### 1.3 Quantum Optics with Superconducting Circuits

During the last decades, there is an emerging field growing rapidly, namely quantum optics with superconducting circuits [19, 20, 21, 22]. The comparison between quantum circuits and conventional quantum optics can be seen in Fig. 1.2 and Fig. 1.4. Comparing to the optical-real atom case, this approach of matter light coupling has the following advantages:

1. Photon-atom interaction  $U_{at-ph}$  can be engineered,
2. The photons are guided by waveguides; beam alignment is not needed,
3. Large vacuum field  $E_{0,rms} \sim 0.2$  V/m due to small mode volume,
4. Standard on-chip fabrication techniques,
5. Tunable transition energy of the atom,
6. Mechanically stable,
7. Huge electric dipole moment  $d = 10^2 - 10^4 ea_0$ , where  $d = U_{at-ph}/E_0$ .

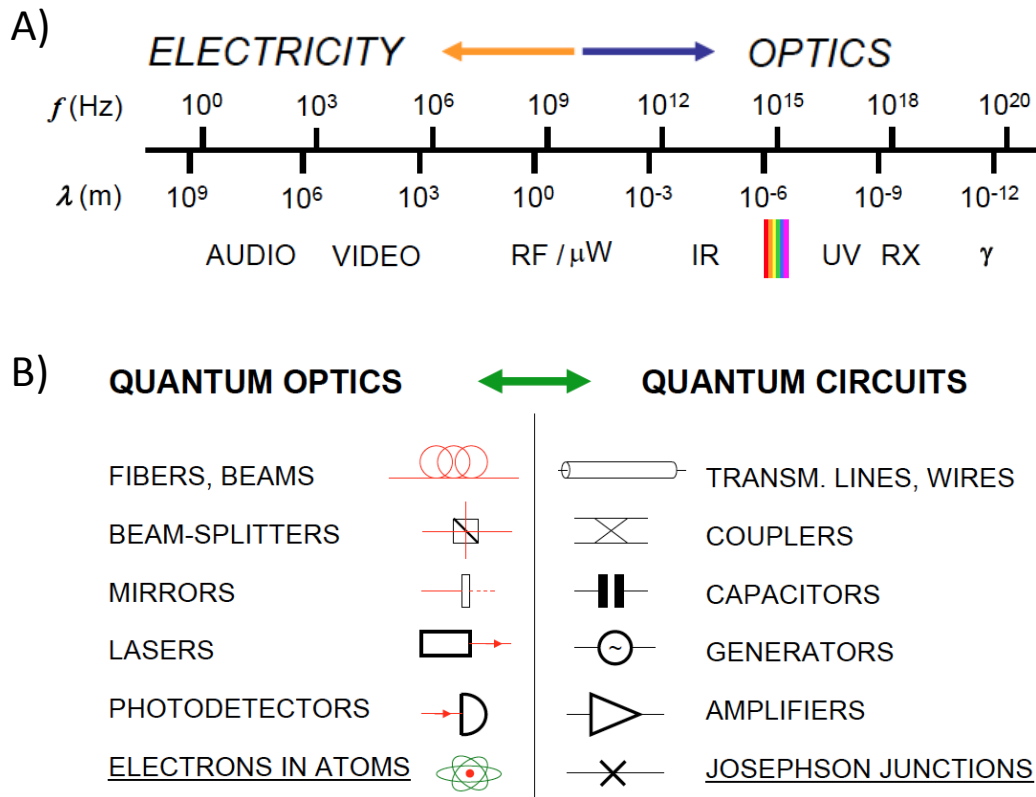


Figure 1.2: A) Frequency spectrum and corresponding wavelength from electrical to optics waves. Compared with optical photons, the frequency of microwave photons is  $10^5$  smaller. B) Comparison of the basic elements of quantum optics and quantum circuit toolboxes. Figure borrowed from [18].

The main disadvantage of superconducting qubit is the relatively short coherence times, of the order of  $\mu s$ . However recently there has been substantial progress and values close to  $100 \mu s$  has been reported [23]. Other disadvantage is that they have to be cooled to mK temperatures.

Fig. 1.2B compares the quantum optics and quantum circuits toolboxes. The waveguide in the optical domain is a fiber, whereas, in the microwave domain, we use a transmission line. In the microwave domain, we use a hybrid coupler as a beam splitter. A  $50 \Omega$  terminated port acts as a vacuum port. The microwave version of a beam splitter, the coupler, will be discussed in Chapter 2.5. In quantum circuits, capacitors can act as mirrors. The source of coherent optical light is a laser, whereas, in the microwave domain, it is a microwave generator. To perform measurements, in the optical domain, photon detectors are used, whereas in the microwave domain, we do not have the equivalent counterpart. However, we can amplify weak microwave fields with a cryogenic low-noise amplifier. After

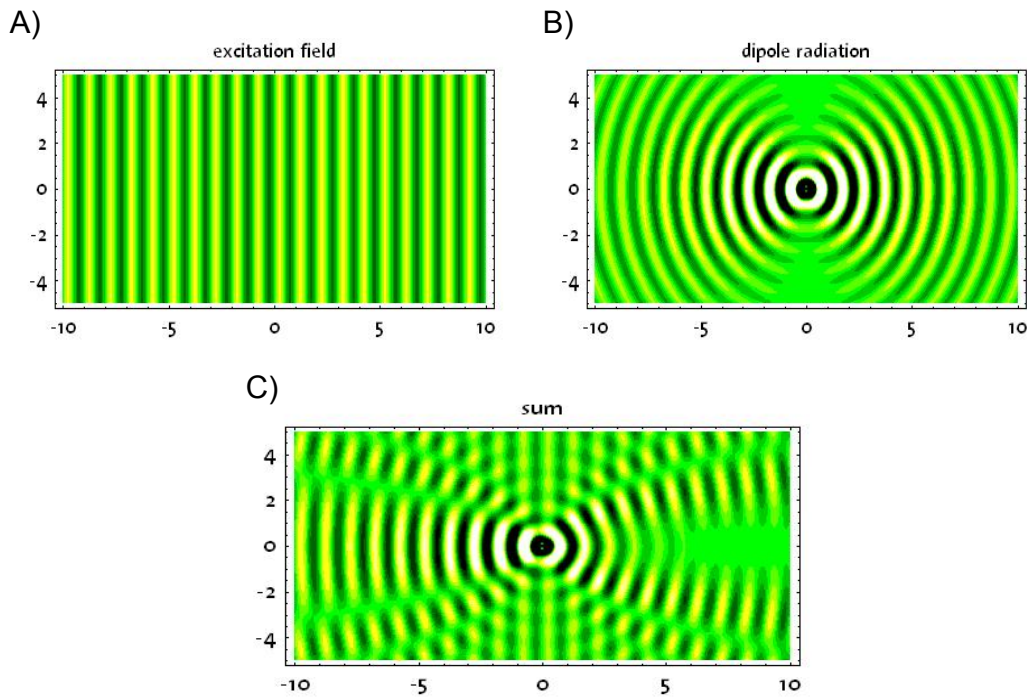


Figure 1.3: Interaction between a single atom/ dipole and a resonant propagating field in open space. A) The excitation field propagates in open space. B) The excited dipole/atom radiates field in all directions. C) The sum of the two fields result in destructive interference in the forward direction. Figure borrowed from [24]. Extinction of the forward wave only occurs in a small solid angle, this is due to the spatial mode mismatch between the excitation and radiated waves.

the heterodyne detection, we measure the quadratures of the field (in-phase and quadrature signals). In order to address individual atomic transitions, the energy spectrum must be anharmonic (nonlinear). In real atoms, this nonlinearity arises naturally from the coulomb potential. In a superconducting artificial atom, this nonlinearity is provided by the Josephson junction, which will be discussed in Chapter 2.1.

With the outstanding advantages of superconducting circuits as compared to conventional quantum optics, superconducting circuits have become a promising platform to investigate strong coupling between light and matter as well as enabling quantum information processing technology [25, 26, 27]. The development of the superconducting circuits is briefly shown below.

Starting from the 1980's, physicists were interested in whether macroscopic, man-made electrical circuits could behave quantum-mechanically. In 1985, J. M. Martinis, M. H. Devoret and J. Clarke demonstrated the discrete energy levels

of Josephson circuits, an early form of a superconducting artificial atom [28]. In the same year, they also demonstrated the macroscopic quantum tunneling of Josephson circuits [29]. In 1999, Nakamura *et al.* demonstrated quantum coherent oscillations of the state of a superconducting qubit [19]. In 2002, Vion *et al.* optimized the coherence time of a superconducting qubit [30], increased the coherence time by 2 order of magnitude. In 2004, Wallraff *et al.* demonstrated strong coupling between a superconducting qubit and a single photon in a transmission line cavity [20]. The field has grown quickly since then. Some of the exciting results include the following: resolving photon-number states [31], single artificial-atom lasing [32], synthesizing arbitrary photonics quantum states [21], three-qubit quantum error correction [33], implementation of a Toffoli gate [34], quantum feedback [35] and architectures for a superconducting quantum computer [36]. The nonlinear properties of Josephson junctions have also been used to study the dynamical Casimir effect [37], build quantum limited amplifiers [38, 39] and tunable cavities [40, 41, 42, 43].

More recently, theoretical and experimental work have begun to investigate the strong interaction between light and a single atom even without a cavity [44, 45, 46, 47]. This system consider a single atom interacting with a resonant propagating field in open space. The destructive interference between the excited dipole radiation and the incident field gives rise to extinction of the forward propagating wave for a weak incident field, see Fig. 1.3. This effect was first demonstrated for a single atom/molecule in three-dimensional (3D) open space, however the extinction of the forward incident wave did not exceed 12% [44, 46]. This is due to the spatial mode mismatch between the incident and scattered waves.

By taking advantage of the confinement of the propagating fields in a 1D open transmission line and the huge dipole moment of an artificial atom, strong coupling between an artificial atom and propagating fields can be achieved, as proposed in [48, 49] (see Fig. 1.4). In 2010, the first experiment was pioneered by O. Astafiev *et al.* [22], with extinctions in excess of 94%. Since then, there has been significant experimental progress [50, 51, 52, 53, 54, 55, 56, 57]. This system represents a potential key component in the field of quantum optics with propagating microwaves in superconducting circuits, which is the central scope of this thesis.

## 1.4 Quantum Network

In recent years, quantum information science has advanced rapidly, both at the level of fundamental research and technological development. For instance, quantum cryptography systems have become commercially available [58]. These systems are examples of quantum channels, serving mainly to distribute quantum information. There is a significant effort to combine these quantum channels with

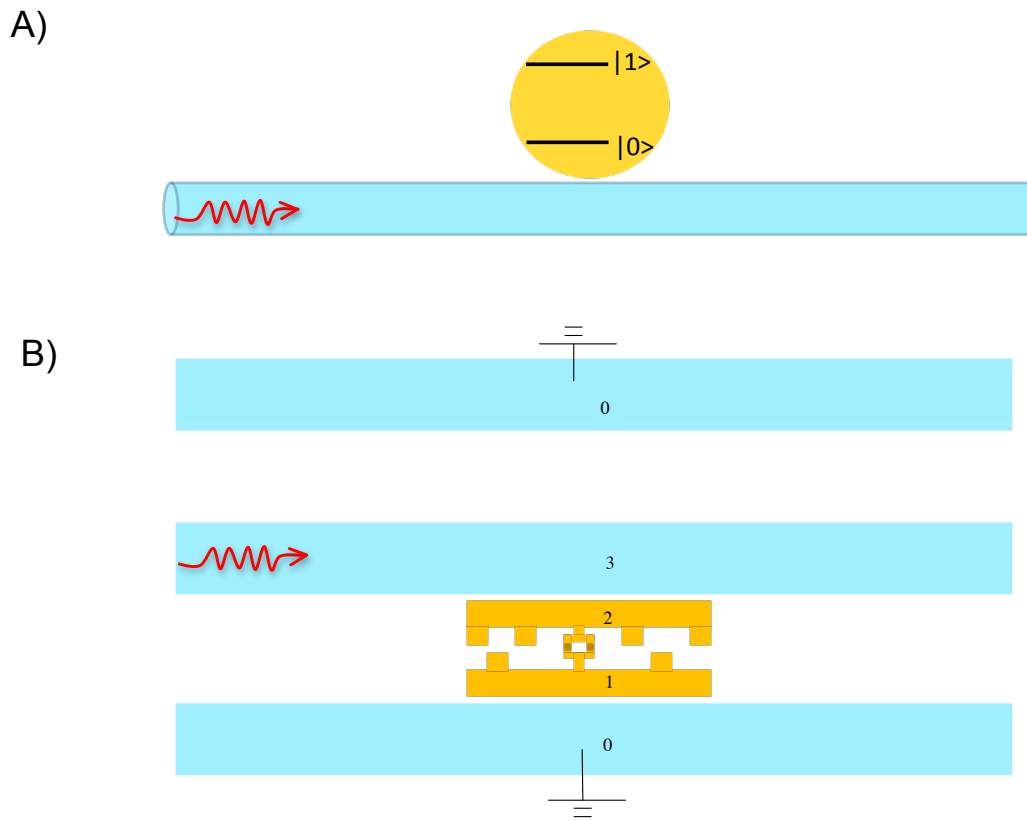


Figure 1.4: A single-atom scattering in 1D open space. The atom is coupled to a continuum of modes, as compared to the conventional cavity case, where the atom is coupled to a single mode. This novel system enables quantum applications with wide bandwidth. A) An optical photon (red) travels along a 1D waveguide (a blue fiber) interacting with a two-level atom (yellow). B) A microwave photon (red) travels along a 1D open coplanar waveguide (blue) interacting with a two-level artificial atom, a superconducting transmon qubit (yellow). The dark yellow regions represent the Josephson junction electrodes. The numbers 0,1,2,3 are the labels of the electrodes, which will be used to model the circuit in Chapter 2.3.2.

quantum nodes that would offer basic processing and routing capability. The combination of these channels and nodes would create a quantum network enabling applications simply impossible today [59]. Quantum network connecting simple quantum processing nodes is also a promising architecture for a scalable quantum computer.

Superconducting circuits is a promising technology for quantum information processing, whereas optical photons have advantages for long distance quantum communication via a quantum channel. As shown in Fig. 1.5, a hybrid quantum

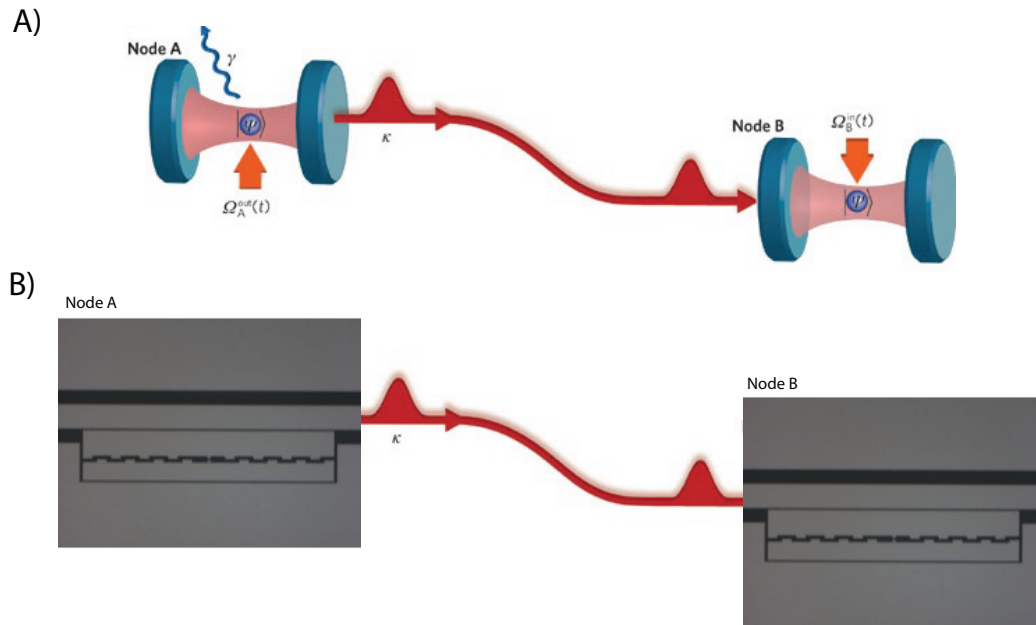


Figure 1.5: A) A quantum network consists of quantum nodes for processing and quantum channels for distributing quantum information. Figure borrowed from [59]. B) Hybrid quantum network. Telecom photons (red) distribute quantum information. Superconducting circuits process quantum information at nodes. A coherent conversion from microwave to optical photons would be needed.

network would combine the advantages of these two systems.

In this thesis, we demonstrate a novel way towards building up a quantum network based on superconducting circuits and artificial atoms. In particular, we demonstrate an example of a quantum node: the single-photon router, which can route quantum information up to 91% efficiency on nanosecond timescales, with the possibility of multiple outputs. We also demonstrate a photon-number filter, which can generate flying microwave photons, the carrier of quantum information. In addition, we demonstrate a cross-Kerr medium, which enables photon-photon interaction at the single-photon level, a resource for various quantum applications.

# Chapter 2

## Theoretical Background

This theory chapter is provided to help the reader understand the main experimental results in Chapter 4. Firstly, Chapter 2.1 includes the elements of an artificial atom, the Single Cooper Pair Box (SCB) [19, 27, 60, 61, 62, 63, 64, 65] and a modified version of the SCB, the transmon [66]. Secondly, Chapter 2.2 includes a description of the confinement structure of the propagating microwaves, the coplanar waveguide transmission line. Thirdly, Chapter 2.3 describes the interaction between an artificial atom and the propagating EM fields. Fourthly, Chapter 2.4 investigates the interaction of two propagating EM fields via a three-level artificial atom. Finally, Chapter 2.5 discusses the second-order correlation of microwave states that are generated by the artificial atom.

### 2.1 Superconducting Artificial Atom

In this thesis, the artificial atoms are made by superconducting circuits. In recent years, fundamental experiments [20, 21, 22, 40, 50, 51, 67, 68, 69, 70, 71, 72] based on superconducting circuits have led to a research field called circuit quantum electrodynamics (Circuit QED). The key elements of superconducting circuits are shown in Fig. 2.1A. They include linear capacitance,  $C$ , linear inductance,  $L$ , and the nonlinear Josephson inductance,  $L_J$ , defined in Eq. (1.12). To illustrate how one can build an artificial atom based on circuit elements, consider the linear LC circuit in Fig. 2.1B. The classical Hamiltonian of this circuit is the sum of the charging energy  $E_C$  and the inductive energy  $E_L$

$$H = \frac{Q^2}{2C} + \frac{\Phi^2}{2L}, \quad (2.1)$$

where  $Q$  is the charge stored on the capacitor  $C$  and  $\Phi$  is the flux stored in the inductor  $L$ . By defining the resonant frequency  $\omega_0 = 1/\sqrt{LC}$ , we can rewrite

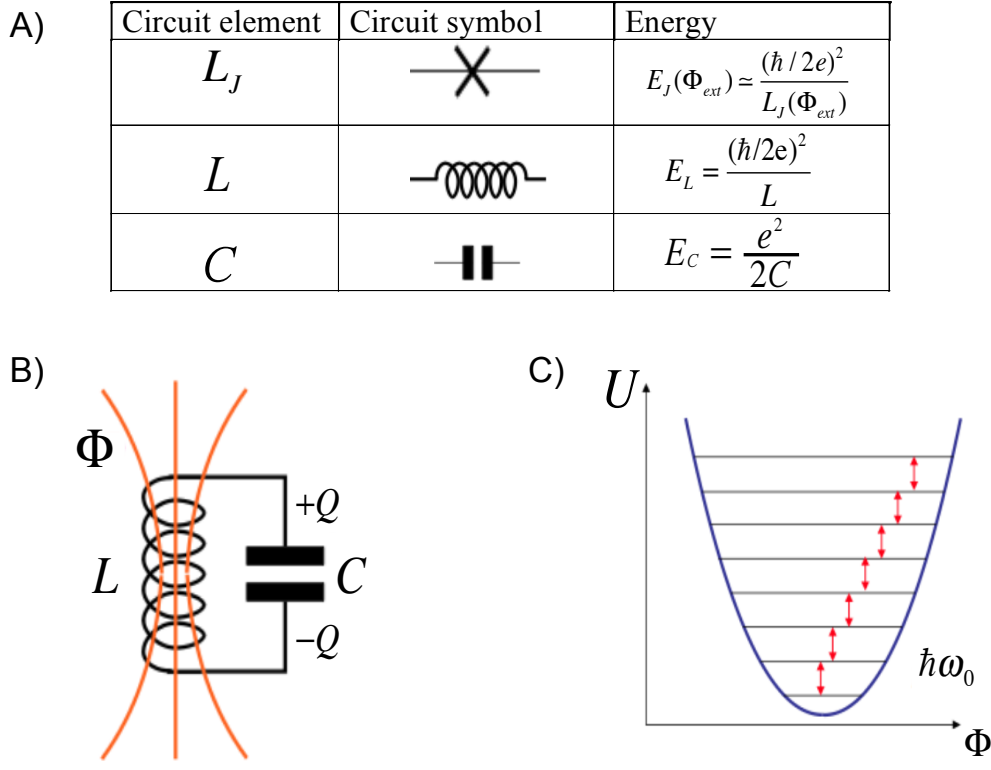


Figure 2.1: A) The table shows the circuit elements used to build superconducting artificial atoms, the corresponding circuit symbols and energies. B) An LC resonator with charge  $Q$  on the capacitor  $C$  and flux  $\Phi$  in the inductor  $L$ . C) Energy  $U$  versus flux of a quantum harmonic oscillator (LC resonator). The transition energy is  $\hbar\omega_0$ .

Eq. (2.1) as

$$H = \frac{Q^2}{2C} + \frac{1}{2}C\omega_0^2\Phi^2. \quad (2.2)$$

This Hamiltonian can be compared with that of a moving particle with mass  $m$ , momentum  $p_m$  and position  $x$  in a harmonic potential,

$$H = \frac{p_m^2}{2m} + \frac{1}{2}m\omega_m^2x^2. \quad (2.3)$$

By analogy, we can map the LC oscillator onto the mechanical oscillator according to Table 2.1,

Since we want to consider the quantum mechanical properties of this system, we can promote the classical variables  $p_m$ ,  $x$  in Eq. (2.3) and  $Q$ ,  $\Phi$  in Eq. (2.2) to quantum operators  $\hat{p}_m$ ,  $\hat{x}$  and  $\hat{Q}$ ,  $\hat{\Phi}$ . How this is done more formally is described

Electrical	Mechanical
$Q$	$p_m$
$C$	$m$
$\omega_0$	$\omega_m$
$\Phi$	$x$
$E_C$	Kinetic energy
$E_L$	Potential energy

Table 2.1: Analogy between an electrical oscillator and a mechanical oscillator

in [18]. Therefore, the quantum Hamiltonian of an LC resonator Eq. (2.2) can be written in the following form,

$$H = \hbar\omega_0 \left( a^\dagger a + \frac{1}{2} \right), \quad (2.4)$$

where  $a^\dagger$  and  $a$  are the creation and annihilation operators for excitations in the oscillator, defined as

$$a^\dagger = \sqrt{\frac{C\omega_0}{2\hbar}} \left( \hat{\Phi} - i \frac{\hat{Q}}{C\omega_0} \right); \quad a = \sqrt{\frac{C\omega_0}{2\hbar}} \left( \hat{\Phi} + i \frac{\hat{Q}}{C\omega_0} \right), \quad (2.5)$$

with the relationship  $[a, a^\dagger] = 1$ . Conversely, charge and flux can be expressed in terms of creation and annihilation operator as follows,

$$\hat{Q} = i\sqrt{\frac{\hbar}{2Z}} (a^\dagger - a); \quad \hat{\Phi} = \sqrt{\frac{\hbar Z}{2}} (a^\dagger + a). \quad (2.6)$$

We used the relation,  $C\omega_0 = \sqrt{C/L} \equiv 1/Z$ , where  $Z$  is the characteristic impedance of the circuit. The energy spectrum of a quantum harmonic oscillator is shown in Fig. 2.1C. The quantum levels are equally spaced. This means that we cannot address individual transitions. Therefore, nonlinearity is needed to build an artificial atom, in which the level spacing is anharmonic. In superconducting circuits, a Josephson junction provides a nonlinear inductor with very little dissipation. As shown in table 2.1, the inductive energy of the Josephson junction acts as a potential energy, according to Eq. (1.13):

$$U = -E_J \cos(\phi). \quad (2.7)$$

where we neglect the offset energy, which is independent of  $\phi$ . By replacing the linear inductor with a Josephson junction in the LC circuit in Fig. 2.1B, the

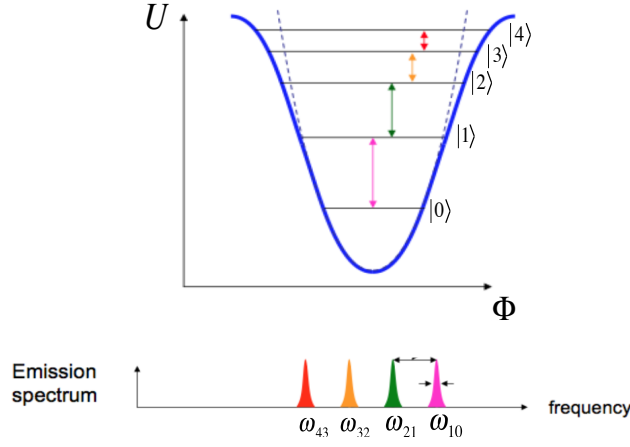


Figure 2.2: Top: the energy spectrum of an artificial atom made by a Josephson junction and its energy levels. The cosine potential comes from the inductive energy of the Josephson junction, and it gives rise to an anharmonic (nonlinear) spectrum. Bottom: the corresponding emission spectrum for these four transitions [18]. The arrows around the pink spectrum indicate the width of 0-1 transition, whereas the arrows between the pink and green spectrum indicate the anharmonicity between the 0-1 and 1-2 transition.

quadratic potential becomes a cosine potential. This procedure results in an anharmonic energy level spacing, as shown in Fig. 2.2. In this case, we can address different individual transitions and call it an artificial atom. The absolute nonlinearity is defined as the ratio of the peak distance to the peak width, see Fig. 2.2. Besides the nonlinear conditions mentioned above, in order to observe the quantum behavior of the atom, we have the following restriction,  $k_B\Theta \ll \hbar\omega_{10} \ll \Delta_s$  where  $k_B\Theta$  is the thermal energy,  $\Theta$  is the temperature of the system.  $\hbar\omega_{10}$  is the energy transition of the two level atom and  $\Delta_s$  is the superconducting gap energy.

Several different kinds of superconducting atoms have been implemented [73]. They can be distinguished by their different  $E_J/E_C$  and  $E_L/E_J$  ratios (see Fig. 2.3). In this thesis, we focus on the single Cooper-Pair Box (SCB) and the transmon.

### 2.1.1 The Single Cooper-Pair Box (SCB)

A SCB is composed of a small island, coupled to a reservoir electrode via a Josephson junction. A gate electrode is used to pump Cooper pairs into or out of the island via the junction. The Josephson junction is often made in a SQUID configuration (Fig. 2.4A) to produce an  $E_J$  which is tunable via  $\Phi_{ext}$ , according to Eq. (1.14). The Hamiltonian of the SCB is given by [19, 60, 61, 62, 63]

$$H(\hat{n}, \hat{\phi}) = E_Q(\hat{n} - n_g)^2 - E_J(\Phi) \cos \hat{\phi} \quad (2.8)$$

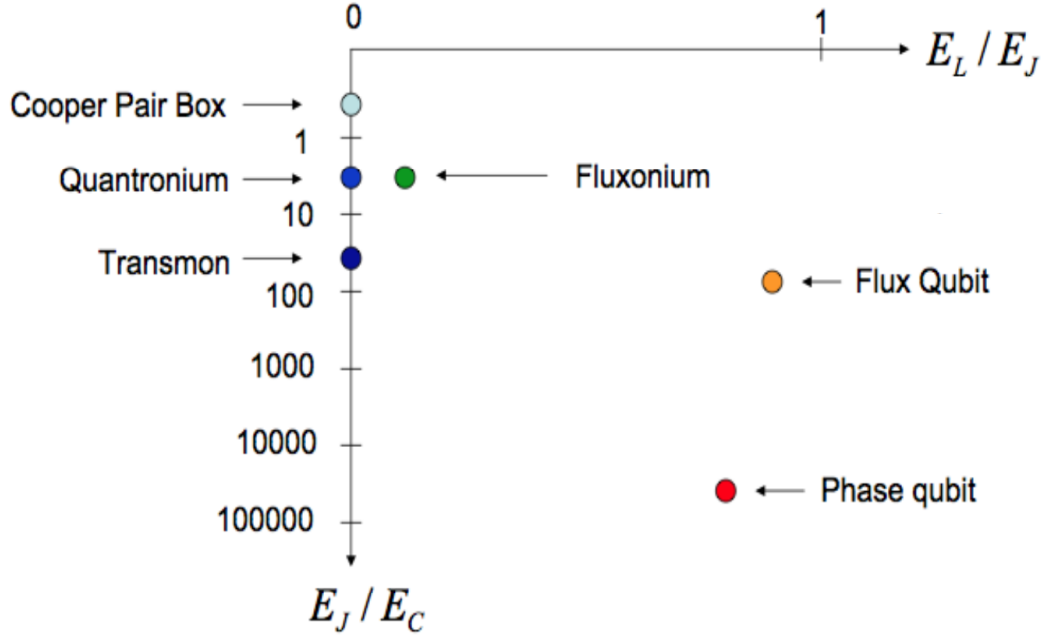


Figure 2.3: The family of superconducting artificial atoms. The type of atom depends on  $E_J/E_C$  and  $E_L/E_J$ . Figure borrowed from [18].

where

$$E_Q = 4E_C = \frac{(2e)^2}{2C_\Sigma}; \quad C_\Sigma = C_g + C_J; \quad n_g = C_g V_g / (2e); \quad (2.9)$$

$$\hat{n} = \frac{\hat{Q}}{2e}; \quad \hat{\phi} = 2\pi \frac{\hat{\Phi}_J}{\Phi_0}$$

$E_Q$  and  $E_C$  are the charging energies for Cooper pairs and electrons, respectively.  $n_g$  and  $V_g$  are the normalized gate charge in the units of Cooper pairs and the gate voltage, respectively. The total capacitance  $C_\Sigma$  is the sum of the gate capacitor  $C_g$  and the junction capacitor  $C_J$  (see Fig. 2.4A).  $\hat{n}$  and  $\hat{\phi}$  are the number and phase operator, respectively. The Cooper pairs with charge  $\hat{Q}$  that have tunneled into the box via the junction and the flux  $\hat{\Phi}_J$  between the two sides of the junction are quantum mechanicals conjugate operators, which obey the canonical commutation relation  $[\hat{\Phi}_J, \hat{Q}] = i\hbar$ .

The exponential of the phase operator acts as ladder operators in the charge basis  $|n\rangle$

$$e^{\pm i\hat{\phi}} |n\rangle = |n \pm 1\rangle. \quad (2.10)$$

We can then express the Hamiltonian Eq. (2.8) in the charge basis,

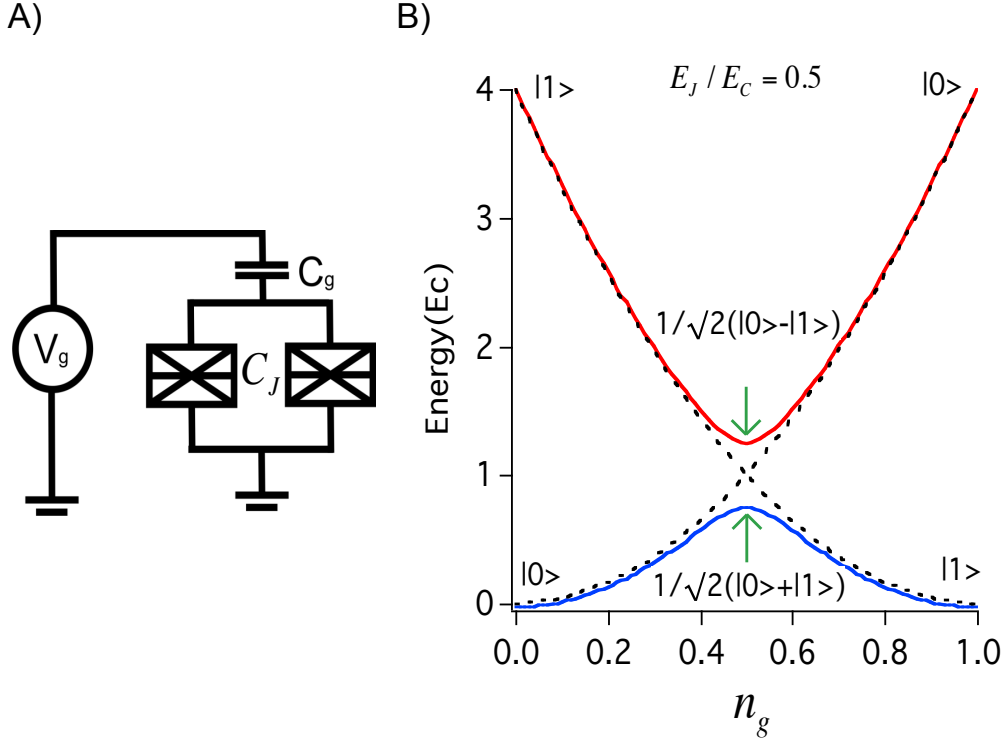


Figure 2.4: A) The SCB in SQUID configuration.  $E_J$  can be tuned by external magnetic flux through the SQUID loop. B) The two lowest energy states of the SCB as a function of the gate charge  $n_g$  for  $E_J/E_C = 0.5$ . Excited state and ground state are the solid red and the solid blue lines, respectively. The dashed black lines represent the case of zero Josephson energy. The green arrows indicate the optimal bias point, where the first derivative is zero with respect to gate charge.

$$H = \sum_{n=-\infty}^{\infty} \left\{ E_Q (n - n_g)^2 |n\rangle \langle n| - \frac{E_J(\Phi)}{2} (|n+1\rangle \langle n| + |n-1\rangle \langle n|) \right\}. \quad (2.11)$$

The role of the Josephson energy is to mix the charge states through tunneling. If  $E_Q \gg E_J$  and we limit  $0 < n_g < 1$ , we can limit the description to only two number states,  $|0\rangle$ , and  $|1\rangle$ . Subtracting a common energy offset  $E_Q[n_g^2 + (1 - 2n_g)/2]\mathbb{I}$ , where  $\mathbb{I}$  is the identity matrix, the Hamiltonian Eq. (2.11) then becomes,

$$H = -\frac{1}{2} E_{ch}(n_g) \sigma_z - \frac{1}{2} E_J(\Phi) \sigma_x, \quad (2.12)$$

with the electrostatic energy  $E_{ch} = E_Q(1 - 2n_g)$ .  $\sigma_z$  and  $\sigma_x$  are the Pauli spin

matrices, where  $\sigma_z = |0\rangle\langle 0| - |1\rangle\langle 1|$ ,  $\sigma_x = |0\rangle\langle 1| + |1\rangle\langle 0|$ . This Hamiltonian is of the same form as that of a spin 1/2 particle in a magnetic field, where  $\mu_{10}\vec{B} = (E_J, 0, E_{ch})$  in Eq. (1.2). The eigenenergies can be written as

$$E_{\pm} = \pm \frac{1}{2} \sqrt{E_{ch}^2(n_g) + E_J^2(\Phi)}, \quad (2.13)$$

with the corresponding eigenstates

$$|-\rangle = \cos(\theta/2) |0\rangle + \sin(\theta/2) |1\rangle; \quad (2.14)$$

$$|+\rangle = -\sin(\theta/2) |0\rangle + \cos(\theta/2) |1\rangle; \quad (2.15)$$

$$\theta = \tan^{-1}(E_J/E_{ch}), \quad (2.16)$$

where  $\theta$  is the mixing angle with respect to the z-axis.

Time-resolved measurements demonstrating quantum coherence in the SCB were first observed by Nakamura *et al.* [19] in 1999.

### Decoherence in the SCB

So far, we have neglected the effects of the environment on the SCB. Any noise in the environment will give rise to decoherence in the SCB and result in random evolution of the qubit state. In other words, the coherent superposition of the qubit states will be lost due to the interaction with the environment. The pure qubit state will evolve into a statistical mixture of the two qubit states. The source of decoherence affects the SCB through either the electrostatic energy  $E_{ch}$  or the Josephson energy  $E_J$ . Fluctuations of  $E_{ch}$  can be caused by voltage noise in  $n_g$ , background two level fluctuators [74] or dielectric loss [75]. The fluctuation of  $E_J$  can be caused by flux noise entering the SQUID loop or critical current noise. The effects of noise on the qubit can be characterized by two time constants, the relaxation time  $T_1$  and the decoherence time  $T_2$ . To describe how the qubit states evolve in time under the influence of noise, we introduce the density matrix  $\rho = |\psi\rangle\langle\psi|$ , where  $|\psi\rangle$  is defined in (1.1). Any arbitrary density matrix for a two level system can be written as

$$\rho = \frac{1}{2}(\mathbb{I} + u_x\sigma_x + u_y\sigma_y + u_z\sigma_z). \quad (2.17)$$

Here,  $\mathbb{I}$  is the identity matrix and  $\vec{u} = (u_x, u_y, u_z)$  is a vector of the length  $|u| \leq 1$ , which describes the qubit state on (pure state) or inside (mixed state) the Bloch sphere (Fig. 1.1A). The expectation value of the Pauli operators are  $\langle\sigma_i\rangle = u_i$ , where  $i \in x, y, z$ . For a spin 1/2 particle in a magnetic field, according to Eq. (1.2), the Hamiltonian can be written as

$$H = -\frac{\hbar}{2}(\omega_x\sigma_x + \omega_y\sigma_y + \omega_z\sigma_z), \quad (2.18)$$

where the strong static field is assumed along the z axis. The state then follows the Bloch equation [76, 8],

$$\dot{\vec{u}} = -\vec{\omega} \times \vec{u} - \frac{1}{T_2}(u_x \hat{x} + u_y \hat{y}) - \frac{1}{T_1}(u_z - u_z^0) \hat{z}, \quad (2.19)$$

where  $\vec{\omega} = (\omega_x, \omega_y, \omega_z)$ . The first term on the right describes the unitary evolution of the state without decoherence. The second term captures the effect of decoherence, the third term describes the relaxation of the state to  $u_z^0$ , the steady state projection on the z axis. The excitation (absorption) rate  $\Gamma_+$ , relaxation (emission) rate  $\Gamma_-$  and the pure dephasing rate  $\Gamma_\phi$  can be calculated from Fermi's Golden rule [8, 77],

$$\Gamma_\pm = \frac{\pi S_\perp(\mp\omega_z)}{2\hbar^2}; \quad \Gamma_\phi = \frac{\pi S_z(\omega \simeq 0)}{2\hbar^2}. \quad (2.20)$$

where  $S_\perp(\omega_z)$  is the spectral density of the fluctuations in  $\omega$  perpendicular to the z axis, for  $\omega_z \gg \omega_x, \omega_y$ .  $S_z(\omega \simeq 0)$  is the spectral density of fluctuations along the z axis. For a system where the environment is in thermal equilibrium at a temperature  $\Theta$ , the balance between absorption and emission is set by:

$$\Gamma_+/\Gamma_- = e^{-\hbar\omega_z/k_B\Theta}; \quad u_z^0 = \frac{\Gamma_- - \Gamma_+}{\Gamma_- + \Gamma_+} = \tanh\left[\frac{\hbar\omega_z}{2k_B\Theta}\right]. \quad (2.21)$$

The relaxation time  $T_1$  and the decoherence time  $T_2$  are given by

$$\frac{1}{T_1} = \Gamma_1 = \Gamma_- + \Gamma_+; \quad \frac{1}{T_2} = \Gamma_2 = \Gamma_\phi + \frac{\Gamma_1}{2}, \quad (2.22)$$

The dephasing of the SCB mainly comes from fluctuations of  $E_{ch}$  (charge noise in  $\sigma_z$  direction). This leads to short coherence time [19, 61, 78]. Vion *et al.* [74] demonstrated that the coherence time of a modified SCB could be made several orders of magnitude longer by biasing at an optimal working point. This optimal point is a saddle point of the energy bands where the first derivatives with respect to both the charge and flux are zero. As a result, the qubit is insensitive to charge and flux noise to first order. As an example, in Fig. 2.4B, at  $n_g = 0.5$ , we see the optimal point with respect to gate charge, indicated by the green arrows. Koch *et al.* [66] further developed this idea to create a new qubit design based on a modified SCB, named the transmon. This new design has a reduced sensitivity to charge noise at all gate bias points and will be described in the following section.

### 2.1.2 The Transmon

The transmon qubit is essentially a SCB, but with an additional shunt capacitor  $C_s$  (Fig. 2.5). The additional shunt capacitor decreases the charging energy. As

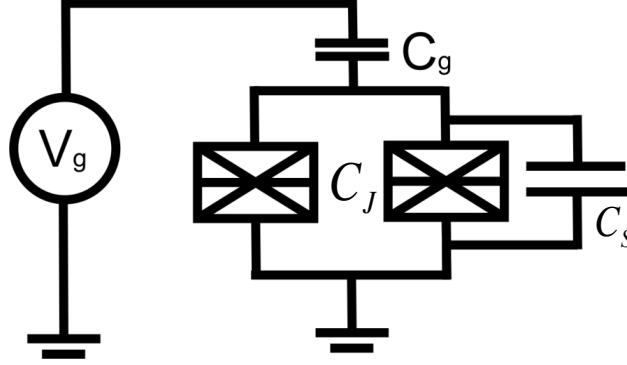


Figure 2.5: A transmon: a SCB with an additional shunt capacitor  $C_s$ . This additional shunt capacitor decreases  $E_C$ , which results in a high  $E_J/E_C$ .

$E_J/E_C$  increases, the energy bands become flatter with respect to the gate charge (Fig. 2.6), making the transition energy less sensitive to charge noise [68, 79]. Unfortunately, this also has the effect of decreasing the anharmonicity between levels. We define an anharmonicity parameter  $\alpha_r$  and a charge dispersion  $\varepsilon_m$  as,

$$\alpha_r = \frac{E_{21} - E_{10}}{E_{10}}; \quad (2.23)$$

$$\varepsilon_m = [E_m(n_g = 0.5) - E_m(0)] / E_{10}, \quad (2.24)$$

where  $E_m$  ( $m, n = 0, 1, 2, \dots$ ) are the energy levels and  $E_{mn} = E_m - E_n$ . If the anharmonicity is too low, the individual levels cannot be addressed and the transmon can no longer be considered an artificial atom. The anharmonicity needs to be at least larger than the spectrum width of the 0-1 transition. The charge dispersion decreases exponentially with  $E_J/E_C$  (Fig. 2.7B), while the anharmonicity approaches zero much slower (Fig. 2.7A). Therefore, it is possible to find parameters such that the transmon is insensitive to charge noise but still sufficiently anharmonic.

When the charging energy of the SCB is decreased, more charge states need to be included. Therefore, the charge basis is no longer a good eigenbasis for the circuit. We can express  $\hat{n}$  in the phase basis, using

$$\hat{n} = -i \frac{\partial}{\partial \phi}. \quad (2.25)$$

By substituting Eq. (2.25) into the SCB Hamiltonian Eq. (2.8), we have

$$H = 4E_C \left( -i \frac{\partial}{\partial \phi} - n_g \right)^2 - E_J \cos \hat{\phi}, \quad (2.26)$$

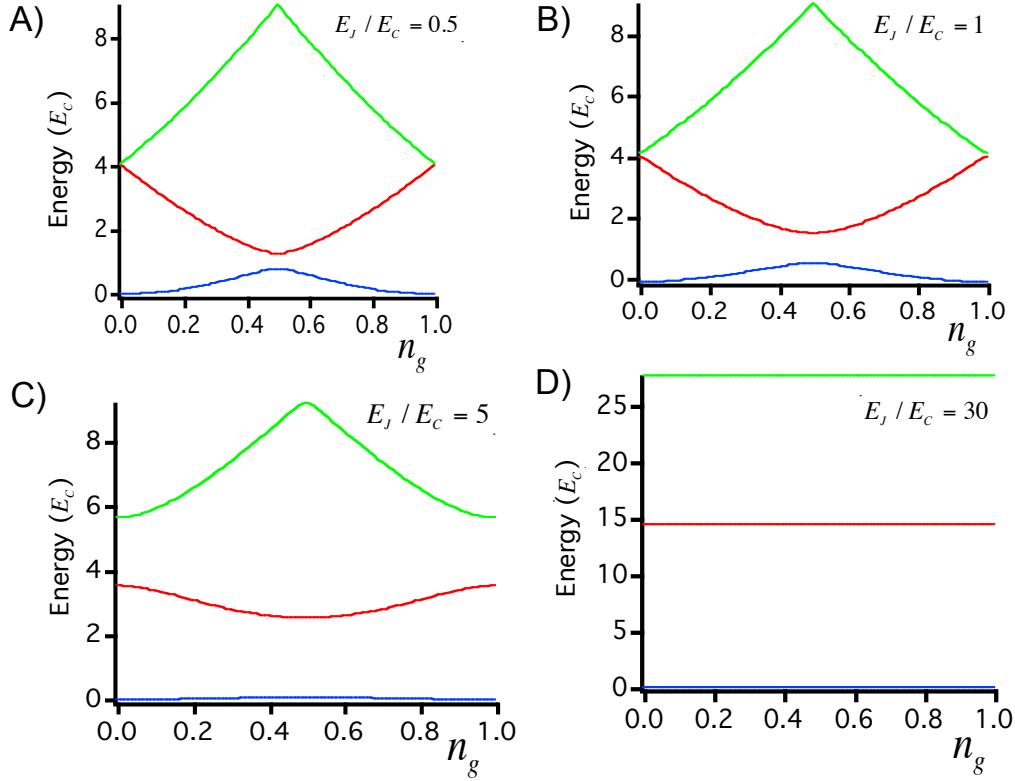


Figure 2.6: The lowest three energy levels (in the unit of  $E_C$ ) of a SCB versus gate charge  $n_g$  for different  $E_J/E_C$ . A)  $E_J/E_C = 0.5$ , B)  $E_J/E_C = 1$ , C)  $E_J/E_C = 5$ , D)  $E_J/E_C = 30$  (transmon limit). The ground state, first excited state and second excited state are the blue, red and green curves, respectively.

with the eigenenergies and eigenstates expressed in the phase basis:

$$H\Psi_m(\phi) = E_m\Psi_m(\phi). \quad (2.27)$$

As a differential equation, this is known as the Mathieu equation [80], which has known solutions, although not in terms of elementary function. Alternatively, one can solve for the eigenenergies of the SCB Hamiltonian by diagonalizing in the charge basis and including many charge states. The more charge states that are included, the better the accuracy. The results shown in Fig. 2.6 include 50 charge states.

As mentioned in Table 2.1, the Josephson energy and the charging energy can be viewed as potential and kinetic energy, respectively. The Hamiltonian of the SCB can be viewed as a particle in a periodic potential. As the mass of the particle increases ( $E_J/E_C$  increases), the kinetic energy decreases, and the particle gets localized near one of the minima of the potential. Then, we can approximate the

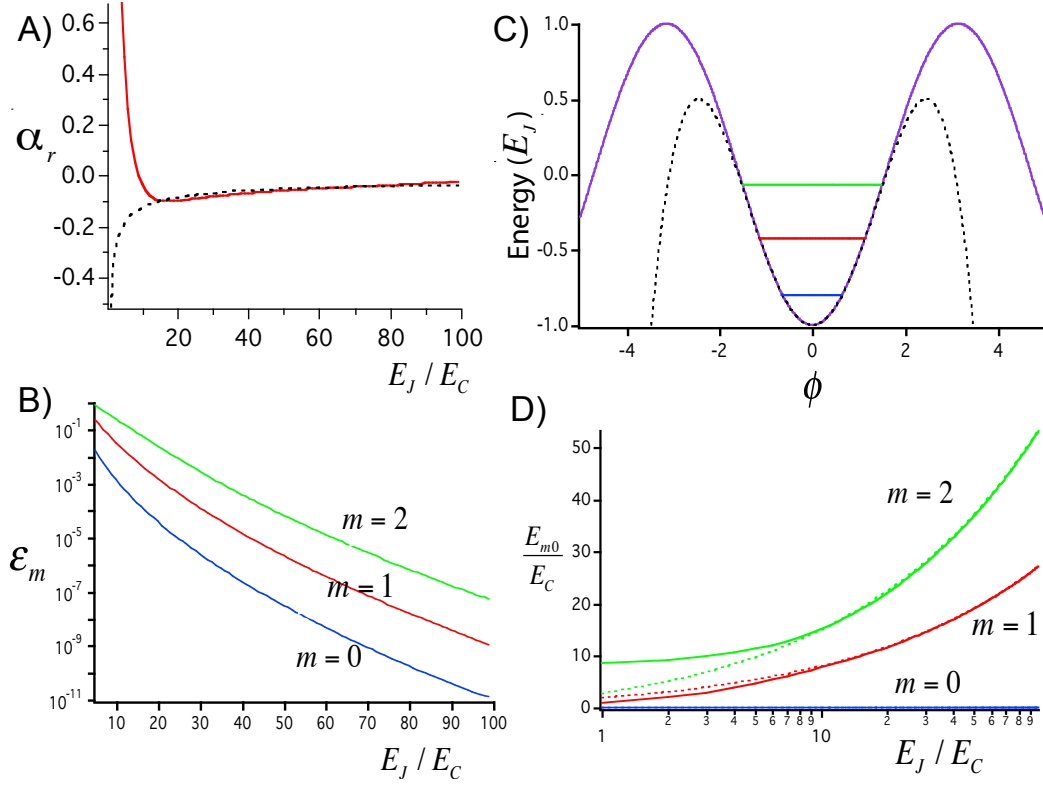


Figure 2.7: A) Anharmonicity of the SCB as a function of  $E_J/E_C$  ratio. Exact (approximation) solution is shown in solid (dashed). B) Charge dispersion of the SCB as a function of  $E_J/E_C$  ratio for different energy levels. C) Cosine potential (solid) plotted together with the quartic approximation (dashed) using Eq. (2.28). Inside the potential is the three lowest energy states in the case of  $E_J/E_C = 50$ . D) Energy level difference  $E_m - E_0$  at  $n_g = 0.5$  as a function of  $E_J/E_C$  ratio. Solid curves show the exact results. Dashed curves are based on Eq. (2.29).

cosine potential around zero with its Taylor expansion to the fourth order,

$$U(\phi) \simeq -E_J \left( 1 - \frac{1}{2}\phi^2 + \frac{1}{24}\phi^4 \right). \quad (2.28)$$

By treating it as a perturbation from the exact harmonic solution, we get the following eigenenergies [66] and anharmonicity parameter,

$$E_m \simeq -E_J + \sqrt{8E_J E_C} \left( m + \frac{1}{2} \right) - \frac{E_C}{12} (6m^2 + 6m + 3) \quad (2.29)$$

$$\alpha_r = -\frac{E_C}{\omega_{10}} = -\frac{1}{\sqrt{8E_J/E_C} - 1} \quad (2.30)$$

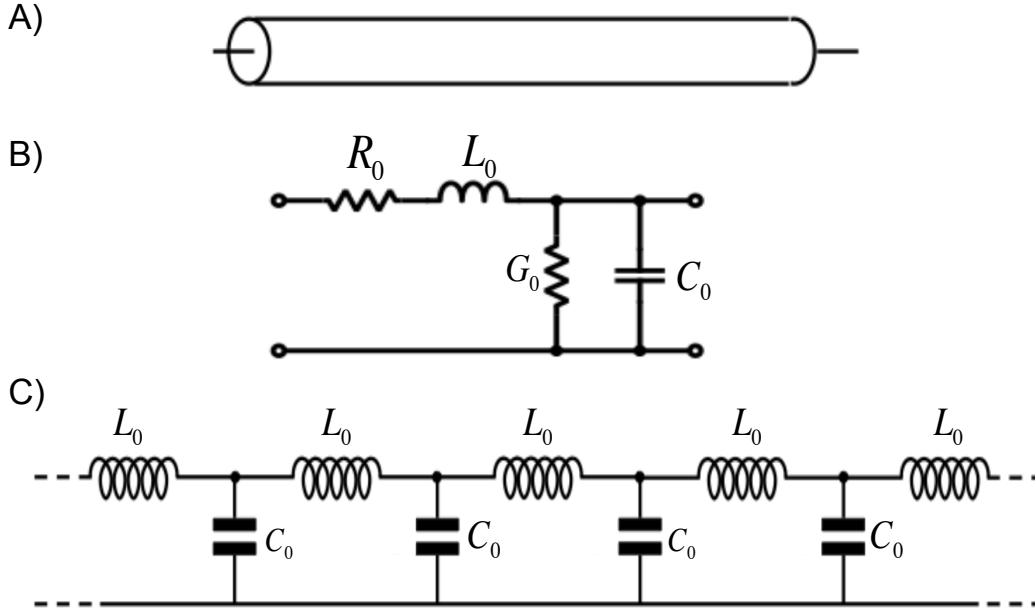


Figure 2.8: A) Transmission line B) Lumped-element model of a section of transmission line. C) Lossless ( $R_0 \simeq 0, G_0 \simeq 0$ ) transmission line (cascade of B).

For  $E_J/E_C \geq 20$ , the approximation is quite good (Fig. 2.7 C,D). We make use of the lowest three levels to form our artificial atoms in this thesis.

## 2.2 1D Coplanar Waveguide Transmission Line

A 1D Coplanar Waveguide (CPW) is used to confine the propagating microwaves (see blue part of Fig. 1.4B). A CPW can be described using a transmission line model. A CPW supports quasi Transverse Electromagnetic (quasi-TEM) modes. For a pure TEM mode, there are no electric or magnetic components along the direction of propagation. A quasi-TEM transmission line (Fig. 2.8A), can be modeled as a number of lumped circuit elements (Fig. 2.8B) where  $R_0, L_0, G_0, C_0$  are series resistance, series inductance, shunt conductance and shunt capacitance per unit length ( $\Delta x$ ). A finite length of lossless transmission line can be represented by a cascade of circuits with  $R_0 = 0, G_0 = 0$ , as shown in Fig. 2.8C.

For a harmonic signal, and taking the limit  $\Delta x \rightarrow 0$ , we can solve the wave equation from the transmission line model. The wave in the transmission line consists of a forward propagating wave with voltage (current) amplitude  $V^+(I^+)$  and a backward propagating wave with amplitude  $V^-(I^-)$ , with angular frequency  $\omega$

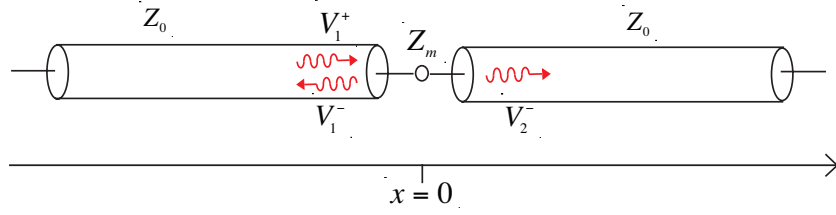


Figure 2.9: Incoming, reflected and transmitted wave propagate along a transmission line with impedance  $Z_0$ ,  $Z_m$  (representing a mismatch) and  $Z_0$ .

and complex propagating constant  $\xi$ , mathematically expressed as [81],

$$V(x) = V^+ e^{i\omega t - \xi x} + V^- e^{i\omega t + \xi x}; \quad (2.31)$$

$$I(x) = I^+ e^{i\omega t - \xi x} - I^- e^{i\omega t + \xi x}, \quad (2.32)$$

where  $\xi = i\Upsilon + \kappa = \sqrt{(R_0 + i\omega L_0)(G_0 + i\omega C_0)}$ .

The real part  $\kappa$  of the complex propagation constant describes the losses per unit length. The voltage  $V^+$ ,  $V^-$  and current amplitudes  $I^+$ ,  $I^-$  are related via the characteristic impedance

$$\frac{V^+}{I^+} = \frac{V^-}{I^-} = Z_0 = \sqrt{\frac{R_0 + i\omega L_0}{G_0 + i\omega C_0}}. \quad (2.33)$$

Considering a lossless transmission line (small series resistance  $R_0 \sim 0$  and small shunt conductance  $G_0 \sim 0$ ), we have

$$\xi \simeq i\omega\sqrt{L_0 C_0}; \quad Z_0 \simeq \sqrt{\frac{L_0}{C_0}}. \quad (2.34)$$

Fig. 2.8C shows the corresponding model.

For a lossless transmission line terminated by an arbitrary load impedance  $Z_L$ , the complex voltage reflection coefficient  $r$  is [81],

$$r = \frac{V^-}{V^+} = \frac{Z_L - Z_0}{Z_L + Z_0} = |r| e^{i\vartheta}, \quad (2.35)$$

where  $\vartheta$  is the phase and  $|r|$  is the magnitude. If  $Z_L = Z_0$ , this relation gives  $r = 0$ , meaning that the backward propagating signal is zero. When this condition is fulfilled, the transmission line is said to be matched to the load impedance,  $Z_L$ .

In Fig. 2.9, considering a transmission line, there is an impedance mismatch at  $x = 0$ . We have an incoming wave  $V_1^+$  and reflected wave  $V_1^-$  from the left. Assuming there are no incoming waves from the right  $V_2^+ = 0$  and the transmitted wave on the right is denoted as  $V_2^-$ , we have

$$V(x = 0^-) = V(x = 0^+); \quad V_1^+ + V_1^- = V_2^+ + V_2^-. \quad (2.36)$$

The voltage transmission (reflection) coefficient  $t$  ( $r$ ) is defined as the ratio between the transmitted (reflected) wave and the incoming wave,

$$t = \frac{V_2^-}{V_1^+}; \quad r = \frac{V_1^-}{V_1^+}. \quad (2.37)$$

Therefore, combining expressions (2.36) and (2.37), we have

$$t = r + 1. \quad (2.38)$$

## 2.3 Interaction of a Two-Level Atom and EM Fields

In this section, we investigate the interaction between the two lowest energy levels of a SCB and the EM field, based on a quantum circuit model. First, we will introduce the dipole coupling of the SCB. Then, we will proceed to the main system of this thesis: a SCB in a 1D open transmission line. Finally, we will discuss a similar system by introducing a boundary condition: a SCB at the end of a transmission line.

### 2.3.1 Dipole Coupling of a SCB

From Section 2.1, a transmon or a SCB can be considered as a two-level artificial atom. The electrostatic energy

$$H_{ch} = 4E_C(\hat{n} - n_g)^2, \quad (2.39)$$

depends on the normalized gate charge,  $n_g = C_g V_g / (2e)$ , induced by the gate voltage  $V_g$ . In the presence of a microwave field, the gate voltage consists of a DC and a microwave component,

$$V_g = V_{DC} + V_{\mu\omega}; \quad (2.40)$$

$$n_g = n_{DC} + n_{\mu\omega}.$$

By putting expression Eq. (2.40) into the Hamiltonian Eq. (2.39), we obtain

$$H_{ch} = 4E_C(\hat{n} - n_{DC})^2 - 8E_C(\hat{n} - n_{DC})n_{\mu\omega} + 4E_C n_{\mu\omega}^2. \quad (2.41)$$

The first term of Eq. (2.41) is the original electrostatic Hamiltonian with a DC bias. The only state dependent term, which is due to the microwaves, is

$$H_{dipole} = 8E_C n_{\mu\omega} \hat{n} = 2e \frac{C_g}{C_\Sigma} V_{\mu\omega} \hat{n}. \quad (2.42)$$

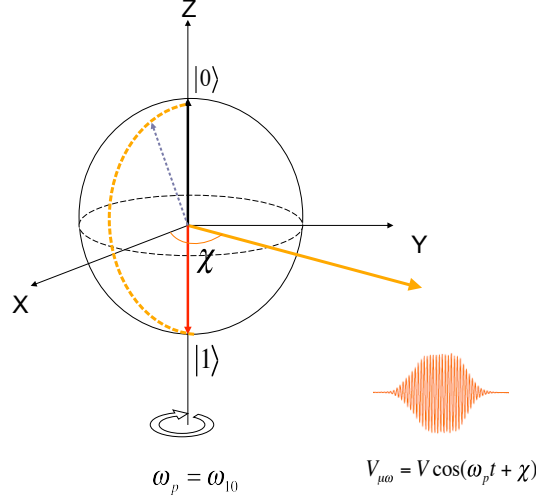


Figure 2.10: Nonadiabatic, resonant ( $\omega_p = \omega_{10}$ ) microwave pulses induce arbitrary state rotations around the  $x$  and  $y$ -axes in the Bloch sphere. The solid orange arrow indicates the rotation axis around a vector in the  $x$ - $y$  plane, which is determined by  $\chi$ . The dashed, orange line indicates the rotation path of the state.

In the charge regime at  $n_g = 0.5$ , we can approximate  $\hat{n} = \sigma_x$ ,

$$H_{dipole} = 2e\beta V_{\mu\omega} \hat{n} = 2e\beta V_{\mu\omega} \sigma_x, \quad (2.43)$$

where  $\beta = C_g/C_\Sigma$ . We assume that the SCB is driven by a cosine drive with the voltage amplitude  $V$ , frequency  $\omega_p$  and phase  $\chi$ ,

$$V_{\mu\omega} = V \cos(\omega_p t + \chi). \quad (2.44)$$

The dipole coupling Hamiltonian Eq. (2.43) then becomes,

$$H_{dipole} = \frac{1}{2} \hbar \Omega \sigma_x (e^{-i(\omega_p t + \chi)} + e^{i(\omega_p t + \chi)}), \quad (2.45)$$

where  $\hbar \Omega = 2e\beta V$ ,  $\sigma_x = \sigma_+ + \sigma_-$ . Making the rotating wave approximation (RWA), meaning we neglect the terms containing  $\sigma_+ e^{i(\omega_p t + \chi)}$  and  $\sigma_- e^{-i(\omega_p t + \chi)}$ , the Hamiltonian Eq. (2.45) becomes

$$H_{dipole} = \frac{1}{2} \hbar \Omega (\sigma_+ e^{-i(\omega_p t + \chi)} + \sigma_- e^{i(\omega_p t + \chi)}). \quad (2.46)$$

We recall that the two-level Hamiltonian is

$$H_0 = \frac{\hbar \omega_{10}}{2} \sigma_z. \quad (2.47)$$

In the interaction picture, the coupling Hamiltonian Eq. (2.46) becomes,

$$H^I = U_0 H_{dipole} U_0^\dagger = \frac{1}{2} \hbar \Omega (e^{-i\chi} \sigma_+ e^{-i\delta\omega_p t} + e^{i\chi} \sigma_- e^{i\delta\omega_p t}), \quad (2.48)$$

where  $\delta\omega_p = \omega_p - \omega_{10}$ ,  $U_0 = e^{iH_0 t/\hbar}$ . In particular, at resonance  $\delta\omega_p = 0$ , and zero phase  $\chi = 0$ , we have

$$H^I = \frac{1}{2} \hbar \Omega \sigma_x. \quad (2.49)$$

If we choose  $\chi = \pi/2$  and  $\delta\omega_p = 0$ , we have

$$H^I = \frac{1}{2} \hbar \Omega \sigma_y. \quad (2.50)$$

These interaction Hamiltonian generate rotations around the x and y axes, respectively. By controlling the phase  $\chi$ , we thus can realize arbitrary rotations around the x- and y-axes (Fig. 2.10). A continuous drive with fixed phase will result in Rabi oscillations [82].

## 2.3.2 A SCB in a 1D Open Transmission Line

### Classical Circuit Approximation

To understand the behavior of a qubit in a transmission line, we start by approximating the qubit as a classical oscillator. This classical circuit approximation is only valid for a weak incident power where we can replace the qubit with a linear harmonic oscillator, meaning that the incident field can only excite one level of the harmonic oscillator (see Fig. 2.1C). As shown in Eq. (1.12), a SQUID acts as a tunable inductance for low excitations. For small enough currents, it can be approximated by a linear inductor with inductance  $L_J = (\hbar/2e)^2/E_J$ . In Fig. 1.4B, we can model the capacitors of the transmon by only considering the capacitance between nearest electrodes (neglecting  $C_{02}, C_{13}, C_{03}$ ). The simplified circuit is shown in Fig. 2.11 A,B, where  $C_c = C_{10}C_{23}/(C_{10} + C_{23})$ ,  $C_{12} \equiv C_s$  (see Fig. 2.5),  $C_{JS} = C_s + C_J$ ,  $C_\Sigma = C_{JS} + C_c$ ,  $\beta = C_c/C_\Sigma$ . Therefore, Fig. 1.4B can be modeled as Fig. 2.11C at sufficiently low power. After some brief circuit analysis of Fig. 2.11C, we have

$$Z_{atom} = \frac{1}{j\omega C_c} + \left( j\omega C_{JS} + \frac{1}{j\omega L_J} \right)^{-1}; \quad (2.51)$$

$$Z_{eff} = \frac{Z_0 Z_{atom}}{Z_{atom} + Z_0}; \quad r = \frac{Z_{eff} - Z_0}{Z_{eff} + Z_0}. \quad (2.52)$$

where  $Z_{eff}$  is the impedance seen from the left hand transmission line in Fig. 2.11C. Assuming the probe frequency  $\omega$  is close to the resonance frequency  $\omega_0$ , we get

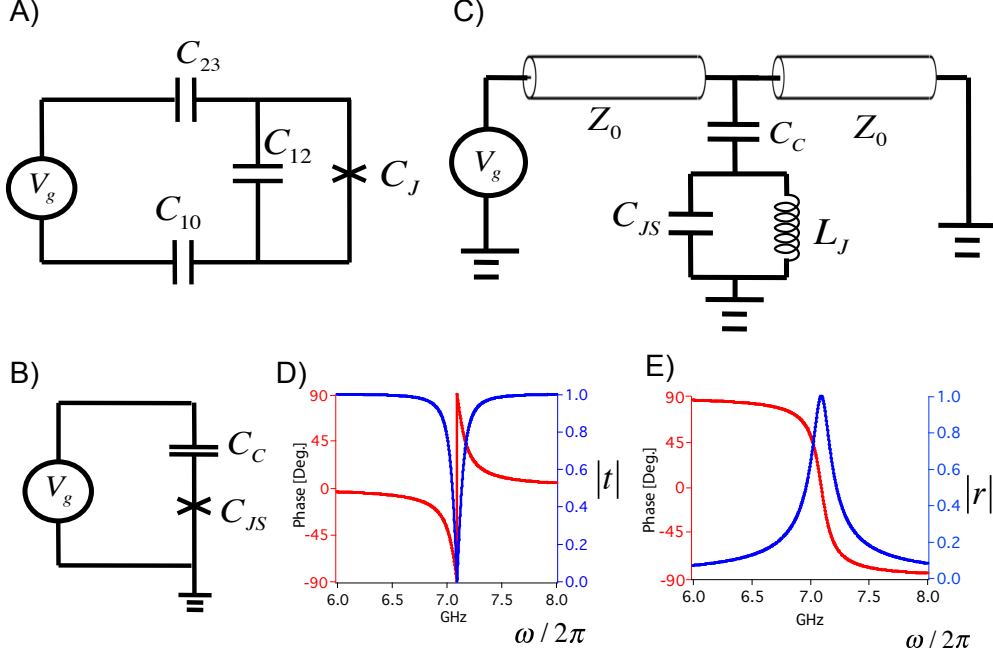


Figure 2.11: A) Circuit model of Fig. 1.4B. B) Simplified circuit model of (A). C) Classical circuit approximation of transmon in a 1D transmission line, where the Josephson junction is replaced by  $L_J$ . D) Transmission coefficient as a function of frequency. Magnitude and phase response are shown in blue and red, respectively. E) Reflection coefficient as a function of frequency. Magnitude and phase response are shown in blue and red, respectively.

$$r \simeq -\frac{1 - i\delta\omega/\Gamma}{1 + \delta\omega^2/\Gamma^2}; \quad t \simeq 1 - \frac{1 - i\delta\omega/\Gamma}{1 + \delta\omega^2/\Gamma^2}, \quad (2.53)$$

where  $\delta\omega = \omega - \omega_0$  and

$$\Gamma = \frac{\omega_0^2 C_c^2 Z_0}{4(C_c + C_{JS})} = \frac{\beta^2 Z_0}{4L_J}; \quad (2.54)$$

$$\omega_0 = \frac{1}{\sqrt{L_J(C_{JS} + C_c)}} = \frac{\sqrt{8E_C E_J}}{\hbar}.$$

The applied power must be much less than the product of one photon energy  $\hbar\omega_0$  and the coupling rate  $\Gamma$ ,  $P_{\text{applied}} \ll \hbar\omega_0\Gamma$ . As the applied power increases, this classical analysis breaks down, as we will show in the next section. The

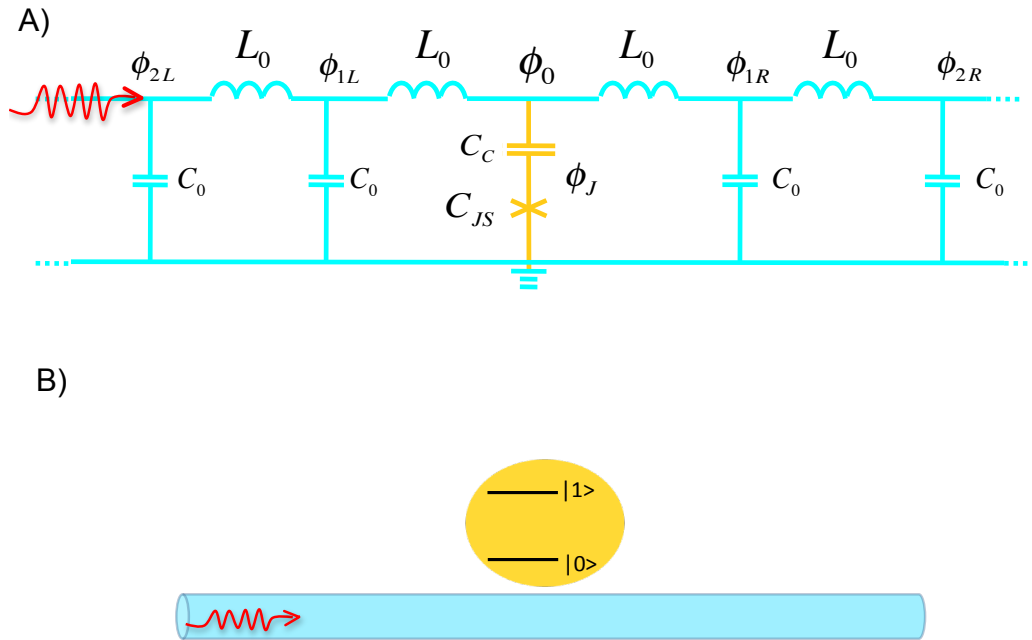


Figure 2.12: A) Quantum circuit model of a SCB/transmon in a 1D open transmission line. B) A photon (red) traveling along the 1D waveguide (Blue) interacts with a two-level atom (yellow).

theory response is plotted in Fig. 2.11 D,E based on the following parameters:  $L_J = 15.2$  nH,  $C_{JS} = 8$  fF,  $C_c = 25$  fF and  $Z_0 = 50 \Omega$ .

### Quantum Circuit Analysis

The system is treated quantum mechanically by B. Peropadre *et al.* [83] in Appended paper V. In this section, we show the main results of analysis. We consider a SCB capacitively coupled to the transmission line at  $x = 0$ , as shown in Fig. 1.4B. The corresponding quantum circuit model is shown in Fig. 2.12A. We use the following steps to solve this problem (See appendix C).

1. From the circuit model, derive the Hamiltonian of the system.
2. Write down the equations of motion for the circuit degrees of freedom.
3. Identify the equations of motion as a quantum Langevin equation (QLE)[84].
3. From the QLE, write down the master equation for the density matrix.
4. Find the solution for the elements of density matrix in the steady state.
5. Find the outgoing fields in terms of average of the appropriate operator.
6. Derive  $r$  and  $t$  from the input-output relations.

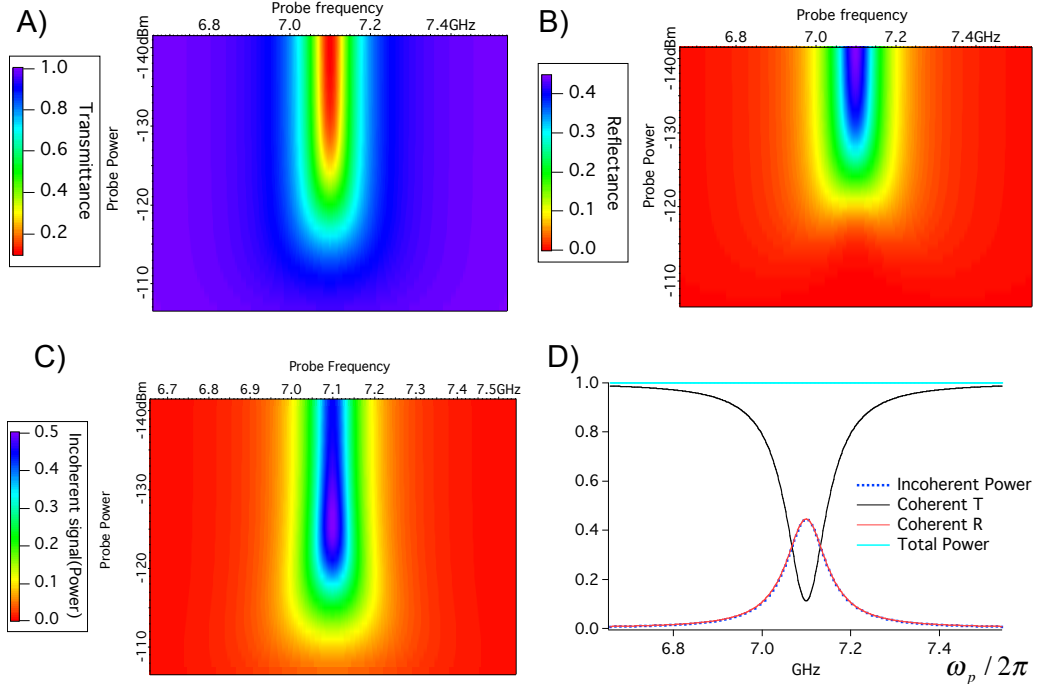


Figure 2.13: Theory plots of how the scattered power is distributed. A) Transmittance (in color scale) as function of probe frequency and probe power. B) Reflectance (in color scale) as function of probe frequency and probe power. C) Incoherent signal ( $1 - R^{coh} - T^{coh}$ ), in color scale, as function of probe frequency and probe power. D) Line cuts along the lowest probe power of A, B, C and the sum of them. It is a coincidence that the incoherence power is almost the same as the coherent reflected power.

From appendix C and including effect of pure dephasing, the voltage transmission coefficient  $t$  and the voltage reflection coefficient  $r$  can be expressed in the following way [22, 85],

$$t = 1 - r_0 \frac{1 - i(\delta\omega_p/\gamma_{10})}{1 + \delta\omega_p^2/\gamma_{10}^2 + \Omega_p^2/\Gamma_{10}\gamma_{10}}; \quad (2.55)$$

$$r = -r_0 \frac{1 - i(\delta\omega_p/\gamma_{10})}{1 + \delta\omega_p^2/\gamma_{10}^2 + \Omega_p^2/\Gamma_{10}\gamma_{10}}, \quad (2.56)$$

where

$$\Omega_p = \frac{\sqrt{2}eC_c}{2\hbar(C_c + C_J)} V_p = \frac{\pi}{\sqrt{2}} \beta \frac{V_p}{\Phi_0}; \quad (2.57)$$

$$\Gamma_{10} = \frac{e^2 \omega_{10} C_c^2 Z_0}{\hbar (C_c + C_J)^2} = 2\pi \omega_{10} \beta^2 \frac{Z_0}{R_k}, \quad (2.58)$$

$$r_0 = 1/(1 + 2\Gamma_{\phi,10}/\Gamma_{10}). \quad (2.59)$$

The Rabi frequency  $\Omega_p$  is proportional to the voltage amplitude of the drive,  $V_p$ .  $\Gamma_{10}$  and  $\Gamma_{\phi,10}$  are the 1-0 relaxation rate and pure dephasing rate of the atom, respectively.  $\gamma_{10} = \Gamma_{10}/2 + \Gamma_{\phi,10}$  is the 1-0 decoherence rate.  $r_0$  is the maximal reflection amplitude.  $\delta\omega_p = \omega_p - \omega_{10}$  is the detuning between the drive and the 0-1 transition frequency of the atom.  $R_k = h/e^2$  is the quantum resistance.  $\Phi_0 = h/2e$  is the flux quantum. Eq. (2.55) and (2.56) are the same as the classical circuit approach in Eq. (2.53), when  $\Omega_p \ll \gamma_{10}$  and  $\Gamma_{\phi,10} \ll \Gamma_{10}$ . We can define the reflectance  $R = |r|^2$  and transmittance  $T = |t|^2$ . Fig. 2.13 A,B shows theory plots of Eq. (2.55), (2.56), assuming  $\Gamma_{10}/2\pi = 73$  MHz,  $\Gamma_{\phi,10}/2\pi = 18$  MHz and  $\omega_{10}/2\pi = 7.1$  GHz, in agreement with the measured sample discussed in Fig. 4.2.

### Coherent and Incoherent

Considering the on-resonance case of Eq. (2.55) and Eq. (2.56), the coherent reflectance and coherent transmittance become,

$$R^{coh} = r_0^2 \frac{1}{(1 + \Omega_p^2/\Gamma_{10}\gamma_{10})^2}; \quad (2.60)$$

$$T^{coh} = \frac{(1 + \Omega_p^2/\Gamma_{10}\gamma_{10} - r_0)^2}{(1 + \Omega_p^2/\Gamma_{10}\gamma_{10})^2}. \quad (2.61)$$

We see that the total coherent power is less than the incoming power even if  $r_0 = 1$ ,

$$R^{coh} + T^{coh} = 1 - \frac{2r_0(1 - r_0 + \Omega_p^2/\Gamma_{10}\gamma_{10})}{(1 + \Omega_p^2/\Gamma_{10}\gamma_{10})^2} < 1. \quad (2.62)$$

This means that some power is missing! This missing power is actually the incoherent emission by the atom (See Fig. 2.13C), which is emitted equally in the reflected and transmitted channels (Fig. 2.14). Since the power is conserved, the normalized incoherent power in the reflected channel,  $R^{inc}$ , and transmitted channel,  $T^{inc}$ , can then be expressed as,  $R^{inc} = T^{inc} = (1 - R^{coh} - T^{coh})/2$ . Since the incoherent signal has random phase, its average voltage is zero. This gives us an interesting phenomenon, which can be measured,  $\langle V_R \rangle^2 < \langle V_R^2 \rangle$  (Fig. 2.14B). We describe the measurement of this effect in Chapter 4.1.1. The origin of the incoherent scattering comes from the Mollow triplet, as we will discuss in the next section.

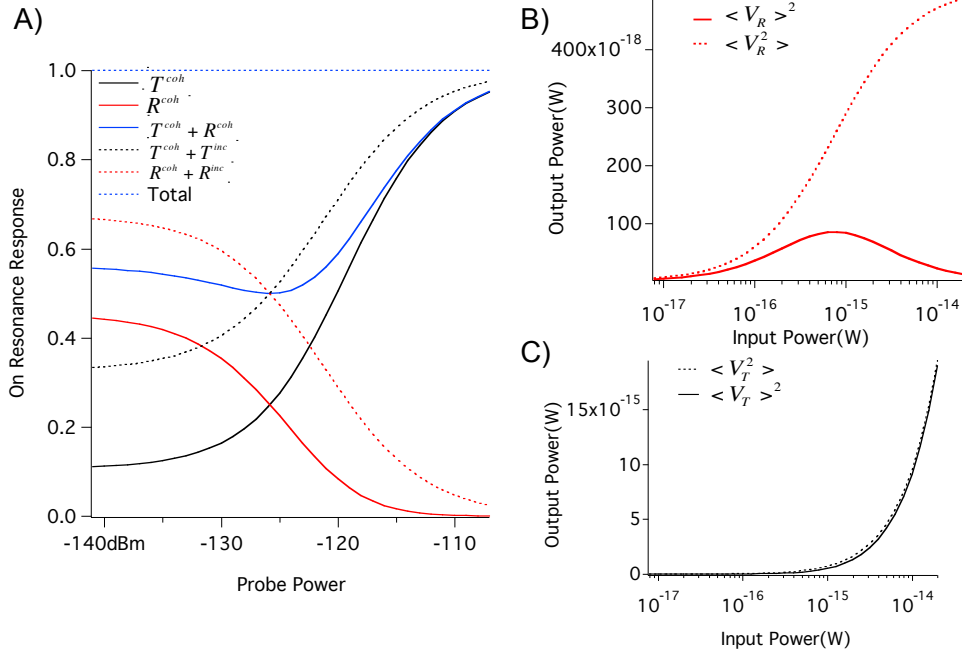


Figure 2.14: A) Calculated transmittance/reflectance on resonance as a function of probe power. Solid black and red curves show the coherent part of the transmittance/reflectance and are the line cut of Fig. 2.13A and B along 7.1 GHz, respectively. Dashed black and red curves are the transmittance, coherent+incoherent, and reflectance, coherent+incoherent, respectively. B) Total reflected power (incoherent+coherent)  $\langle V_R^2 \rangle$  and coherent reflected power  $\langle V_R \rangle^2$  as a function of input power C) Total transmitted power (incoherent+coherent)  $\langle V_T^2 \rangle$  and coherent transmitted power  $\langle V_T \rangle^2$  as a function of input power. All the plots here use the same parameters as in Fig. 2.13.

### 2.3.3 A SCB in a Quantized Field: Dressed States

Consider a quantized field with the frequency  $\omega_p \simeq \omega_{10}$  [86], according to Eq. (2.6), we have

$$\hat{V} = \frac{\hat{Q}}{C} = V_0(a + a^\dagger), \quad (2.63)$$

where

$$V_0 = \sqrt{\frac{\hbar\omega_p}{2C}}. \quad (2.64)$$

Note that I interchanged the phase and charge in Eq. (2.6), since, in a SCB, the charge is well defined and the charging energy acts as potential energy. From

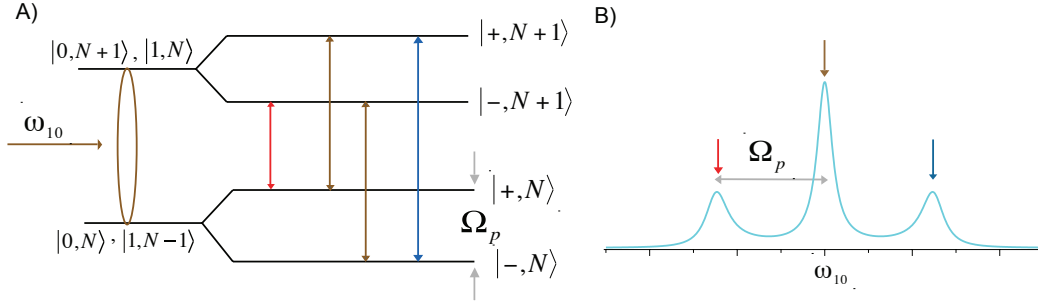


Figure 2.15: A) A two-level atom in a quantized field gives the Mollow Triplet: three possible transitions, indicated by red, brown and blue arrows, between these four dressed states ( $|+, N+1\rangle$ ,  $|-, N+1\rangle$ ,  $|+, N\rangle$ ,  $|-, N\rangle$ ). The experimental observation of this triplet is described in Chapter 4.1.3. The emission signal from the triplet is incoherent. B) Cartoon of the Mollow Triplet spectrum.

Eq. (2.43) and Eq. (2.63) we have

$$H_{dipole} = \hbar g(a + a^\dagger)\sigma_x, \quad (2.65)$$

where  $g = e\beta V_0$ . One can make the RWA so that,

$$(a + a^\dagger)\sigma_x \simeq a\sigma_+ + a^\dagger\sigma_-. \quad (2.66)$$

Combining the Hamiltonian for the two-level atom, the field and the interaction, we get the *Jaynes – Cummings* Hamiltonian [87]

$$H = \frac{1}{2}\hbar\omega_{10}\sigma_z + \hbar\omega_p a^\dagger a + \hbar g(a\sigma_+ + a^\dagger\sigma_-), \quad (2.67)$$

where  $\hbar\omega_{10}$  denotes the transition energy between the ground and excited state.

If there is no coupling,  $g = 0$ , the Hamiltonian Eq. (2.67) in the Hilbert space spanned by  $|0, N+1\rangle, |1, N\rangle$  has the eigenenergies

$$E_{0, N+1} = (N+1)\hbar\omega_p - \frac{1}{2}\hbar\omega_{10}; \quad (2.68)$$

$$E_{1, N} = N\hbar\omega_p + \frac{1}{2}\hbar\omega_{10}, \quad (2.69)$$

where  $E_{0, N+1}$  and  $E_{1, N}$  are the diagonal elements of the Hamiltonian in the  $|0, N+1\rangle, |1, N\rangle$  basis. Next, we consider the  $g \neq 0$  case. The interaction term in the Hamiltonian Eq. (2.67) conserves excitation number and only couples the nearest neighbor photon states,

$$\langle 0, N+1 | g(a\sigma_+ + a^\dagger\sigma_-) | 1, N \rangle = g\sqrt{N+1}; \quad (2.70)$$

$$\langle 1, N | g(a\sigma_+ + a^\dagger\sigma_-) | 0, N + 1 \rangle = g\sqrt{N + 1}. \quad (2.71)$$

In the two dimensional subspace, spanned by  $|0, N + 1\rangle$ ,  $|1, N\rangle$ , the Jaynes Cumings Hamiltonian looks like,

$$H_{N+1} = \hbar \begin{pmatrix} N\omega_p + \frac{1}{2}\omega_{10} & g\sqrt{N + 1} \\ g\sqrt{N + 1} & (N + 1)\omega_p - \frac{1}{2}\omega_{10} \end{pmatrix}, \quad (2.72)$$

Considering the on resonance case,  $\omega_p = \omega_{10}$ , we get the eigenenergies and the dressed eigenstates,

$$E_{\pm, N+1} = (N + \frac{1}{2})\hbar\omega_p \pm \hbar g\sqrt{N + 1}; \quad (2.73)$$

$$|+, N + 1\rangle = \frac{1}{\sqrt{2}} (|0, N + 1\rangle + |1, N\rangle); \quad (2.74)$$

$$|-, N + 1\rangle = \frac{1}{\sqrt{2}} (|0, N + 1\rangle - |1, N\rangle). \quad (2.75)$$

The level splitting is then given by the Rabi frequency,  $\hbar\Omega_{p, N+1} = 2\hbar g\sqrt{N + 1}$ . Similarly, we have the eigenenergies and the dressed eigenstates for  $H_N$ ,

$$E_{\pm, N} = (N - \frac{1}{2})\hbar\omega_p \pm \hbar g\sqrt{N}; \quad (2.76)$$

$$|+, N\rangle = \frac{1}{\sqrt{2}} (|0, N\rangle + |1, N - 1\rangle); \quad (2.77)$$

$$|-, N\rangle = \frac{1}{\sqrt{2}} (|0, N\rangle - |1, N - 1\rangle). \quad (2.78)$$

The level splitting is  $\hbar\Omega_{p, N} = 2\hbar g\sqrt{N}$ . For large photon number  $N \gg 1$ , the Rabi splitting of adjacent levels will be the same,  $\Omega_p \equiv \Omega_{p, N+1} \simeq \Omega_{p, N}$  (see Fig. 2.15A). There are three different possible transitions between these dressed states [88], described in Eq. (2.74), Eq. (2.75), Eq. (2.77) and Eq. (2.78). They have been observed in atomic physics, and named the Mollow Triplet [22, 89, 90] (see Fig. 2.15B). This triplet resonance can be probed using a weak field at the corresponding transition frequencies or directly observed in the spectrum emitted by the atom, known as fluorescences. These emitted fluorescences are incoherent, except at  $\omega_{10}$ . We will discuss the experimental results in Chapter 4.

### 2.3.4 A SCB at the end of a 1D Transmission Line

So far, we have considered a two-level artificial atom in a 1D open transmission line. In this section, we are interested in how geometric constraints affect the interaction between a two-level atom and an EM field. In particular, we introduce a boundary condition, see Fig. 2.16A,B. This boundary condition acts as an infinite potential, where the propagating photons can not pass through. Therefore, all photons will be reflected. We consider the configuration in Fig. 2.16B with the SCB embedded at the end of a 1D transmission line. In this configuration, the SCB is always at a voltage antinode. The corresponding quantum circuit model is shown in Fig. 2.16C. As we will show later, all the field will be reflected either coherently or incoherently, because of the boundary condition.

From the theoretical point of view, this configuration is the same as for the 1D open transmission line case, with only one difference: the emitted fields from the atom can only propagate in one direction for the single-ended transmission line, but two directions for the open transmission line. The complex reflection coefficient,  $r_{p,2}$ , can be expressed as,

$$r_{p,2} = 1 - \frac{\Gamma_{10}}{\gamma_{10}} \frac{1 - i(\delta\omega_p/\gamma_{10})}{1 + \delta\omega_p^2/\gamma_{10}^2 + \Omega_p^2/\Gamma_{10}\gamma_{10}}, \quad (2.79)$$

where the definition of all the parameters is the same as that in Eq. (2.55) and Eq. (2.56). Similar to Eq. (2.55) and Eq. (2.56), this expression only contains the coherently reflected signal.

For a weak resonant probe ( $\Omega_p \ll \gamma_{10}$ ,  $\omega_p = \omega_{10}$ ), Eq. (2.79) becomes [91]

$$r_{p,2} = 1 - \frac{2}{1 + 2\Gamma_{\phi,10}/\Gamma_{10}}. \quad (2.80)$$

In the case of strong coupling, where  $\Gamma_{10} \gg \Gamma_{\phi,10}$ , this leads to  $|r_{p,2}| = 1$ . In other words, all of the probe field is coherently reflected by the atom. Thus, the atom acts as a mirror for a weak resonant probe. According to Eq. (2.79), for a strong resonant probe, where  $\Omega_p \gg \gamma_{10}$ ,  $\omega_p = \omega_{10}$ , we see that also in this case  $|r_{p,2}| = 1$ . For a resonant probe, where  $\omega_p = \omega_{10}$  with  $\Omega_p = \sqrt{\Gamma_{10}^2 - \Gamma_{10}\gamma_{10}}$ , we see  $|r_{p,2}| = 0$ . In Fig. 2.17A and B, we plot the magnitude and phase of  $r_{p,2}$  as a function of  $\omega_p$  and  $\Omega_p$  according to Eq. (2.79), with the parameters shown in the caption. In Fig. 2.17C, we show the vertical resonant line cut of Fig. 2.17A. For a weak resonant probe, where  $\Omega_p \ll \gamma_{10}$ ,  $\omega_p = \omega_{10}$ , the incident field is reflected by the atom with  $|r_{p,2}| \simeq 0.52$ .  $|r_{p,2}|$  is determined by the ratio between the pure dephasing and the relaxation rate (see Eq. (2.80)). As the probe amplitude increases, there is a perfect destructive interference between the field reflected by the atom and the field reflected by the boundary condition. This leads to  $|r_{p,2}| \simeq 0$ ,

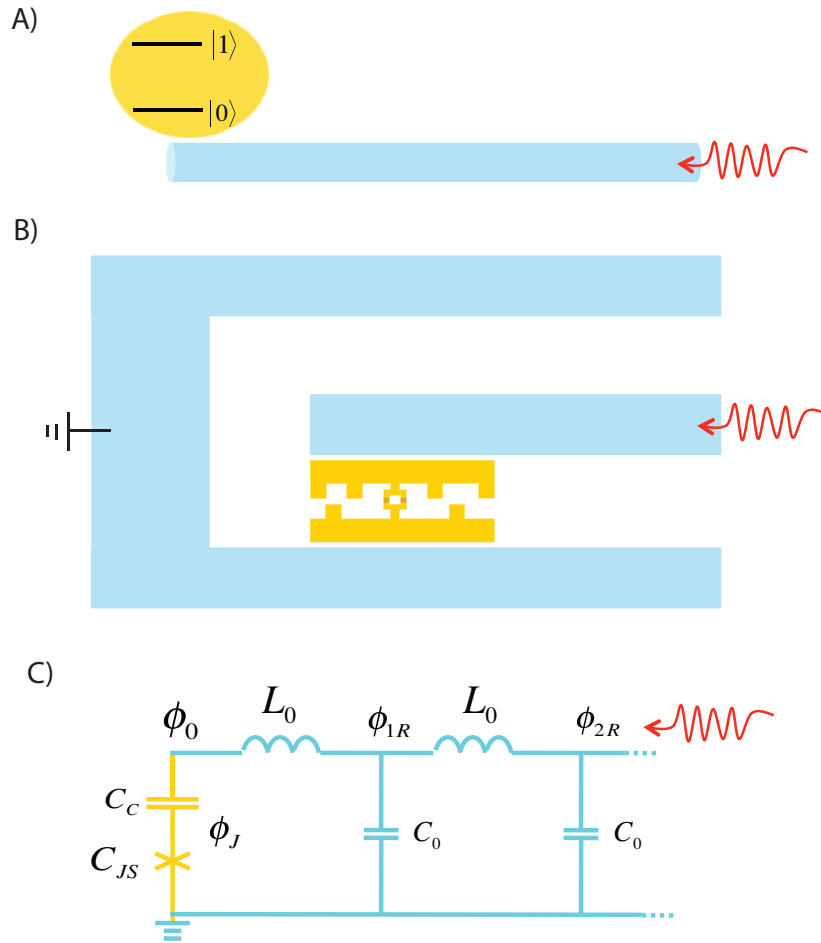


Figure 2.16: A) A photon (red) traveling along a 1D single-end waveguide (Blue) interacts with the two-level atom (yellow). B) SCB/transmon is embedded at the end of a 1D transmission line. C) Quantum circuit model of B.

when  $\Omega_p \sim 2\pi \times 46$  MHz, as expected. For a very high probe field, where  $\Omega_p \gg \gamma_{10}$ , the atom is saturated. All the field is reflected by the boundary condition, this gives  $|r_{p,2}| = 1$ . The missing signal is emitted incoherently with a random phase. This effect is the same as for an atom in an open transmission line, as shown in Fig. 2.14. To distinguish between the coherent and incoherent signal, we can compare the phase sensitive average  $\langle V \rangle^2$  and phase insensitive average  $\langle V^2 \rangle$ , where  $V$  is the voltage amplitude of the signal. In Fig. 2.17D, we show the horizontal line cut of Fig. 2.17A and B for  $\Omega_p \ll \gamma_{10}$ , we see that the phase shift (blue curve) between on and off resonance is  $\pi$  radians.

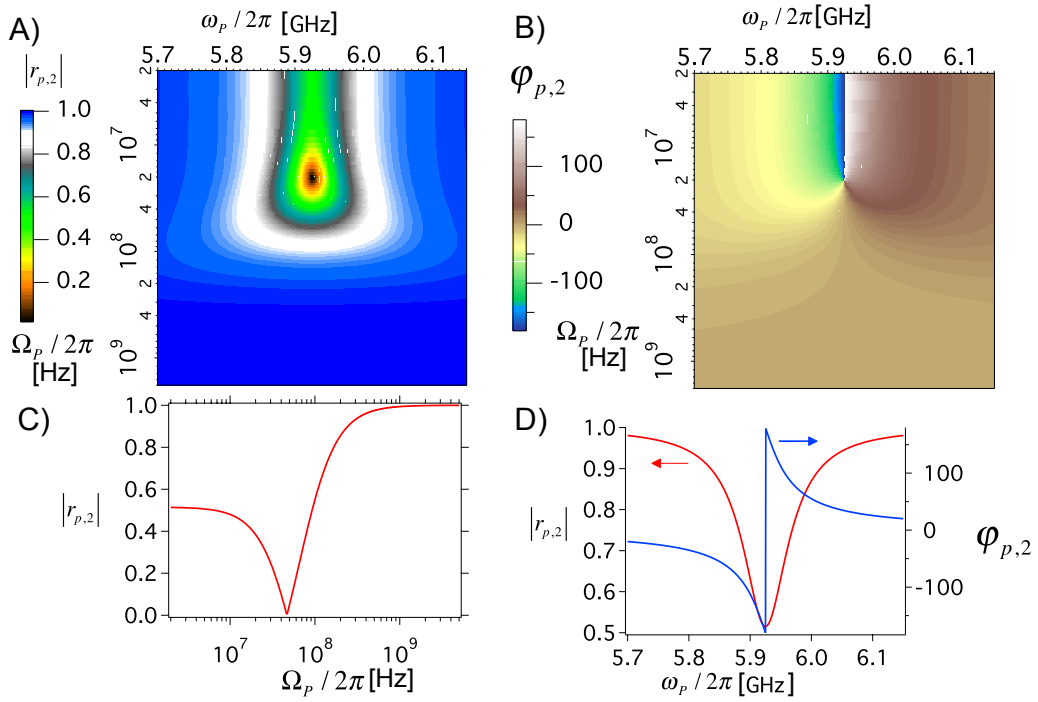


Figure 2.17:  $r_{p,2}$  as a function of  $\omega_p$  and  $\Omega_p$ . A) Magnitude response. B) Phase response. C) Vertical line cut at  $\omega_p = \omega_{10}$  from A. This shows  $|r_{p,2}|$  as a function of  $\Omega_p$ . D) Horizontal line cut from A,B with  $\Omega_p \ll \gamma_{10}$ . The magnitude and phase response of  $r_{p,2}$  are displayed in red and blue, respectively. All curves are based on the following parameters:  $\omega_{10}/2\pi = 5.92$  GHz,  $\Gamma_{10}/2\pi = 80$  MHz and  $\Gamma_{\phi,10}/2\pi = 12.8$  MHz, corresponding to  $\gamma_{10}/2\pi = 52.8$  MHz.

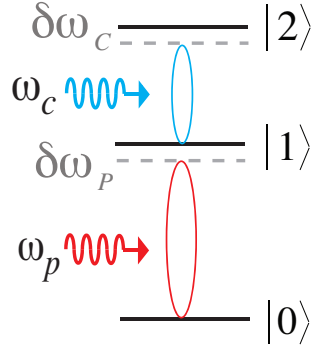


Figure 2.18: Interaction between two EM Fields via a Three-Level Atom. The probe field and the control fields are at  $\omega_p \sim \omega_{10}$ ,  $\omega_c \sim \omega_{21}$ , respectively. The amplitude of the probe and control fields are proportional to  $\Omega_p$  and  $\Omega_c$ , respectively. For  $\Omega_p \ll \gamma_{10}$  and  $\Omega_c \gg \gamma_{10}$ , we see electromagnetically induced transparency from the Autler-Townes splitting (see Section 2.4.1). For  $\Omega_c \ll \gamma_{21}$ ,  $\Omega_p \ll \gamma_{10}$ , we see the cross-Kerr effect (see Section 2.4.2).

## 2.4 Interaction of Two EM Fields via a Three-Level Atom

In Section 2.3, we only used the two lowest energy levels. In this section, we also use the third energy level. We consider a three-level atom under two drives, the probe field at  $\omega_p$  and the control field at  $\omega_c$  (see Fig. 2.18). Within the rotating wave approximation, described in detail in Appendix B, the Hamiltonian is given by

$$H = -\frac{\hbar}{2} \begin{pmatrix} 0 & \Omega_p & 0 \\ \Omega_p & 2\delta\omega_p & \Omega_c \\ 0 & \Omega_c & 2(\delta\omega_p + \delta\omega_c) \end{pmatrix}, \quad (2.81)$$

where  $\Omega_p, \Omega_c$  are the Rabi frequencies of the probe and the control fields respectively. We also define two different detunings  $\delta\omega_p = \omega_p - \omega_{10}$  and  $\delta\omega_c = \omega_c - \omega_{21}$ . The time evolution of the density matrix,  $\rho$ , is given by the von-Neumann equation

$$\hbar\partial_t\rho = -i[H, \rho], \quad (2.82)$$

where

$$\rho = \begin{pmatrix} \rho_{00} & \rho_{01} & \rho_{02} \\ \rho_{10} & \rho_{11} & \rho_{12} \\ \rho_{20} & \rho_{21} & \rho_{22} \end{pmatrix}. \quad (2.83)$$

From Eq. (2.82), comparing each component of the matrix, we get 9 equations. In addition, the off-diagonal elements,  $\rho_{ij}$  ( $i \neq j$ ), are subject to a pure exponential

decay with rate  $\gamma_{ij}$ . For the steady state,  $\partial_t \rho_{ij} = 0$ , ( $i, j \in 0, 1, 2$ ). This gives us the following equations,

$$\partial_t \rho_{10} = \frac{i}{2} (2\delta\omega_p \rho_{10} + \Omega_p(\rho_{00} - \rho_{11}) + \Omega_c \rho_{20}) - \gamma_{10} \rho_{10} = 0; \quad (2.84)$$

$$\partial_t \rho_{20} = \frac{i}{2} (\rho_{10} \Omega_c - \Omega_p \rho_{21} + 2\rho_{20}(\delta\omega_p + \delta\omega_c)) - \gamma_{20} \rho_{20} = 0; \quad (2.85)$$

$$\partial_t \rho_{21} = \frac{i}{2} (\Omega_c(\rho_{11} - \rho_{22}) - \rho_{20} \Omega_p + 2\delta\omega_p \rho_{21}) - \gamma_{21} \rho_{21} = 0. \quad (2.86)$$

From Eq. (2.85), we have

$$\rho_{20} = \frac{i\Omega_c}{2[\gamma_{20} - i(\delta\omega_p + \delta\omega_c)]} \rho_{10} - \frac{i\Omega_p}{2[\gamma_{20} - i(\delta\omega_p + \delta\omega_c)]} \rho_{21}. \quad (2.87)$$

In the case of the control field being much stronger than the probe field,  $\Omega_c \gg \Omega_p$ , the second term of Eq. (2.87) can be neglected,

$$\rho_{20} \simeq \frac{i\Omega_c}{2[\gamma_{20} - i(\delta\omega_p + \delta\omega_c)]} \rho_{10}. \quad (2.88)$$

We substitute Eq. (2.88) into Eq. (2.84). For the steady state, with  $\Omega_p \ll \gamma_{10}$ , we can approximate  $\rho_{11} \simeq 0$ ,  $\rho_{00} \simeq 1$ . Then Eq. (2.84) becomes

$$\rho_{10} \simeq \frac{i\Omega_p}{2(\gamma_{10} - i\delta\omega_p) + \Omega_c^2/[2\gamma_{20} - 2i(\delta\omega_p + \delta\omega_c)]}. \quad (2.89)$$

From the input-output theory [84], the output coherent field  $\alpha_{out}$  is the sum of incoming coherent field  $\alpha_{in}$  and the field emitted by the atom:

$$\alpha_{out} = \alpha_{in} + i\sqrt{\frac{\Gamma_{10}}{k_n}} \langle \sigma_- \rangle, \quad (2.90)$$

where  $k_n$  is the number of output channels,  $\sigma_- = |0\rangle\langle 1|$ .  $\Omega_p$  is related to the amplitude of coherent drive  $\alpha$  and  $\Gamma_{10}$  [92]:

$$\frac{\Omega_p}{2} = \alpha\sqrt{\frac{\Gamma_{10}}{k_n}}. \quad (2.91)$$

So far, we have considered a general case, without introducing any geometry confinement. We now consider the case of the a three-level atom being put in an open transmission line with two emission channels,  $k_n = 2$ . From Eq. (2.90) and Eq. (2.91), the transmission coefficient of the probe is given by,

$$t_{p,1} = 1 + i\frac{\Gamma_{10}}{\Omega_p} \langle \sigma_- \rangle. \quad (2.92)$$

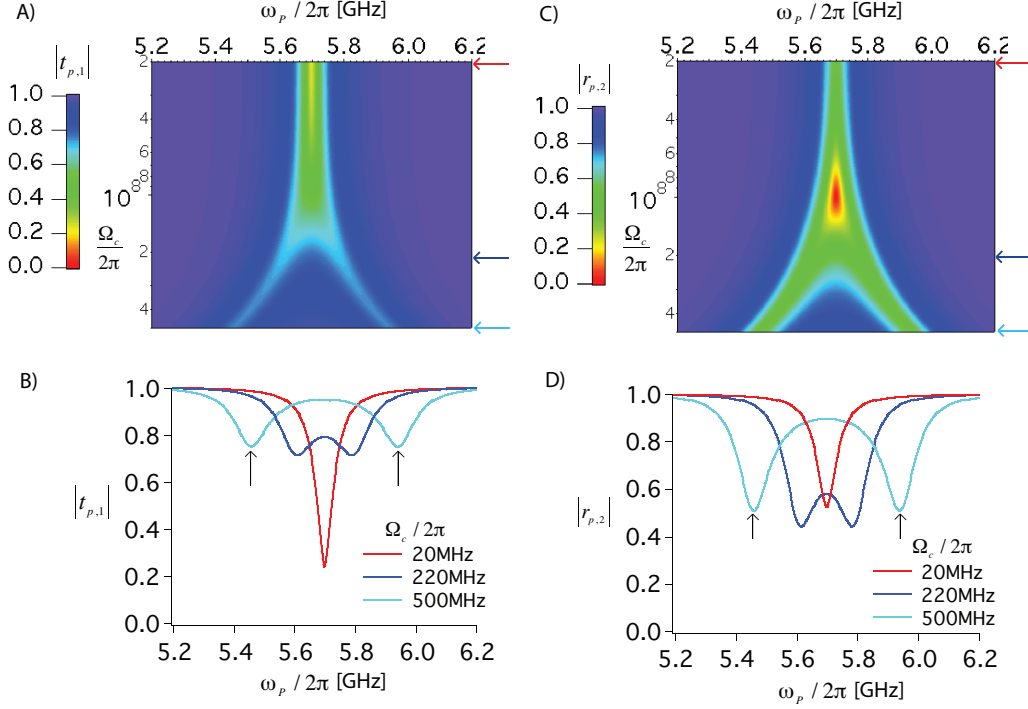


Figure 2.19:  $|t_{p,1}|$  and  $|r_{p,2}|$  as a function of  $\omega_p$  and  $\Omega_c$  for a weak probe, where  $\Omega_p \ll \gamma_{10}$ , for  $k_n = 2$  and  $k_n = 1$ , respectively. A) and B) Three-level atom in an open transmission line,  $k_n = 2$ . We see electromagnetically Induced Transparency (EIT) from the Autler-Townes splitting (ATS). C) and D) Three-level atom at the end of transmission line,  $k_n = 1$ . The black arrows in B) and D) indicate the Autler-Townes splitting. All the plots are based on Eq. (2.94) and Eq. (2.96) with the following parameters:  $\Gamma_{10}/2\pi = 70$  MHz,  $\Gamma_{10,\phi}/2\pi = 10$  MHz,  $\omega_{10}/2\pi = 5.7$  GHz,  $\gamma_{20}/2\pi = 100$  MHz.  $\delta\omega_c/2\pi = 0$ .

In the 0-1 subspace, we have,

$$\langle \sigma_- \rangle = \text{Tr}(\sigma_- \rho) = \rho_{10}. \quad (2.93)$$

From Eq. (2.92), Eq. (2.93) and Eq. (2.89), the probe transmission coefficient is given by

$$t_{p,1} = 1 - \frac{\Gamma_{10}}{2(\gamma_{10} - i\delta\omega_p) + \Omega_c^2 / [2\gamma_{20} - 2i(\delta\omega_p + \delta\omega_c)]}. \quad (2.94)$$

For the three-level atom positioned at the end of the transmission line, there is only one emission channel and thus  $k_n = 1$ . From Eq. (2.90) and Eq. (2.91), the

reflection coefficient is given by,

$$r_{p,2} = 1 + i \frac{2\Gamma_{10}}{\Omega_p} \langle \sigma_- \rangle. \quad (2.95)$$

The factor of 2 in front of the second term is a consequence of having only one emission channel for the atom. From Eq. (2.89), Eq. (2.95) and Eq. (2.93), we have the reflection coefficient at  $\omega_p$

$$r_{p,2} = 1 - \frac{2\Gamma_{10}}{2(\gamma_{10} - i\delta\omega_p) + \Omega_c^2 / [2\gamma_{20} - 2i(\delta\omega_p + \delta\omega_c)]}. \quad (2.96)$$

Depending on different regimes of  $\Omega_c$ , we observe different quantum-optical effects, these effects originate from photon-photon interaction via the three-level atom. In the next section, we will discuss Electromagnetically Induced Transparency (EIT) from the Autler-Townes splitting (ATS) in the regime where  $\Omega_p \ll \gamma_{10}$  and  $\Omega_c \gg \gamma_{20}$ . Furthermore, in Section 2.4.2, we investigate the cross-Kerr effect in the regime where  $\Omega_p \ll \gamma_{10}$  and  $\Omega_c \ll \gamma_{21}$ .

### 2.4.1 The Electromagnetically Induced Transparency

From Eq. (2.94), considering the case when both the probe and the control field are on resonance ( $\delta\omega_p = \delta\omega_c = 0$ ), we see that the role of the Rabi frequency of the control field,  $\Omega_c$ , is to enhance the  $|t_{p,1}|$  at  $\omega_p = \omega_{10}$ . For  $\Omega_c \gg \gamma_{20}$ , this leads to  $|t_{p,1}| = 1$  (see Fig. 2.19A,B). This is an example of electromagnetically induced transparency (EIT) [51, 93]. In addition, with strong  $\Omega_c$ , we also see the Autler-Townes splitting (ATS), (see Fig. 2.19B,D) [51]. This will be discussed experimentally in Chapter 4.1.3.

### 2.4.2 The Cross-Kerr Effect

The cross-Kerr effect refers to the interaction between two EM fields via a nonlinear medium. The nonlinear medium used here is our three-level artificial atom. We are interested in the cross-Kerr phase shift,  $\Delta\varphi_p = \varphi_p(\Omega_c) - \varphi_p(\Omega_c = 0)$ , where  $\varphi_{p,1} = \arg(t_{p,1})$  for a transmon in a 1D open transmission line,  $\varphi_{p,2} = \arg(r_{p,2})$  for a transmon at the end of a 1D transmission line,  $t_{p,1}$  and  $r_{p,2}$  are expressed in Eq. (2.94) and Eq. (2.96), respectively. In Appendix F, we calculate  $t_{p,1}$  and  $r_{p,2}$ , without assuming  $\Omega_c \gg \Omega_p$ . Typically, the Kerr phase shift is expressed as

$$\Delta\varphi_p = KP_c, \quad (2.97)$$

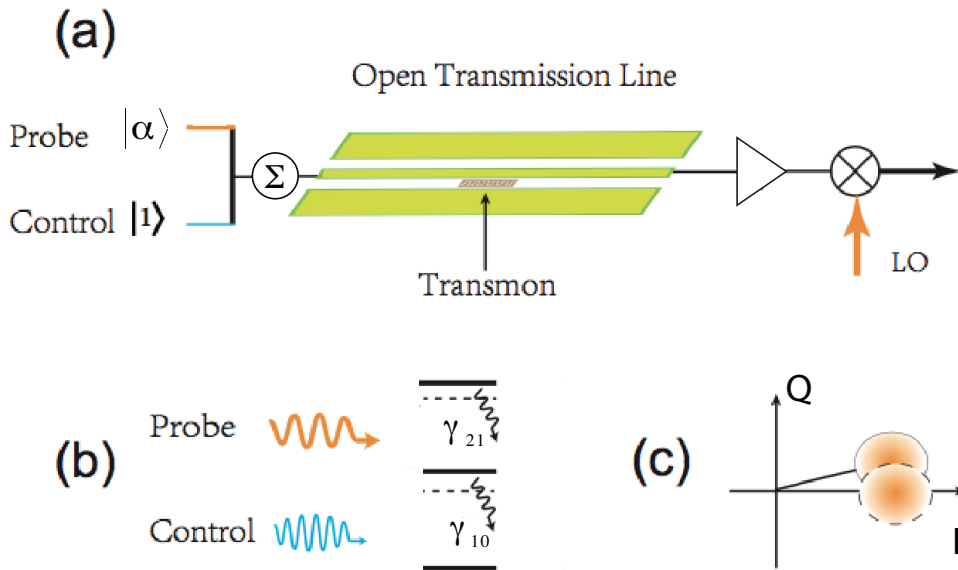


Figure 2.20: (a) Cartoon of the setup for a single photon detector. A microwave photon source emits a single-photon Fock state (blue) into a 1D planar transmission line with a three-level transmon embedded in it. We combine the coherent probe and the Fock state into the same input port. After interacting with transmon, we use heterodyne detection to detect the probe field. (b) Transmon level structure. The upper transition of the transmon is coupled a coherent microwave field (probe) and its lower transition is coupled to the Fock state. Note that we interchange the probe and control field, as compared to Fig. 2.18, because this configuration theoretically gives a better cross-Kerr effect. The interaction induced phase shift in the probe field is detected by heterodyne detection. (c) Cartoon of the Kerr-induced probe displacement in phase space. Figures borrowed from appended paper VI.

for weak control power  $P_c$ , where  $\Omega_c \ll \gamma_{21}$ , and weak probe power  $P_p$ , where  $\Omega_p \ll \gamma_{10}$ . The proportional constant  $K$  is the Kerr coefficient.  $P_c$  can be expressed in terms of the average number of control photons  $\langle N_c \rangle$  per interaction time,  $\langle N_c \rangle = 2\pi P_c / (\hbar\omega_c \Gamma_{21})$ . Eq. (2.97) indicates that  $\Delta\varphi_p$  is proportional to  $\langle N_c \rangle$ . We observe this effect in Chapter 4.2.3. By means of the Kerr effect, quantum logic operations such as the controlled phase gate [94], the quantum Fredkin gate [95] and the conditional phase switch [96] can be realized.

We stress that the Kerr effect demonstrated in Chapter 4.2.3 is purely due to the coherent interaction between the fields and the transmon. This differs greatly from what has previously been demonstrated in superconducting devices where

the utilization of the kinetic inductance of a superconducting film [97] or the Josephson inductance of a Superconducting Quantum Interference Device (SQUID) [38] required a pump tone at least several orders of magnitude higher than those used in this experiment.

### 2.4.3 Photon Detection with Cross-Kerr Scheme

It has been suggested that quantum-nondemolition detection of propagating photons may be possible by measuring the Kerr phase shift [98]. In this section, we investigate the possibility to detect free microwave photons with the giant cross-Kerr phase shift. The detailed theoretical derivation is done by Bixuan Fan *et al.* in appended paper VI. We illustrate the main result of that paper here. The idea is to use a three-level transmon to detect a single-photon Fock state traveling through an open transmission line, as shown in Fig. 2.20(a). Assuming the photon close to resonance with the 1-0 transition of the transmon, we do the measurement by sending a coherent probe signal with amplitude  $\alpha$  at a frequency close to the 1-2 transition of the transmon, as shown in Fig. 2.20(b). The coherent probe field is characterized by its amplitude and phase. If the transmon is in the ground state, the probe does not interact with the 1-2 transition of the transmon. However, if a (control) photon interacts with the 0-1 transition of the transmon, this will change what the probe experiences when passing the transmon. The probe will acquire a phase shift, which can be detected using heterodyne detection (see Fig. 2.20(c)). Heterodyne detection basically measures the two quadratures of the probe field.

Can we distinguish a single photon in this scheme? To answer this question, we simulate the numerical SNR from the stochastic, cascaded master equation method having initial condition with or without incoming photon. The results are shown in Fig. 2.21. The inset shows the histogram on the Q displacement of the probe. Even in an ideal setup there is vacuum noise, which gives the widths of the peaks. We see that the blue and green area mostly overlap with each other, meaning that the two possibilities of one and zero photons are impossible to distinguish. We can define a signal-to-noise ratio (SNR), which is related to the ratio of the distance between the center of the peaks and the width of the peaks [92]. To have a good photon detector, we should have a SNR above unity. We tried optimizing different parameters, but the SNR can never exceed unity for a single atom. In the main panel of Fig. 2.21, we show that the optimized SNR as a function of normalized probe amplitude  $\alpha/\gamma_{10}$ . We show that in spite of the very large cross-Kerr nonlinearity, the induced probe displacement in the presence of a single control photon is limited by saturation effects in the transmon, and is always less than its own quantum noise. This approach seems to be fundamentally limited by the time needed for the photon to interact with the transmon, the limited signal which can be produced in this time and the unavoidable quantum noise. How-

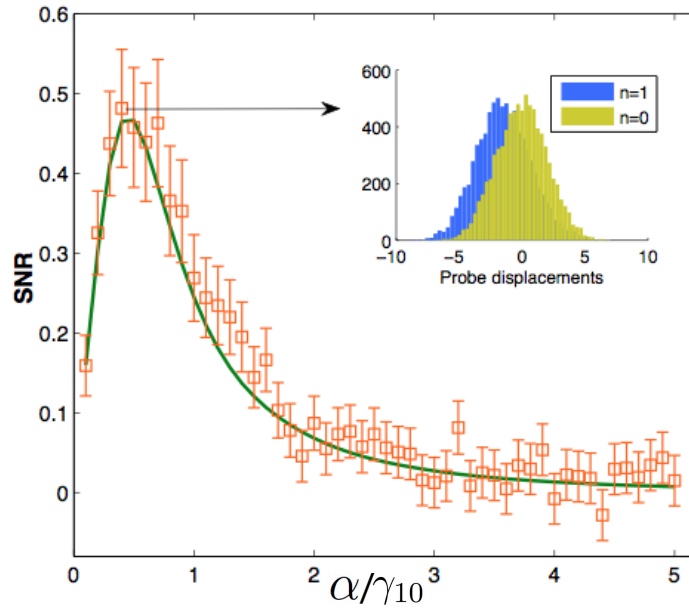


Figure 2.21: The SNR as a function of the normalized probe amplitude  $\alpha/\gamma_{10}$  at optimal parameter settings. Note that the normalized probe amplitude  $\alpha$  is in the unit of  $\gamma_{10}$ , instead of  $\gamma_{21}$ . We assume no pure dephasing, therefore  $\gamma_{10} = \gamma_{21}/2$ . The orange squares represent the numerical SNR from the stochastic, cascaded master equation method and the green curve represents the analytic SNR from the Fock state master equation method and quantum regression theorem. The inset provides the histogram of the highest SNR for zero and one control photon. Figures borrowed from appended paper VI.

ever, more recently, by building a chain of artificial atoms (Fig. 2.16B) connected through circulators which break time-reversal symmetry, making both photon and probe propagate in one direction, Ref. [99] shows that a SNR above one can be realized.

## 2.5 Second-Order Correlation

In this section, we want to address the following question. What is the photon statistics of the reflected or transmitted field from a two-level atom with a resonant coherent drive? In order to answer this question, we investigate the second-order correlation of the fields. Historically, Hanbury Brown and Twiss [100] first measured intensity-intensity correlations between two beams in 1956. As we will show later, the second-order correlation function,  $g^{(2)}$ , is directly related to the

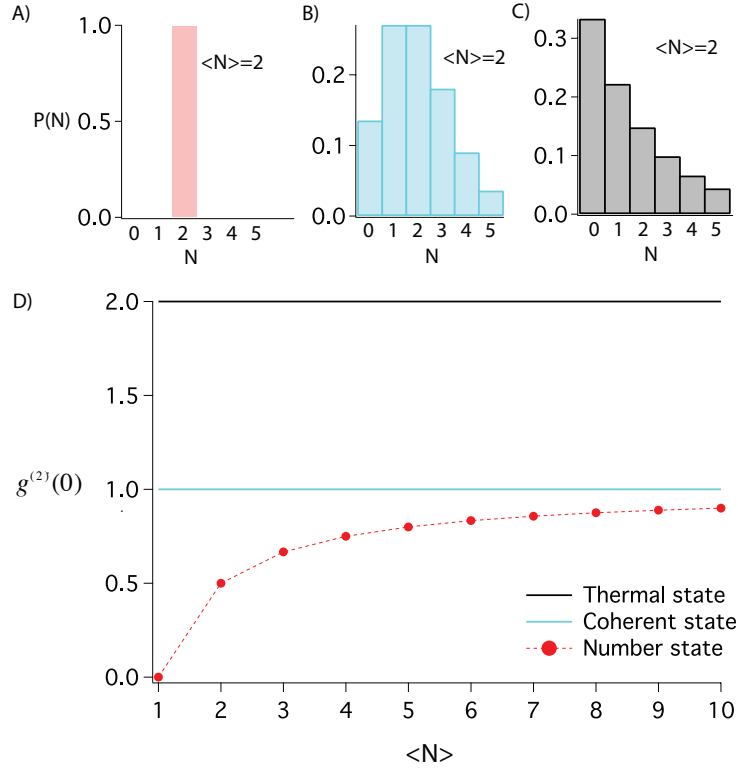


Figure 2.22: Comparison of the photon distribution and corresponding  $g^{(2)}(0)$  of various light states. A) Number state  $|2\rangle$ . B) Coherent light: poisson distribution (Eq. 2.107) with  $\langle N \rangle = 2$ . C) Thermal light: Bose-Einstein distribution (Eq. 2.109) with  $\langle N \rangle = 2$ . D)  $g^{(2)}(0)$  as a function of  $\langle N \rangle$  for the number state (Eq. 2.101), coherent state (Eq. 2.106) and thermal state (Eq. 2.111).

intensity-intensity correlations. Measuring  $g^{(2)}$ , we can reveal the quantum properties of the field. First, we will give a basic comparison between different light sources in terms of their photon statistics and the second-order correlation function. Then, we will compare the typical methods to measure  $g^{(2)}$  in optics and in microwaves. With this method, we are able to measure  $g^{(2)}$  of the state generated by a two-level atom in a 1D open transmission line.

### 2.5.1 Photon Statistics of Different Light Sources

For single-mode light, the second-order correlation function is defined as

$$g^{(2)}(\tau) = \frac{\langle a^\dagger(t')a^\dagger(t'+\tau)a(t'+\tau)a(t') \rangle}{\langle a^\dagger(t')a(t') \rangle \langle a^\dagger(t'+\tau)a(t'+\tau) \rangle}, \quad (2.98)$$

which is interpreted as the conditional probability that if a photon is detected at time  $t'$  one is also detected at  $t' + \tau$ .  $a^\dagger$  and  $a$  are the creation and annihilation operators of the field,  $\tau$  is the delay time between the two paths (see Fig. 2.24). At zero delay time, this can be further expressed in the following way,

$$g^{(2)}(\tau = 0) = \frac{\langle N(N-1) \rangle}{\langle N \rangle^2} = 1 + \frac{(\Delta N)^2 - \langle N \rangle}{\langle N \rangle^2}, \quad (2.99)$$

where  $N = a^\dagger a$  is the number operator. The photon-number variance,  $(\Delta N)^2$ , must be a non-negative quantity,

$$(\Delta N)^2 = \langle N^2 \rangle - \langle N \rangle^2 \geq 0. \quad (2.100)$$

Three prototypical light states are the number state (Fock state), coherent state and thermal state. We summarize the following comparisons for different states in Fig. 2.22 and Fig. 2.23.

#### A) Number state $|N\rangle$ :

For a number state  $|N\rangle$ , the photon number is well defined, therefore,  $(\Delta N)^2 = 0$ . Eq. (2.99) then gives

$$g^{(2)}(0) = 1 - 1/\langle N \rangle. \quad (2.101)$$

In particular, for the number state  $|1\rangle$ , we have

$$g^{(2)}(0) = 0. \quad (2.102)$$

Therefore, the joint probability for detecting photon at the same time is zero.

#### B) Coherent state $|\alpha\rangle$ :

From the properties of the coherent state, we know that [102],

$$a|\alpha\rangle = \alpha|\alpha\rangle; \langle\alpha|a^\dagger = \langle\alpha|\alpha^*,$$

from which, we can derive the following expressions,

$$\langle N \rangle = \langle\alpha|a^\dagger a|\alpha\rangle = |\alpha|^2; \quad (2.103)$$

$$\langle N^2 \rangle = |\alpha|^4 + |\alpha|^2 = \langle N \rangle^2 + \langle N \rangle. \quad (2.104)$$

From Eq. (2.103) and Eq. (2.104), we have

$$(\Delta N)^2 = \langle N^2 \rangle - \langle N \rangle^2 = \langle N \rangle. \quad (2.105)$$

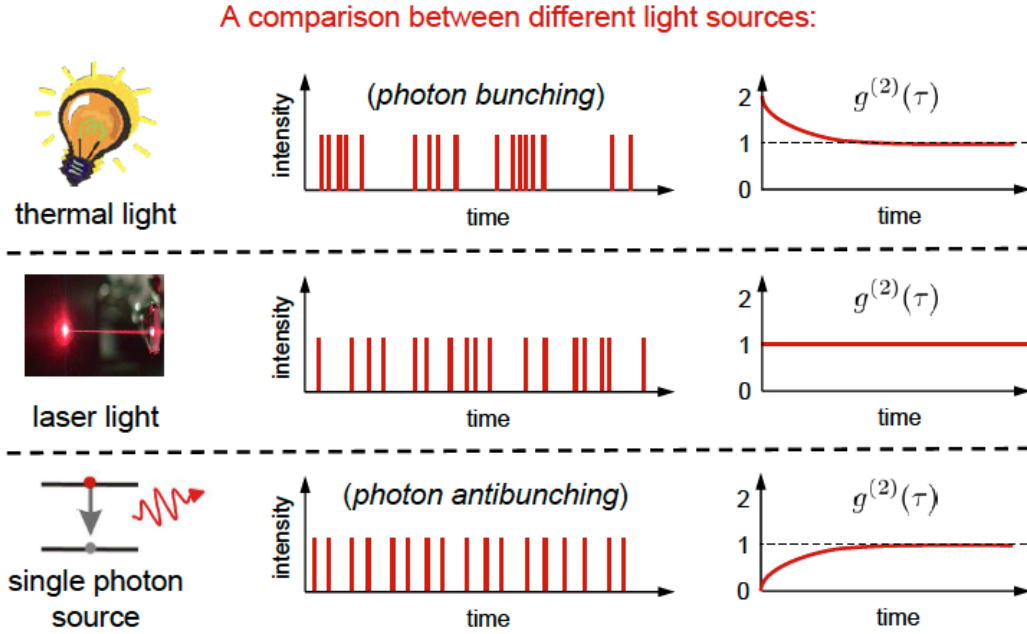


Figure 2.23: Comparison of the photon statistics of various light states. A) Thermal/chaotic light with  $g^{(2)}(0) = 2$ , showing bunching statistics. B) Coherent light with  $g^{(2)}(\tau) = 1$ , showing poissonian statistics. C) Number state  $|1\rangle$  with  $g^{(2)}(0) = 0$ , showing antibunching statistics. For  $\tau \rightarrow \infty$ ,  $g^{(2)} = 1$  in all light sources. Figure borrowed from [101].

Substituting Eq. (2.105) into Eq. (2.99) gives

$$g^{(2)}(0) = 1, \quad (2.106)$$

which is independent on  $\langle N \rangle$ . We know that the photon-number distribution of a coherent state is the Poisson distribution [102],

$$P(N) = \frac{\langle N \rangle^N}{N!} e^{-\langle N \rangle}. \quad (2.107)$$

### C) Thermal state $|\beta_T\rangle$ :

From the properties of the thermal state, the average number of photon  $\langle N \rangle$  is [102],

$$\langle N \rangle = \frac{1}{e^{\hbar\omega/k_B\Theta} - 1}, \quad (2.108)$$

where  $\Theta$  is the temperature. The photon-number distribution can be expressed as [102],

$$P(N) = \frac{\langle N \rangle^N}{(1 + \langle N \rangle)^{1+N}}. \quad (2.109)$$

Eq. (2.108) and Eq. (2.109) lead to the following expression [102],

$$(\Delta N)^2 = \langle N \rangle^2 + \langle N \rangle. \quad (2.110)$$

Substituting Eq. (2.110) into Eq. (2.99) gives

$$g^{(2)}(0) = 2, \quad (2.111)$$

which is independent of  $\langle N \rangle$ .

In optics,  $g^{(2)}(\tau)$  is measured using the Hanbury-Brown Twiss setup, as discussed below. In Fig. 2.24A, we consider a single-photon source, which emits single photons. Naively, since the photon is particle like, it can either go via path 1 or path 2 when it encounters a beam splitter. Therefore, the joint probability for both detecting the photon at detector 1 and detector 2 is zero, *i.e.*  $g^{(2)}(0) = 0$ . However, in the microwave regime, single-photon detectors are not available. With advanced microwave techniques, the second-order correlation function can be measured using linear amplifiers [103] (see appendix D for details). Fig. 2.24 compares the Hanbury-Brown Twiss measurements in the optical and the microwave domains. The measurement of  $g^{(2)}(\tau)$  for microwave photons is challenging for two reasons. First, the photon energy is five orders of magnitude less than that of optical photons (see Fig. 1.2A). Second, the low-noise microwave amplifier has about 30 thermal photons of noise, which will be characterized in Chapter 3.3.1. Nevertheless, we are able to measure  $g^{(2)}(\tau)$  for propagating microwave photons in Chapter 4.2.2 by making many averages. The key issue is that the noises of two amplifiers are uncorrelated. Other groups also observed the antibunching behavior of microwave photons in a cavity [103].

## 2.5.2 Antibunched and Superbunched States

In the Section 4.2.2, we demonstrate the quantum nature of the scattered field generated from our two-level artificial atom in a 1D open transmission line by using a resonant coherent state. In particular, by measuring the  $g^{(2)}(\tau)$  of the fields we show that the reflected field is antibunched [49, 102] while still maintaining first-order coherence. Moreover, we observe superbunching statistics in the transmitted fields [49].

To understand how our artificial atom generates antibunched and superbunched states, it is helpful to consider the incident coherent state in the photon number basis. For a low power incident field with less than 0.5 average photons per lifetime

---

of our atom, we can safely approximate the coherent field using only the first three photon eigenstates. If we consider a one-photon incident state, the atom reflects it, leading to antibunching statistics in the reflected field. Together with the zero-photon state the reflected field still maintains first-order coherence. For a two-photon incident state, since the atom is not able to scatter more than one photon at a time, the pair has a much higher probability of transmission, leading to superbunching statistics in the transmission [49, 104]. Superbunching statistics refers to  $g^{(2)}(0) > 2$ . In summary, the two-level atom acts as a photon-number filter, extracting the one-photon from the incident coherent state. We demonstrate this effect in Chapter 4.2.2. The detailed theoretical derivation is studied by B. Peropadre *et al.* [83] in the append paper V.

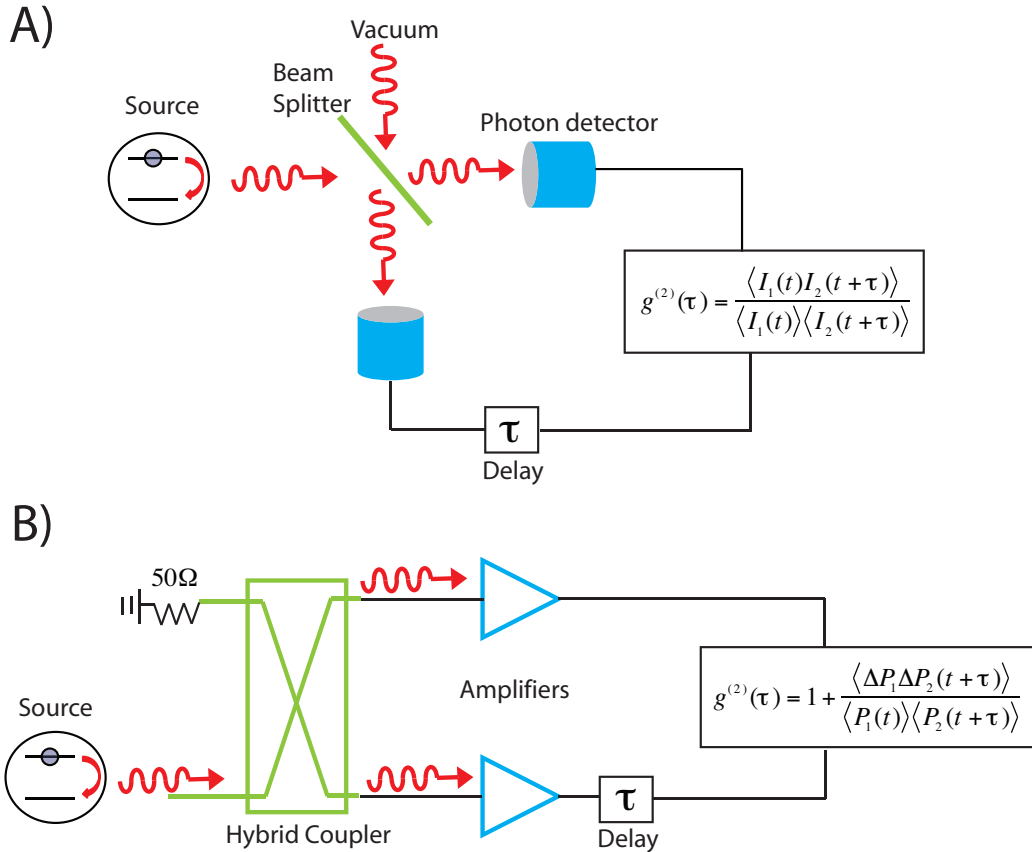


Figure 2.24: Hanbury-Brown Twiss setup. A) Optical version using photon detectors. A single-photon source emits one photon at a time. The photon (red) goes through a beam splitter (green) and is then detected by the photon detector (blue).  $\tau$  is the delay time between the two paths. We can then compute  $g^{(2)}(\tau)$ , from correlations between intensity  $I_1$  and  $I_2$ . B) Microwave version using linear amplifiers with the corresponding color code. The beam splitter is a hybrid-coupler. The 50 ohm port acts as a vacuum port, provided that  $k_B T \ll \hbar\omega$ .  $P_1$  and  $P_2$  refer to the power of the fields after the amplifier (blue).  $\langle \Delta P_1 \Delta P_2 \rangle$  is the covariance of the output powers in ports 1 and 2, defined as  $\langle (P_1 - \langle P_1 \rangle)(P_2 - \langle P_2 \rangle) \rangle$ . See appendix D for details.

# Chapter 3

## Experimental Techniques

The type of samples proposed in Fig. 1.4B and Fig. 2.16B have been designed, fabricated and measured. They were made from Al on a silicon substrate at the Nanofabrication Laboratory at Chalmers University of Technology. Micrographs of the fabricated samples are shown in Fig. 3.2. They were cooled to low temperature ( $\leq 50$  mK) to initialize the artificial atoms in their ground states and then measured with coherent microwave photons at powers ranging from -140 dBm to -100 dBm. Due to the bandwidth of the low noise amplifier (LNA), we measure the response of the artificial atom at frequencies ranging from 4 GHz to 8 GHz. This chapter describes the full experimental procedure, including design, fabrication and measurements.

### 3.1 Sample Design

When designing the circuits, we have the following considerations. Firstly, the characteristic impedance of the CPW,  $Z_0$ , depends on the width and the gap of the CPW, and on the dielectric constant of the substrate. To match the circuit to standard microwave devices, we choose  $Z_0 \simeq 50 \Omega$ . We use “txline”, a microwave simulation package, to determine the gap and width of the CPW. The gap and the width of the center transmission line were designed to be  $10 \mu\text{m}$  and  $16.7 \mu\text{m}$ , respectively in the measured devices. Secondly, in order to stay in the transmon regime and still have enough anharmonicity between the first 3 levels, we are restricted to the ratio  $E_J/E_C$  to the range 20-50. The atomic transition frequency should also be within 4-8 GHz, in the range of the LNA (see Fig. 3.3D). For a given material, we know that the product of the normal resistance of the junction  $R_n$  and the Josephson energy  $E_J$  is a constant [16], therefore we choose  $R_n \sim 10 \text{ k}\Omega$ , which gives  $E_J \simeq 14 \text{ GHz}$ . Thirdly, in order to have high reflection  $r$  from the atom, from Eq. (2.59) and Eq. (2.80), the relaxation (coupling) rate should

be much larger than the pure dephasing rate, *i.e.*,  $\Gamma_{10} \gg \Gamma_{\phi,10}$  (strong coupling limit). In addition, this increases the saturation power  $P_r \sim \hbar\omega_{10}\Gamma_{10}$  of the single atom, making it easier to observe. However,  $\Gamma_{10}$  should be less than the frequency anharmonicity between the  $\omega_{10}$  and  $\omega_{21}$  transitions, *i.e.*  $\Gamma_{10} < \omega_{10} - \omega_{21}$ , so that the levels can be addressed individually.

Design parameter	Value
$\omega_{10}$	5.7 GHz
$\omega_{21}$	5.38 GHz
$\Gamma_{10}$	55 MHz
$E_J/\hbar$	14 GHz
$E_C/\hbar$	320 MHz
$E_J/E_C$	44
$\beta$	0.4
Gap of CPW	10 $\mu\text{m}$
Width of CPW	16.7 $\mu\text{m}$
$Z_0$	50 $\Omega$

Table 3.1: Summary of the design parameters for Sample 1a.

From Eq. (2.29), the anharmonicity,  $\alpha_n$ , is equal to  $E_C/\hbar$  for a transmon, and thus determined by the total capacitance  $C_\Sigma$ . Considering  $\omega_{10}$  fixed, the only way to increase  $\Gamma_{10}$  is to engineer the coupling to the CPW,  $\beta = C_c/C_\Sigma$ , according to Eq. (2.58). We can see that strong coupling is achieved by a high  $\beta$ . This is done by having a small gap between the transmon and the center conductor, and a small gap between the transmon and the ground plane. We designed it to be  $\sim 0.5 \mu\text{m}$  in both cases (See Fig. 3.2A,B,C). By putting the fingers of the interdigitated capacitor far apart ( $\sim 3 \mu\text{m}$ ), the total capacitance comes mostly from the coupling capacitor  $C_c$ , instead of the interdigitated capacitor, resulting in a larger  $\beta$ . This design with  $\beta \sim 0.7$  is different from the typical transmon design [20, 31, 40, 68] where  $\beta = 0.1 \sim 0.2$ .

All the capacitances were then simulated using Microwave Office. For a given geometric design and  $R_n$ , we can get an estimate of  $\Gamma_{10}$  from Eq. (2.54). The design parameters for Sample 1a (Fig. 3.2A) are shown in table 3.1. For the design of sample 1a (Fig. 3.2A), we expected to see  $\Gamma_{10} \sim 55 \text{ MHz}$  and  $\beta \sim 0.4$  according to the simulation. From the experiment results in Chapter 4, we get  $\Gamma_{10} \simeq 73 \text{ MHz}$  and  $\beta \sim 0.7$ . Note that there are uncertainties in the design estimate, such as  $R_n$ , which is only measured in a test structure (see the blue square in Fig. 3.3B). We also estimate the individual capacitances from a combination of different electrodes using Microwave Office, then we use the equivalent circuit

model of the transmon in Fig. 2.11 to calculate  $\Gamma_{10}$  and  $\beta$ . Since this is a CPW structure, a simple parallel and series capacitor model does not work well.

The size of the transmon in Sample 1a and Sample 1b are  $160 \mu\text{m} \times 36 \mu\text{m}$  and  $320 \mu\text{m} \times 36 \mu\text{m}$ , respectively (see Fig. 3.2A and B). The size of the electrodes are bigger in Sample 1b, giving a higher  $C_\Sigma$ . This leads to a higher  $E_J/E_C$  ratio for the same  $E_J$ . As I will demonstrate experimentally in the next chapter, with high  $E_J/E_C$ , the pure dephasing rate is much less due to the first excited level being insensitive to charge noise [66]. According to Eq. (2.59) and Eq. (2.80), the transmon then reflects resonant photons more efficiently. The transmon design of Sample 2 is the same as Sample 1b. In Sample 2, we introduce a boundary condition for the transmon, as discussed theoretically in Chapter 2.3.4.

## 3.2 Fabrication

Our samples are fabricated on a 3-inch silicon wafer with a few nm of SiOx. This intrinsic silicon wafer should be a good insulator with a low loss tangent, so that it would not affect the performance of the device. The major fabrication steps are explained as follows. A full recipe is given in Appendix E. More details of our fabrication technique can be found in [106, 107]. We pattern the gold pad (large structures) and the Al (small structures) by using photolithography and e-beam lithography, respectively. In Fig. 3.3B, the yellow part is the gold pad, while the white part is Al.

### Photolithography

This step patterns the large area of the ground plane. The wafer is covered by a thin layer of a photo sensitive polymer, called photoresist. By applying ultraviolet light to the polymer, the internal bonds of the polymer are broken (for positive resist). Therefore, the exposed polymer is more dissolvable in a specific solvent (developer) than the unexposed polymer.

In our case, two layers of resist were used. The bottom and top resists are the lift-off layer and the imaging layer, respectively. The exposed wafer is developed in a developer to remove the exposed top resist and create an undercut profile in the bottom layer (see step 2 in Fig. 3.1). Although Fig. 3.1 shows the schematic of e-beam lithography, the principle of photolithography and e-beam lithography are similar.

### E-beam lithography

This step patterns the small structures including part of the ground plane, the CPW and the transmon. Photolithography uses photosensitive polymer, whereas

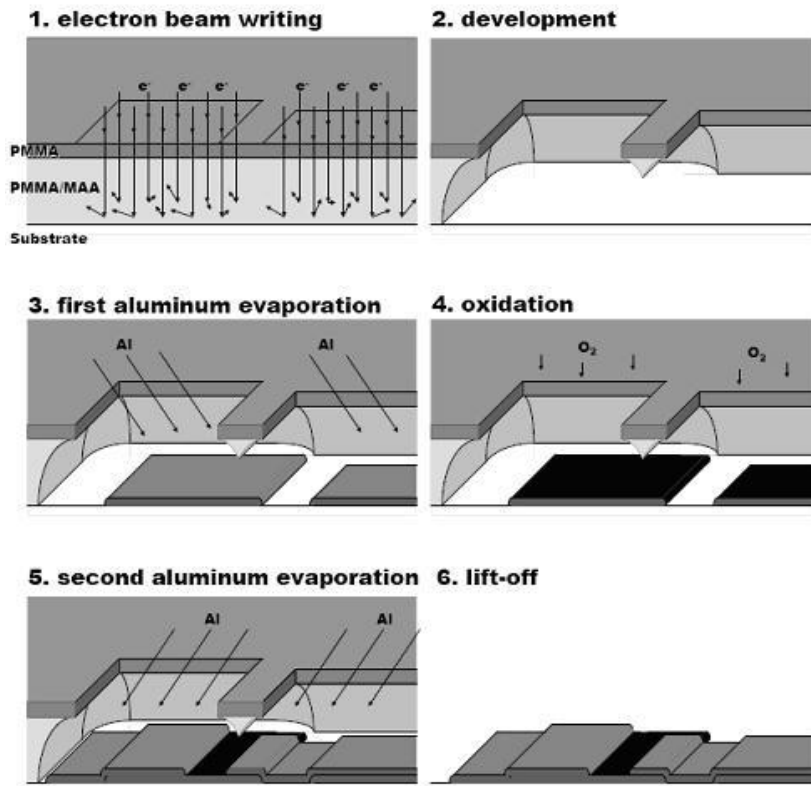


Figure 3.1: Schematic of E-beam lithography and the shadow evaporation technique for making a Josephson junction. The figure here is borrowed from [105]. This involves 6 major steps: 1) An electron beam is used to write the designed pattern into the two-layer resist. 2) Development of the top and bottom resist leads to the formation of suspended bridges. 3) Evaporation of Al at positive angle ( $30^\circ$ ). 4) Oxidation of Al. 5) Evaporation of Al at negative angle ( $-30^\circ$ ). 6) Lifting off the resists.

the e-beam lithography uses electron-sensitive polymer. The wavelength of the electrons can be made much smaller than optical wavelengths. This makes it possible to pattern very small features ( $\sim 10$  nanometers). Depending on the size of the structure, we use three different beam currents to write the ground plane, the CPW and the transmon. See Fig. 3.1 for a description of e-beam lithography of a Josephson junction.

### Double angle evaporation of Al

The Josephson junctions are formed by double angle evaporation of Al, step 3 to 6 in Fig. 3.1. We deposit a 20 nm thick aluminum layer with an angle of  $30^\circ$  (step

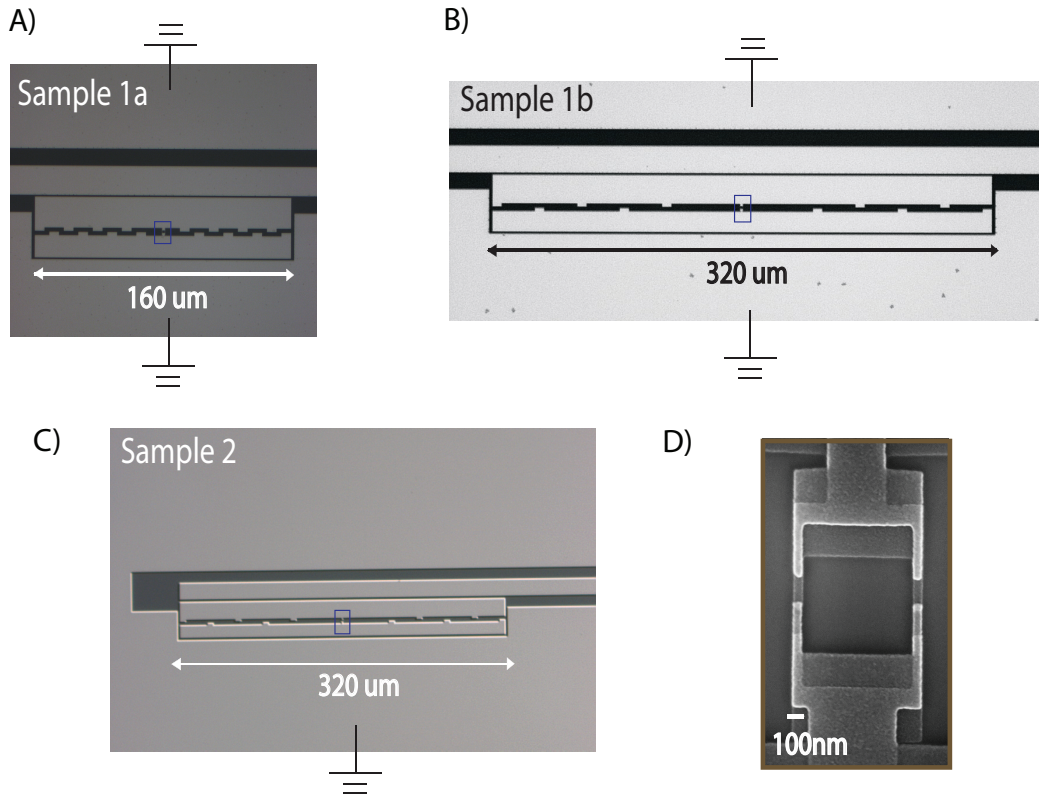


Figure 3.2: Microscopy pictures of the fabricated samples. The light regions are Al while the dark regions are the oxidized silicon substrate. In A) and B), we see the center conductor of the CPW in between the two ground planes and the two plates of the interdigitated capacitance of the transmon. A) Sample 1a: a transmon in a 1D open transmission line. B) Sample 1b: a transmon in a 1D open transmission line, with a higher total capacitor  $C_{\Sigma}$ . This leads to a lower  $E_C$ . The quantum circuit model of Sample 1a,b corresponds to Fig. 2.12A. C) Sample 2: a transmon at end of a 1D transmission line. The quantum circuit model of Sample 2 corresponds to Fig. 2.16C. D) Scanning-electron micrograph of the SQUID loop of the transmon in A), which allows us to tune its transition frequency with an external magnetic flux  $\Phi$ . The box in A), B) and C). indicate the position of the SQUID.

3 in Fig 3.1) on the chip. Then, oxygen is let into the vacuum chamber. A few nm aluminum oxide grows on top of the aluminum. Then, we evaporate another 40 nm of Al on the aluminum oxide at an angle of  $-30^\circ$  (step 5 in Fig. 3.1). The Josephson junctions are formed in the overlap area (see Fig. 3.2D).

## 3.3 Measurement Setup

### 3.3.1 Microwaves

The sample is wire bonded to a microwave PCB (Printed Circuit Board) designed with CPWs and mounted in a sample box, see Fig. 3.3A. The PCB has small vias all over the ground planes, which help to eliminate resonant modes in the ground plane. The cryostat is equipped with semirigid coaxial cables with a characteristic impedance of  $50 \Omega$ . From room temperature (RT) to the still stage, the cables are stainless steel cables (UT-85-SS), since stainless steel has low heat conduction. From the still stage to the mixing chamber stage, both Nb and NbTi cables are used. When they are superconducting ( $< 10$  K), they have a very low thermal conductivity but a high electrical conductivity. On each stage, the outer conductor of the cables are thermally anchored using panel mounted bulk head feed throughs.

The setup for the single-photon router and the second-order correlation measurements are shown in Fig. 3.4A and B, respectively. Attenuators (solid red box) at each stage have two functions. Firstly, since the lowest microwave drive at the sample is around  $-140$  dBm, the input signal needs to be attenuated. This also reduces the thermal noise from each stage. For example, there is in total  $60$  dB of attenuation from room temperature ( $300$  K) to the sample stage at the mixing chamber. Similarly,  $40$  dB and  $30$  dB of attenuation from  $4.2$  K and  $1.5$  K stage to the sample stage, respectively. Therefore, the noise temperature  $T_N = 300/10^6 + 4.2/10^4 + 1.5/10^3 = 2.22$  mK is added to the sample. We characterize the total noise temperature of the detection chain in next section. Secondly, the attenuators heat sink the inner conductor of the coaxial cables.

The circulators allow microwaves to travel in only one direction, typically with  $20$  dB isolation. By putting two in series, we are able to increase the isolation. By using circulators, labeled 1-4 in Fig. 3.4, we can measure the reflected signal from the atom, which travels to the amplifier. Because room temperature thermal noise and the  $4$  K thermal noise can enter the output line, it is crucial to have high isolation, *i.e.*, more circulators. The DC block before the LNA is intended to prevent heat conduction from the LNA to the lower stages via the coax. As mentioned before, the reflected photon power  $P_r = \hbar\omega_{10}\Gamma_{10} \sim 10^{-16}$  W from the atom is very weak. In order to measure this faint signal, many stages of amplification are employed. The first stage amplification is a LNA (blue triangle in Fig. 3.4) with  $36$  dB gain. The second stage amplifier has a gain of  $30$  dB at room temperature.

A small superconducting magnet, attached to the sample box, is used to flux bias the atom (Fig. 3.3C).

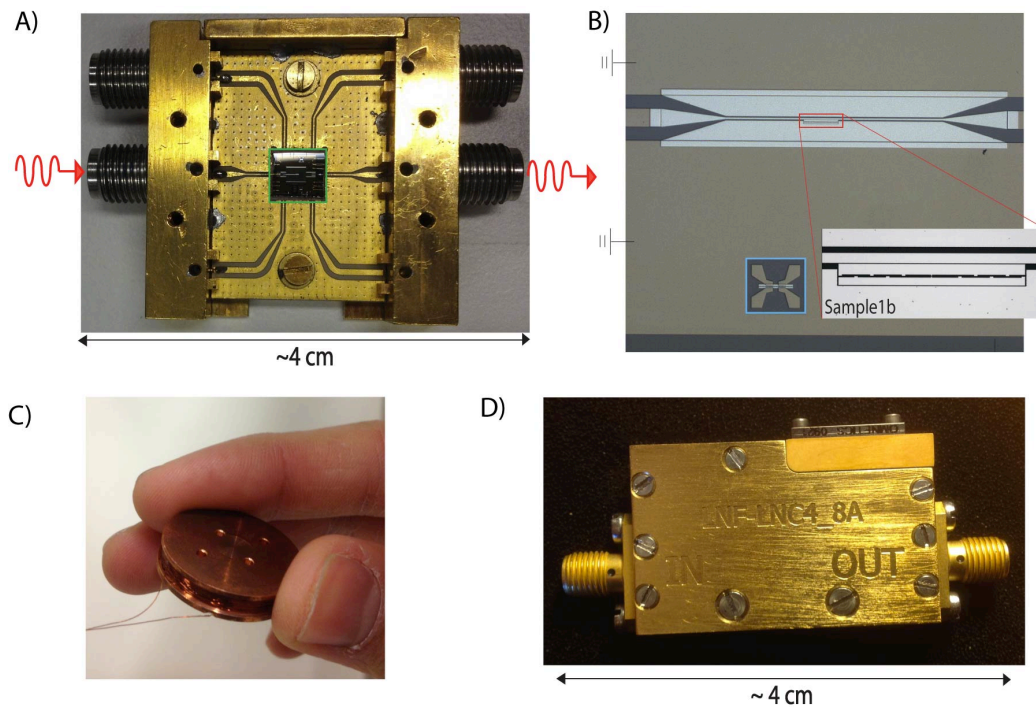


Figure 3.3: A)  $5\text{ mm} \times 5\text{ mm}$  Chip (green square) is wire bond to a printed circuits board and mounted in a sample box. The PCB has four CPWs connected to high frequency SMK launchers. Only two of them are being used, indicated by the propagating fields (red) along the SMA connectors. B) Micrograph picture of Sample 1b. The grey ground plane is the gold pad, while the white part is Al. The blue box indicates the test transmon, which is identical to the transmon in the transmission line. By measuring the normal resistance  $R_n$  of this transmon, we can get an estimation for  $E_J$ . C) The superconducting magnet is attached to the sample box. It is used to create a magnetic flux,  $\Phi$ , through the SQUID loop of the transmon. D) The LNA is a key component for measurement of microwave photons, as discussed in Fig. 1.2B and Fig. 2.24B. The quantum mechanical description of a linear amplifier is discussed by C.M. Caves [108].

### Noise temperature measurement

It is important to know the noise temperature of the system since the noise dramatically affects the averaging time of the data. In this section, we characterize the total noise temperature of the detection chain in the following way. We use a signal generator to send a continuous wave at 5 GHz, then measure the output spectrum with the signal on and off. The table below summarizes the results. The noise temperature ( $T_N$ ) is calculated according to the following equation:

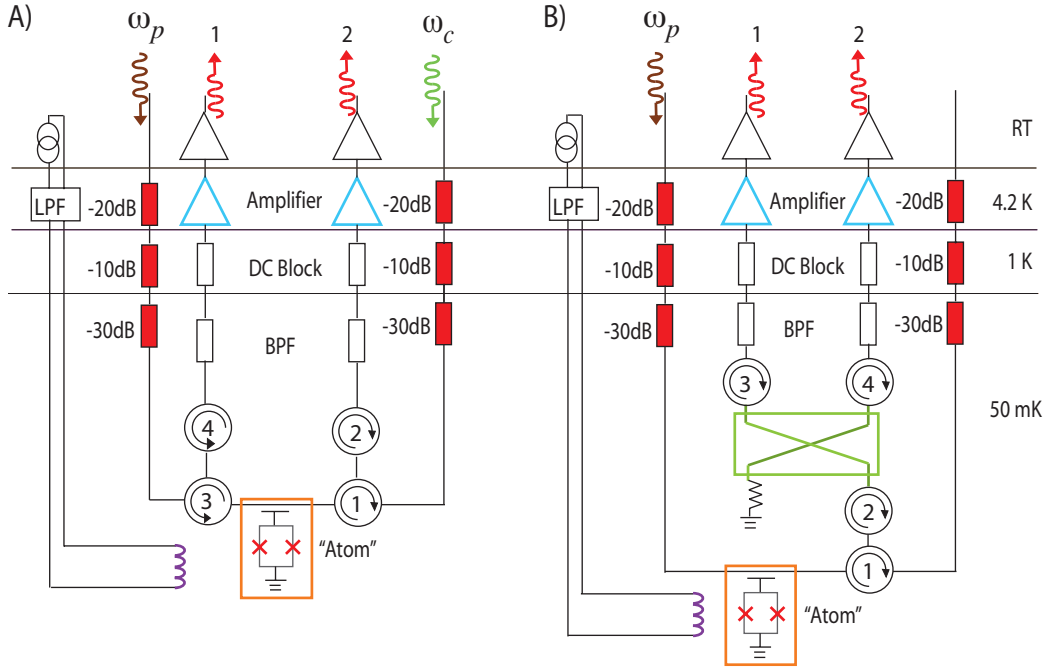


Figure 3.4: Measurement setup for an artificial atom in a 1D open transmission line. The blue triangles represent the LNA (see Fig. 3.3D). The orange square represents the sample box (see Fig. 3.3A). The purple curves represent the superconducting magnet (see Fig. 3.3C). The red squares represent attenuators. The green box represents a hybrid-coupler, acting as a beam splitter (see Fig. 2.24). A) Setup for measurement of the single-atom scattering in Chapter 4.1.1 and the single-photon router in Chapter 4.2.1. A strong control pulse at  $\omega_c = \omega_{21}$  is used to route a weak microwave signal at the probe frequency  $\omega_{10}$ . The circulators, numbered 1-4, allow us to separate signals propagating in different directions in the lines. We also use this setup for measurement of the cross-Kerr effect in Chapter 4.2.3. B) Schematic setup for measurement of the second-order correlation function in Chapter 4.2.2. This setup enables us to do Hanbury Brown-Twiss measurements between output ports 1 and 2. Depending on the choice of input port, we can measure  $g^{(2)}$  of the reflected or transmitted field.

$$k_B \cdot T_N \cdot RBW = P_N, \quad (3.1)$$

where

$$P_N = 10^{-3} \cdot 10^{+(N_f - G)/10}. \quad (3.2)$$

$P_N$  is the noise power in units of Watts.  $N_f$  and  $G$  are the noise factor at the analyzer and the gain, respectively, in units of dB. RBW is the Resolution Bandwidth.

Note that the noise temperature of the system was primary characterized by a shot noise thermometer [109]. The method in this section is a secondary way to check things have not gotten worse.

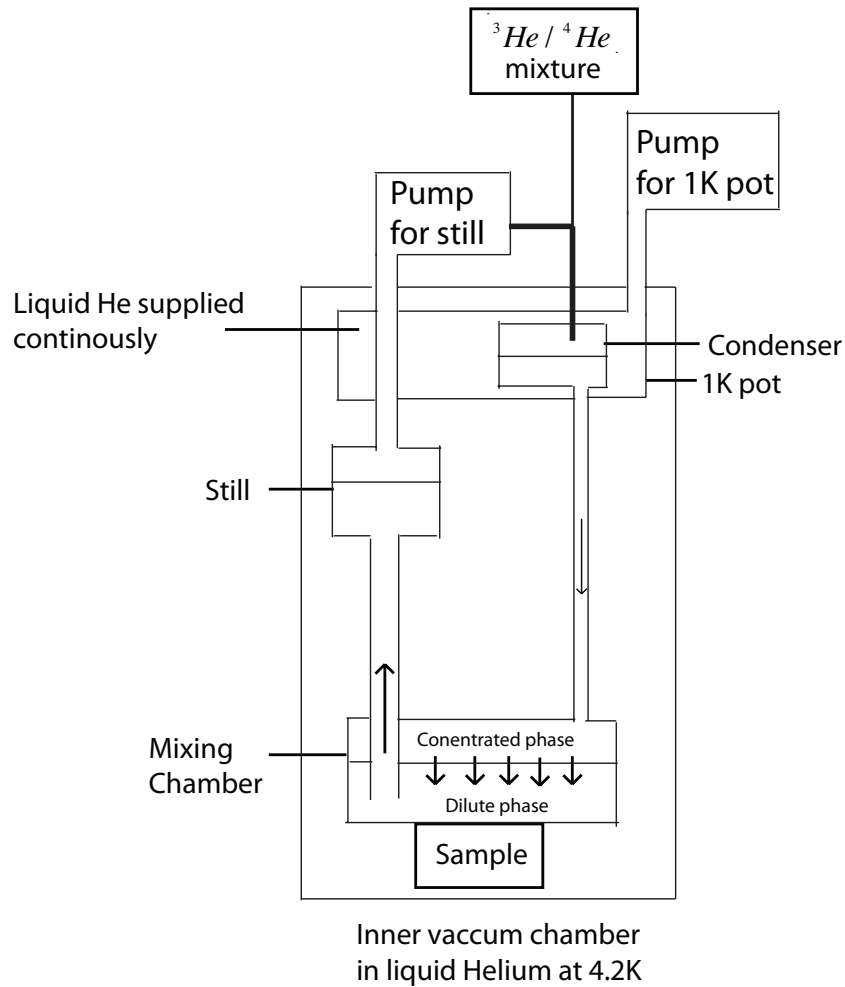
Description	data
RBW	2000 Hz
Total attenuation before the atom	123 dB
Applied signal	-15 dBm
Output signal	-68.04 dBm
Noise floor ( $N_f$ )	-89.4 dBm
Gain (G)	$-68.04 - (-15 - 123) = 69.96$ dB
Noise temperature ( $T_N$ )	6.4 K

Table 3.2: Experiment data for calculating the noise temperature of the system @5 GHz

### 3.3.2 Cryogenics

The basic concept of a cryogenic dilution fridge is shown in Fig. 3.5. The sample was placed inside a vacuum chamber, called the inner vacuum chamber (IVC), which is submerged in a liquid  $^4\text{He}$  bath at atmospheric pressure. Inside the IVC, there are several temperature stages.  $^4\text{He}$  is drawn from the bath into the 1 K pot and is pumped to around 1.5 K. This stage, called the 1 K pot stage, is then used to condensed the  $^4\text{He}/^3\text{He}$  mixture in a closed system. The next stage is the still with a temperature of about 600 mK. After the still stage, there is a continuous heat exchanger and a cold plate stage with a temperature around 100 mK. The final stage is the mixing chamber, where the phase separation occurs.  $^3\text{He}$  gas is pumped out of the dilute phase of the liquid  $^4\text{He}/^3\text{He}$  mixture. The base temperature is around 20-50 mK. The sample is mounted at this stage.

The thermal contact of the sample and the mixing chamber should be good to ensure the sample cools down to the base temperature. Moreover, heat sinking of the wires at each stage is very important, since heat may be directly conducted down to the sample through the wires.



*Figure 3.5: Simplified schematic diagram of a dilution refrigerator. Note that the  ${}^4\text{He}/{}^3\text{He}$  mixture is circulated in a closed system. In the mixing chamber two phases of  ${}^4\text{He}/{}^3\text{He}$  mixtures are in equilibrium: the so-called concentrated phase and the dilute phase. The  ${}^3\text{He}$  flows from the concentrated phase through the phase boundary into the dilute phase and cools down the cryostat.*

# Chapter 4

## Experimental Results

We summarize the main results of the thesis in this chapter. In the first section, we will demonstrate well-known quantum-optical effects such as single-atom scattering, the Mollow Triplet and the Autler-Townes splitting. In the second section, we will demonstrate three quantum applications based on these effects, where single microwave photons are manipulated and allowed to interact using transmon qubits: a single-photon router, a photon-number filter and the cross-Kerr phase shift.

The experimental results come from the measurements of the samples shown in Fig. 3.2A,B,C. The detailed measurement setups are shown in Fig. 3.4. The theoretical fits and calculations are based on Chapter 2 and Appendix B,C,D and F.

### 4.1 Quantum Optics with Propagating Microwaves

#### 4.1.1 Single-Atom Scattering

According to Eq. (2.29), the 0-1 transition energy of the transmon is

$$\hbar\omega_{10}(\Phi) \approx \sqrt{8E_J(\Phi)E_C} - E_C, \quad (4.1)$$

where  $E_C = e^2/2C_\Sigma$  is the charging energy,  $C_\Sigma$  is the total capacitance of the transmon and  $E_J(\Phi)$  is the Josephson energy which can be tuned by the external flux  $\Phi$ , according to Eq. (1.14). In this section, we investigate the scattering properties of the 0-1 transition of a transmon with an incident coherent state, in two configurations as proposed in Chapter 2.3.2 and Chapter 2.3.4. We also compare the elastically (coherent) and inelastically (incoherent) scattered fields from the transmon.

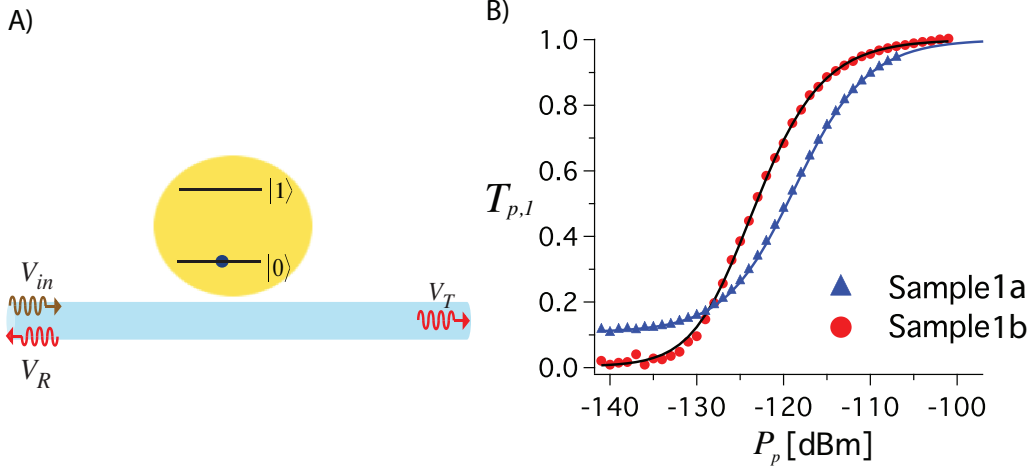


Figure 4.1: (A) Cartoon of scattering of a resonant coherent state from a two-level atom in a 1D open waveguide. (B) Measured transmittance,  $T_{p,1} = |t_{p,1}|^2$ , on resonance as a function of the incoming probe power,  $P_p$ , for Sample 1a and 1b in Fig. 3.2. At low power very little is transmitted, whereas at high power  $T_{p,1}$  approaches unity.

### A Transmon in a 1D open transmission line

In Fig. 3.2A and B, a transmon is embedded in a 1D open transmission line with a characteristic impedance  $Z_0 \simeq 50 \Omega$ . With a coherent state input, we investigate the transmission and reflection properties of the field. The input field, transmitted field and the reflected field are denoted as  $V_{in}$ ,  $V_T$  and  $V_R$ , respectively, indicated in Fig. 4.1A. We first investigate the *coherent* properties of the reflected field and transmitted field, denoted as  $\langle V_R \rangle$  and  $\langle V_T \rangle$ , where  $\langle x \rangle = T_m^{-1} \int_0^{T_m} d\tau x(\tau)$  denotes averaging over the measurement time,  $T_m$ . Then we compare  $\langle V_R \rangle^2$  (coherent) and  $\langle V_R^2 \rangle$  (sum of coherent and incoherent) using a phase-sensitive average and phase-insensitive average, respectively.

The complex reflection coefficient for Sample 1a and b in Fig. 3.2 is  $r_{p,1} = \langle V_R \rangle / \langle V_{in} \rangle$ . Here we use the subscript “1” to label the coefficients for Sample 1. According to Eq. (2.56), we have

$$r_{p,1} = -r_0 \frac{1 - i\delta\omega_p/\gamma_{10}}{1 + (\delta\omega_p/\gamma_{10})^2 + \Omega_p^2/(\Gamma_{10} + \Gamma_l)\gamma_{10}}, \quad (4.2)$$

where  $\Gamma_l$  is the relaxation rate due to nonradiative losses (*e.g.* intrinsic losses), the decoherence rate is  $\gamma_{10} = \Gamma_{10}/2 + \Gamma_{\phi,l}$ , where  $\Gamma_{\phi,l} = \Gamma_{\phi,10} + \Gamma_l/2$ . The maximum reflection amplitude is given by  $r_0 = \Gamma_{10}/2\gamma_{10}$ . We see that both  $r_0$  and  $\gamma_{10}$  depend on  $\Gamma_{\phi,l}$  and  $\Gamma_{10}$ .  $\Omega_p$  is proportional to  $V_{in}$  and can be expressed as

[66]

$$\Omega_p = \frac{2e}{\hbar} \frac{C_c}{C_\Sigma} \left( \frac{E_J}{8E_C} \right)^{1/4} \sqrt{P_p Z_0}, \quad (4.3)$$

where  $P_p = |V_{in}|^2/2Z_0$  is the probe power. According to Eq. (2.38), the transmission coefficient  $t_{p,1} = \langle V_T \rangle / \langle V_{in} \rangle = 1 + r_{p,1}$ . The level of  $V_{in}$  is assumed to be the same as in the off-resonance value. The relaxation process is dominated by coupling to the 1D transmission line through the coupling capacitance  $C_c$  (see Fig. 3.2A,B), according to Eq. (2.58). This relaxation originates from coupling to a continuum of modes, as opposed to the cavity case, where the artificial atom is coupled solely to a single mode.

According to Eq. (4.2), for a weak ( $\Omega_p \ll \gamma_{10}$ ) resonant probe ( $\delta\omega_p = 0$ ), in the absence of both pure dephasing ( $\Gamma_{\phi,10} = 0$ ) and non-radiative decay ( $\Gamma_l = 0$ ), we should see full reflection ( $|r_{p,1}| = 1$ ) of the incoming probe field [48, 49, 110]. In that case, we also have full extinction,  $|t_{p,1}| = 0$ , of the propagating wave. This full extinction (perfect reflection) can be described as a coherent interference of the incoming wave and the scattered wave from the atom, as discussed in Fig. 1.3. This is what we observe in Fig. 4.1B, where we measure the transmittance,  $T_{p,1} = |t_{p,1}|^2$ , on resonance as a function of  $P_p$  for two samples. We see an extinction in the resonant microwaves of up to 90% (99%) for Sample 1a(b) at low incident probe power, where  $\Omega_p \ll \gamma_{10}$ . When increasing  $P_p$ , we see the strong nonlinearity of the atom, which becomes saturated by the incident microwave photons. Since the atom can only scatter one photon at a time, at high incident power,  $\Omega_p \gg \gamma_{10}$ , most of the photons pass the atom without interaction and are thus transmitted. Therefore,  $|T_{p,1}|$  tends towards unity for increasing  $P_p$ , consistent with Eq. (4.2). We define the average probe photon number coming to the transmon per interaction time as,  $\langle N_p \rangle = P_p / (\hbar\omega_p(\Gamma_{10}/2\pi))$ .

We measure  $t_{p,1}$  as a function of  $P_p$  and  $\omega_p$ . The experimental magnitude,  $|t_{p,1}|$ , and phase response,  $\varphi_{p,1}$ , for Sample 1a are shown in Fig. 4.2. The top and the bottom panels display 2D plots and the corresponding line cuts indicated by the arrows, respectively. For  $\langle N_p \rangle \ll 1$ , the magnitude response shows the strong extinction of resonant microwaves, up to 70% in amplitude or  $\sim 90\%$  in power (Sample 1a in Fig. 4.1B). The solid curves of Fig. 4.2 show fits to all magnitude and phase curves simultaneously, with three fitting parameters,  $\Gamma_{10}/2\pi = 73$  MHz,  $\Gamma_{\phi,1}/2\pi = 18$  MHz and  $\omega_{10}/2\pi = 7.1$  GHz. This corresponds to  $C_c = 25$  fF,  $\gamma_{10}/2\pi = 55$  MHz and  $r_0 = 0.67$ . We find very good agreement between theory and experiment.

In order to measure the resonant scattered field,  $V_R$ , from the atom, we need to cancel the background reflections and circulator leakage in the setup. In Fig. 4.3A, after splitting the input field, the phase and amplitude in one arm are varied such

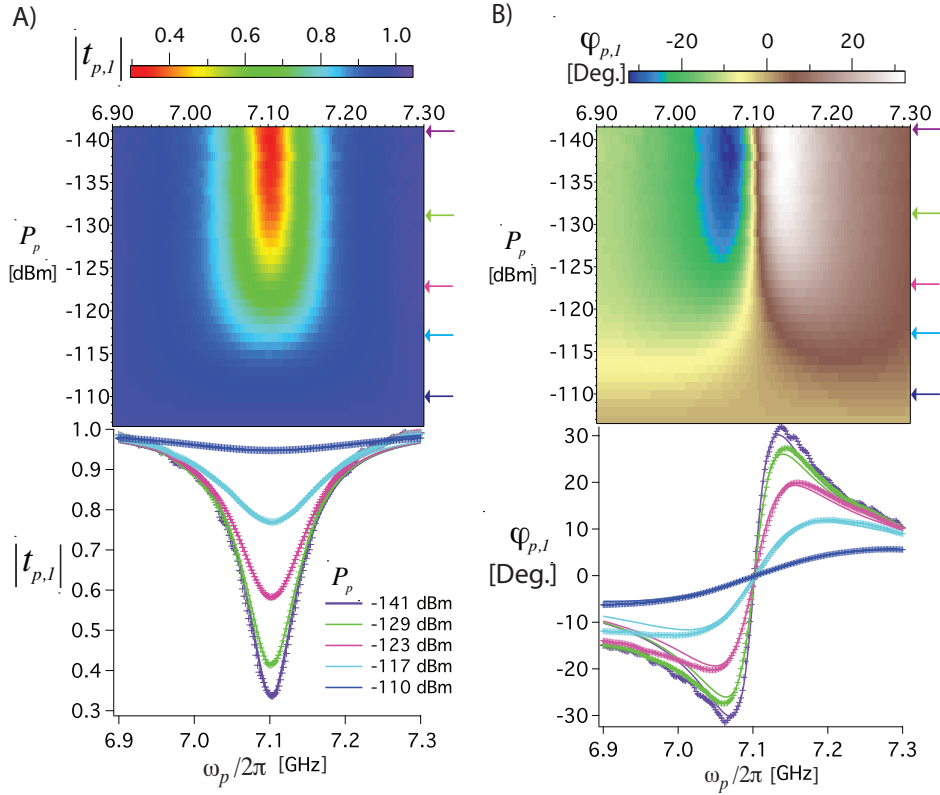


Figure 4.2:  $t_{p,1}$  as a function of  $P_p$  and  $\omega_p$  (Sample 1a). A) The magnitude response. B) the phase response. Top panel: experimental data. Bottom panel: we show the line cuts for 5 different powers, as indicated by the arrows on the top panel. The experimental data (markers) are fit simultaneously using Eq. 4.2 (curves). The extracted parameters are summaries in Table 4.1. The magnitude response demonstrates the strong coupling between the atom and resonant propagating microwaves.

that the field through a directional coupler destructively interferes with the coherent leakage from the circulator and background reflections (see green curves). We send a pulse at  $\omega_{10}$  and measure the scattered (reflected) fields from the artificial atom. We use a phase-sensitive average  $\langle V_R \rangle^2$  to capture the elastic (coherent) component of the scattered field. For the total scattered field, the sum of the elastically and inelastically scattered fields, we use a phase-insensitive average  $\langle V_R^2 \rangle$ . At the end of Chapter 2.3.2, we theoretically compared the elastic (coherent) and inelastic (incoherent) scattering in Fig. 2.14. By pulsing the input we are able to subtract the amplifier noise from our measurement of the total scattered field.

In Fig. 4.3B, we show  $\langle V_R \rangle^2$  and  $\langle V_R^2 \rangle$  as a function of resonant incident power for two different measurement bandwidths (BW). We see that the amount of the

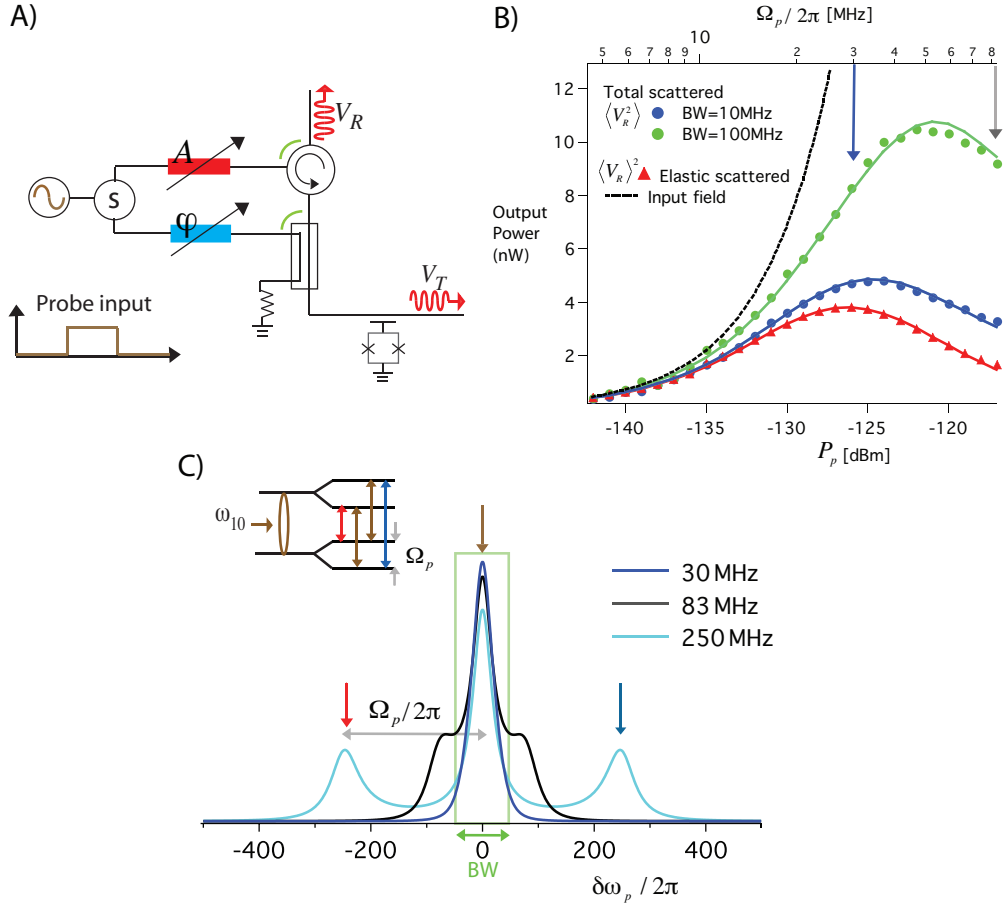


Figure 4.3: Elastic vs. inelastic scattering from the artificial atom (Sample 1b). A) Measurement setup, with cancellation of background reflection and leakage from the circulator. The green curves represent the leakage fields from the circulator and the fields through the directional coupler. By tuning the phase (blue box) and attenuation (red box), these two fields can cancel each other. B) The coherently/elastically reflected power (phase-sensitive average, red curve) or total reflected power (phase-insensitive average, green and blue curves) as a function of resonant  $P_p$  for different BW. The total power reflected is the sum of both the elastic and inelastic fields. Solid curves are the theory fits to experimental data, with extracted parameters Table 4.1. The black curve shows the input power for comparison. Note that the output power includes the 79 dB gain of the amplifiers. C) Cartoon of the spectrum of scattered power when a microwave pump is applied at  $\omega_{10}$ . When the power of the  $\omega_{10}$  pump increases, the Mollow triplet appears in the spectrum with peak separation equal to the Rabi frequency  $\Omega_p$ . (inset) Dressed-state picture of the energy levels.

inelastic field that we capture depends on the BW. The solid curves are theory fits, using the model in Fig. 4.3C (integrating the Mollow triplet), with the parameters in Table 4.1 for Sample 1b. As expected, at low incident power, we see  $\langle V_R \rangle^2 \simeq \langle V_R^2 \rangle \simeq \langle V_{in}^2 \rangle$ . This suggests that both the pure dephasing and relaxation due to non-radiative losses are small, and not resolvable from the data. At a higher incident field, where  $\Omega_p \simeq \gamma_{10}$ , more and more photons are inelastically scattered as the Mollow triplet begins to emerge. At very strong incident fields, where  $\Omega_p > \gamma_{10}$ , the main contribution to the total field is from inelastic scattering. The wider the BW, the more of the Mollow triplet we capture. The power associated with intrinsic losses is  $P_l = P_p - P_R - P_T$ , where  $P_R, P_T$  is the total power reflected and transmitted, respectively. For a resonant probe, we can estimate the loss rate  $\Gamma_l$  using the following expression [83],

$$P_l = \hbar\omega_{10}\rho_{11}\Gamma_l = \frac{2r_0\Gamma_l/(\Gamma_{10} + \Gamma_l)}{1 + \Omega_p^2/(\Gamma_{10} + \Gamma_l)\gamma_{10}}P_p,$$

where  $\rho_{11}$  is the probability for the atom to be in the first excited state. We do not have sufficiently accurate data to extract the loss rate for these measurements. We can however set an upper limit on the loss rate. For Sample 1b,  $\Gamma_{\phi,l}/2\pi \simeq 1.1$  MHz, which means that  $\Gamma_l/2\pi$  is less than 2.2 MHz. For the rest of the experimental results below, we neglect the effect of  $\Gamma_l$ , since it is very small.

### A Transmon at the end of a 1D transmission line

In Fig. 3.2C, a transmon is embedded at the end of a 1D open transmission line with a characteristic impedance  $Z_0 \simeq 50 \Omega$ . As discussed in Chapter 2.3.4, because of the boundary condition (Fig. 4.4A), all the input field will be reflected either coherently or incoherently. With a coherent state input, we investigate the *coherent* reflection properties of the field, defining  $r_{p,2} = \langle V_R \rangle / \langle V_{in} \rangle$ . Here we use the subscript “2” to label the coefficients for Sample 2. The input field and the reflected field are denoted as  $V_{in}$  and  $V_R$ , respectively, indicated in Fig. 4.4A. According to Eq. (2.79), for a resonant probe field,  $\omega_p = \omega_{10}$ , the reflection coefficient,  $r_{p,2}$ , is expressed as

$$r_{p,2} = 1 - \frac{2}{1 + 2\Gamma_{\phi,10}/\Gamma_{10} + 2\Omega_p^2/\Gamma_{10}^2}. \quad (4.4)$$

In Fig. 4.4B, we show the measured  $|r_{p,2}|$  as a function of  $P_p$ . The experimental data (markers) are fit using Eq. (4.4) (solid curve) with  $\Gamma_{\phi,10}$  and  $\Gamma_{10}$  extracted from Fig. 4.4C,D. For a weak resonant probe, where  $\Omega_p \ll \gamma_{10}$ ,  $\omega_p = \omega_{10}$ , the incident field is reflected by the atom with  $|r_{p,2}| \simeq 0.52$ .  $|r_{p,2}|$  is determined by the ratio between pure dephasing,  $\Gamma_{\phi,10}$  and relaxation rate  $\Gamma_{10}$ , according to

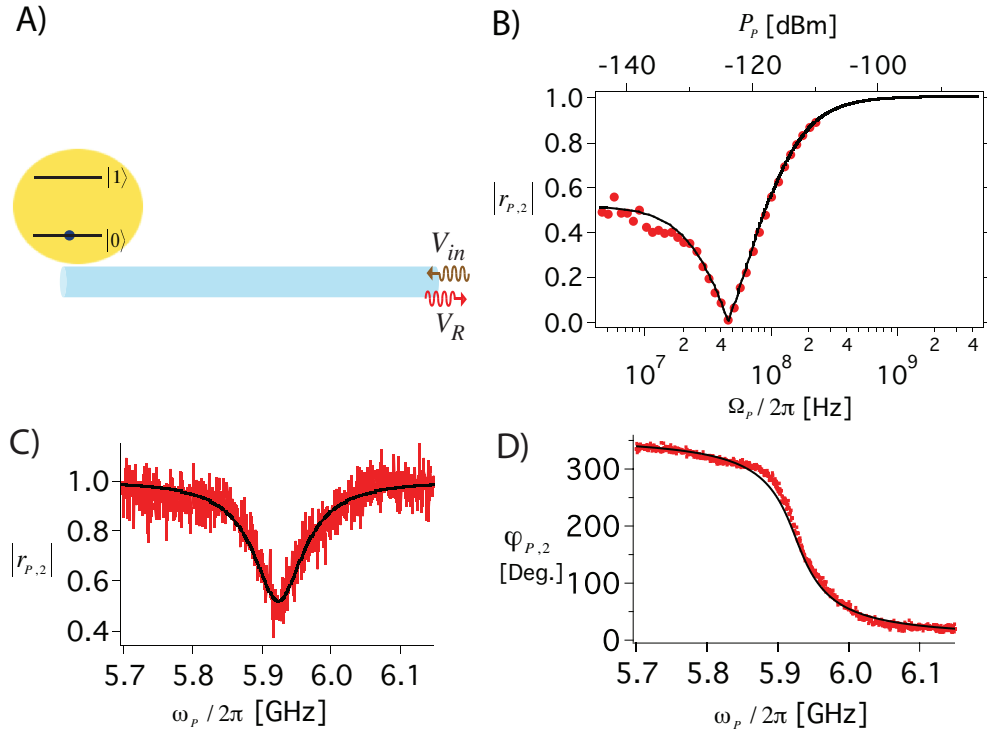


Figure 4.4: A) Cartoon of scattering of resonant coherent state from a two-level atom at a single ended 1D waveguide. The micrograph of the measured sample is shown in Fig. 3.2C (Sample 2). B)  $|r_{p,2}|$  on resonance ( $\omega_p = \omega_{10}$ ) as a function of  $P_p$ . C) and D) shows  $r_{p,2}$  as a function of probe frequency for a weak probe, where  $\Omega_p \ll \gamma_{10}$ . C) Magnitude response. D) Phase response. The theoretical curves (solid black) use the parameters in Table 4.1.

Sample	$E_J/h$	$E_C/h$	$E_J/E_C$	$\omega_{10}/2\pi$	$\omega_{21}/2\pi$	$\Gamma_{10}/2\pi$	$\Gamma_{\phi,l}/2\pi$	Ext.
1a	12.7	0.59	21.6	7.1	6.38	0.073	0.018	90%
1b	10.7	0.35	31	5.13	4.74	0.041	0.0011	99%
1c	—	—	—	4.88	4.12	0.017	0.0085	75%

Sample	$E_J/h$	$E_C/h$	$E_J/E_C$	$\omega_{10}/2\pi$	$\omega_{21}/2\pi$	$\Gamma_{10}/2\pi$	$\Gamma_{\phi,10}/2\pi$	$ r_{p,2} $
2	11.99	0.42	28.5	5.92	5.50	0.08	0.0128	52%

Table 4.1: Parameters for Samples 1a, 1b, 1c and 2. Images of Sample 1a, 1b and 2 are shown in Fig. 3.2A, B and C, respectively. All dimensional quantities are in GHz. Ext. is the extinction of the transmitted field. Note that one of the Josephson junctions was broken in Sample 1c, therefore,  $\omega_{10}$  and  $\omega_{21}$  could not be tuned with  $\Phi$ .

Eq. (4.4). As the probe amplitude increases, there is a perfect destructive interference between the field reflected by the atom and the field reflected by the boundary condition. This leads to  $|r_{p,2}| \simeq 0$ , when  $\Omega_p \sim 2\pi \times 47$  MHz, as expected. For a very high probe field, where  $\Omega_p \gg \gamma_{10}$ , the atom is saturated. All the field is reflected by the boundary condition, giving  $|r_{p,2}| = 1$ . For a weak probe, where  $\Omega_p \ll \gamma_{10}$ , according to Eq. (2.79), the reflection coefficient becomes

$$r_{p,2} = 1 - \frac{\Gamma_{10}}{\gamma_{10}} \frac{1 - i\delta\omega_p/\gamma_{10}}{1 + (\delta\omega_p/\gamma_{10})^2}. \quad (4.5)$$

In Fig. 4.4C and D, we plot the measured magnitude and phase of  $r_{p,2}$  as a function of probe frequency. The experimental data (markers) are fitted using Eq. (4.5) (solid curves). In Fig. 4.4D, we see that the phase shift between on and off resonance is  $\pi$ . The missing signal in Fig. 4.4B and C is emitted incoherently (inelastically) with random phase. This effect is the same as a transmon in open transmission line case, as discussed in the previous section, see Fig. 4.3B.

## 4.1.2 Tunable Artificial Atom

To further characterize Sample 1a, the frequency of the resonance dip in transmission in Fig. 4.2A is mapped as a function of magnetic flux  $\Phi$  with a weak probe, where  $\Omega_p \ll \gamma_{10}$  (see Fig. 4.5A). In the transmon regime, where  $E_J/E_C \geq 20$ ,  $\omega_{10}$  is tuned by  $\Phi$  according to Eq. (4.1). If we increase  $P_p$  to a level such that the 0-1 transition is saturated, two-photon (0-2) transitions occur, as indicated in the grey curve of Fig. 4.5B. The transition frequency corresponds to  $(\omega_{10} + \omega_{21})/2$ , where  $\omega_{21}$  is the 1-2 transition energy. We use a Cooper-Pair box [66] Hamiltonian with 50 charge states to fit the spectrum of the atom and extract  $E_J = 12.7$  GHz

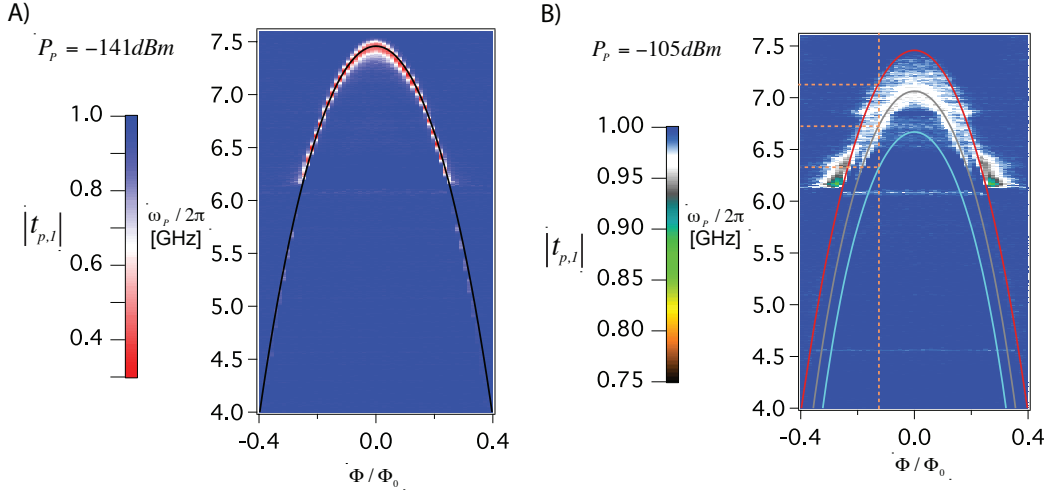


Figure 4.5:  $|t_{p,1}|$  as a function of  $\Phi$  for Sample 1a. A) At weak probe power, where  $\Omega_p \ll \gamma_{10}$ . The black curve is the theory fit to the 0-1 transition. B) At high probe power, where  $\Omega_p \gg \gamma_{10}$ . The red and blue curve correspond to the 0-1 and 1-2 transition respectively. The grey curve is the two-photon (0-2) transition. The orange dashed line indicates the flux bias point and the corresponding  $\omega_{10}$ ,  $\omega_{20}/2$ ,  $\omega_{21}$  for Fig. 4.2 and Fig. 4.7A, C and D. There is a stray resonance around 6.1 GHz.

and  $E_C = 590$  MHz for Sample 1a. The extracted parameters are summarized in Table 4.1.

As can be seen in Fig. 4.1B, the extinction efficiency of Sample 1b is much better than Sample 1a. This is because Sample 1a has a relatively low  $E_J/E_C \sim 21.6$ , which is barely in the transmon limit. For this value of  $E_J/E_C$ , charge noise still plays an important role as the energy band of the 0-1 transition still depends on charge, see Fig. 2.6. For Sample 1a we find that the charge dispersion is 7 MHz (see Fig. 4.6) and the dephasing is dominated by the charge noise. By increasing  $E_J/E_C$  to 31, we see much less dephasing in Sample 1b, which gives nearly perfect extinction of propagating resonant microwaves. Note that, the anharmonicity between  $\omega_{10}$  and  $\omega_{21}$  of Sample 1b is close to  $E_C$ . This is not quite the case for Sample 1a due to its low  $E_J/E_C$  [66].

### 4.1.3 Mollow Triplet and Autler-Townes Splitting

As shown in Fig. 4.5B and Fig. 4.6, the transmon has higher level transitions. In particular, we are interested in the 1-2 transition with angular frequency  $\omega_{21}$ . By using 2-tone spectroscopy, the  $\omega_{21}$  transition can be directly measured. In Sample 1a, we can saturate the  $\omega_{10}$  transition by applying a pump field at  $\omega_{10}/2\pi = 7.1$

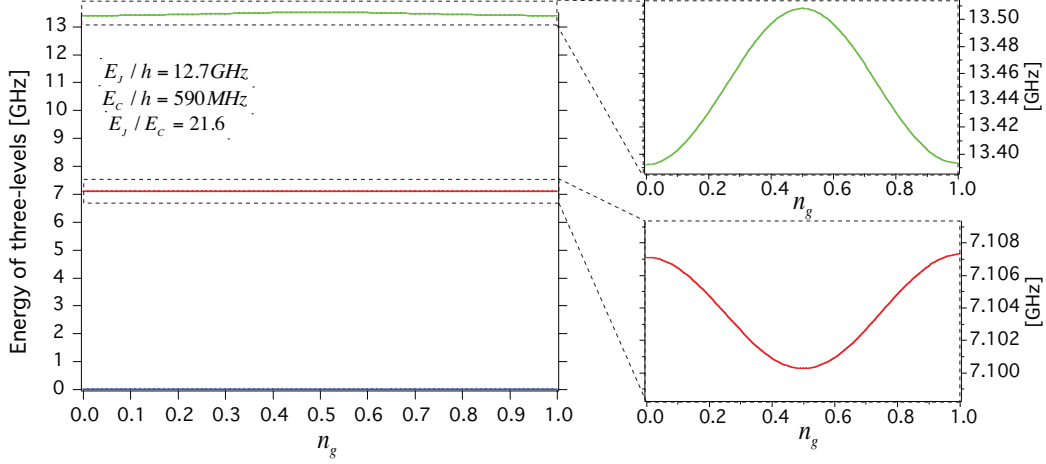


Figure 4.6: Based on the parameters of Sample 1a in Table 4.1, we plot the three lowest energy levels of the transmon as a function of normalized gate charge,  $n_g$ . The right plots show the magnification of the first excited and second excited states. The charge dispersion of the transmon in Sample 1a for the first excited state and second excited state are 7 MHz and 110 MHz, respectively.

GHz, and measure the transmission properties using a weak probe at  $\omega_p$ . As the pump power is increased, the population of the first excited state increases, therefore, we start to observe photon scattering from the 1-2 transition, which appears as a dip in transmission at  $\omega_p = \omega_{21}$ , see Fig. 4.7A. The dip in transmission grows until the 0-1 transition becomes fully saturated. From this, we extract  $\omega_{21}/2\pi = 6.38$  GHz for Sample 1a. Therefore, the two-photon (0-2) transition should be equal to 6.74 GHz, consistent with the observation in Fig. 4.5B. The linewidth of the  $\omega_{21}$  transition is around 120 MHz, this dephasing mainly comes from the charge dispersion. Further increasing the pump power at  $\omega_{10}$ , we observe the well known Mollow triplet [22, 89] (Fig. 4.7B, Sample 1c). The Rabi splitting of the triplet can be used to calibrate the incident power at the atom. The Mollow triplet can be explained in the dressed-state picture, where the two lowest levels split by the Rabi frequency, see Chapter 2.3.3. These four states give three different transitions, indicated by red, brown and blue arrows in the inset of Fig. 4.7B, consistent with Fig. 4.3C. Note that the way we observed the triplet here is different from that in [22]. We probe the transmission of these triplet transitions instead of looking at the emission spectrum. We see that the center transition is much less visible, because we pump at the frequency which saturates that transition. Recently, similar results has been observed in Ref. [57].

With a weak resonant probe field,  $\Omega_p \ll \gamma_{10}$ ,  $\omega_p = \omega_{10}$ , and a strong resonant,  $\omega_c = \omega_{21}$ , control field, the 0-1 resonance dip splits with the magnitude of  $\Omega_c$

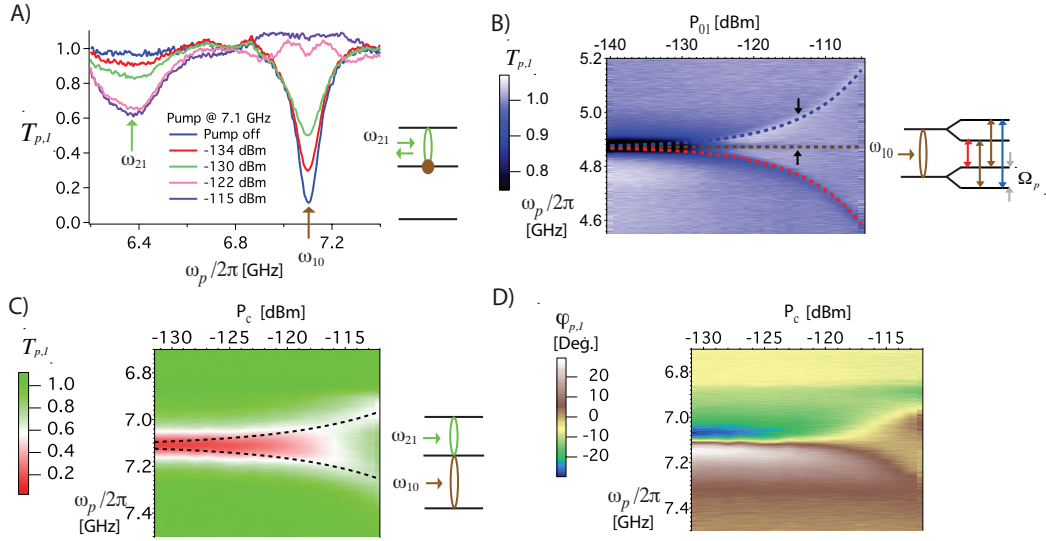


Figure 4.7: Two-tone spectroscopy of Sample 1a in (A), (C) and (D), Sample 1c in (B). A) As the frequency of a weak probe field is swept, a second microwave drive is continuously applied at  $\omega_{10}$  with increasing powers. We see a second dip gradually appear in the probe transmission response. B)  $T_{p,1}$  as a function of probe frequency and pump power. As the power of  $\omega_{10}$  further increases, we see the Mollow triplet. The dashed lines indicate the calculated position of the triplet. (Inset) Schematic picture of triplet transitions in the dressed-state picture. Note that we use Sample 1c, where  $\omega_{10}/2\pi = 4.88$  GHz. (C) and (D) Magnitude and phase response of a second microwave applied at  $\omega_{21}$  with variable power,  $P_c$ . As  $P_c$  increases, we see induced transmission at  $\omega_p = \omega_{10}$ . With a strong drive applied, the Autler-Townes splitting appears with the magnitude of  $\Omega_c/2\pi$  (Black dashed lines).

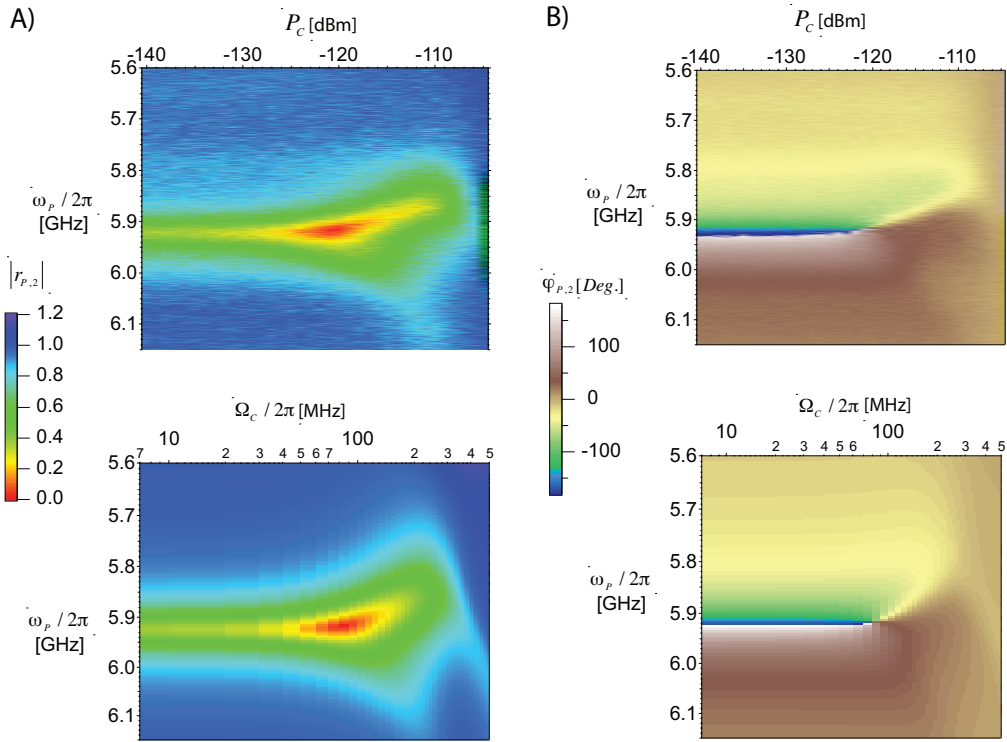


Figure 4.8:  $r_{p,2}$  as a function of  $\omega_p$  and  $P_c$  for a weak probe, where  $\Omega_p \ll \gamma_{10}$  (Sample 2). A) Magnitude response of the probe. B) Phase response of the probe. Top: experimental data. Bottom: Theory calculations (performed by A. F. Kockum). Similar to Eq. 4.3, we have  $\Omega_c \propto \sqrt{P_c}$ . Applying a strong drive, we see an asymmetric Autler-Townes splitting.

[51]. This is known as the Autler-Townes Splitting (ATS) [111]. The magnitude and phase response are shown in Fig. 4.7C and D respectively. In the magnitude response, we see that the transmon becomes transparent for the probe at  $\omega_p = \omega_{10}$  at sufficiently high control power. The theory of EIT from ATS was described in Chapter 2.4. In the phase response, we see the probe phase,  $\varphi_p$ , depends on the control power,  $P_c$ .

For Sample 2, the 1-2 transition can also be measured using 2-tone spectroscopy. We find  $\omega_{21}/2\pi = 5.5$  GHz. With similar techniques, we apply two continuous tones, the probe at  $\omega_p \sim \omega_{10}$  and the control at  $\omega_c = \omega_{21}$ , we measure  $r_{p,2}$  as a function of  $P_c$  and  $\omega_p$  for a weak probe,  $\Omega_p \ll \gamma_{10}$ . The magnitude and phase responses are shown in Fig. 4.8A, B, respectively. We observe the Autler-Townes splitting for  $\Omega_c > \gamma_{10}$  in Fig. 4.8A. However, we see that this Autler-Townes splitting is very asymmetric, this is due to the fact that  $\Omega_c$  is close to the anharmonicity ( $\sim 420$  MHz), so that the upper levels of the transmon are involved. The theoretical plots take 6 transmon levels into account, as shown at the bottom of Fig. 4.8A and B. We observe a similar asymmetric behavior for Sample 1a at a higher incident power, due to the higher anharmonicity ( $\sim 720$  MHz) of Sample 1a.

## 4.2 Quantum Applications at the Single-Photon Level

In the following application section, we demonstrate three quantum devices based on the quantum-optical effects described in Section 4.1, which could be utilized in a microwave quantum network. By making use of the ATS in Fig. 4.7C, we demonstrate a router for single photons (see Appended paper I). By using the strong nonlinearity of the atom in Fig. 4.1B, we demonstrate a photon-number filter, where we convert classical coherent microwaves to nonclassical microwave fields (see Appended paper II). By utilizing the induced phase shift in Fig. 4.7D and Fig. 4.8B, we demonstrate a cross-Kerr medium in both samples, enabling photon-photon interaction at the single-photon level (see Appended paper III).

### 4.2.1 The Single-Photon Router

The operating principle of the single-photon router is explained as follows. In the time domain (see Fig. 4.9A), we input a constant weak probe in the single-photon regime, where  $\langle N_p \rangle \ll 1$ , at  $\omega_p = \omega_{10}$ . We then apply a strong control pulse, around 30 dB more than the probe power, at the  $\omega_{21}$  frequency. When the control is off, the probe photons are reflected by the atom, and delivered to output port 1. When the control is on, the probe photons are transmitted based on the ATS, and delivered to output port 2. We measure the reflected and transmitted

probe power simultaneously in the time domain. This is crucial to investigate if the microwave photon transport is a fully coherent process, *i.e.* the transmission dip seen in Fig. 4.2A is because of the photons are being reflected (not due to dissipation). Note that the measured quantities are phase sensitive since we measure  $\langle V \rangle^2$  rather than  $\langle V^2 \rangle$ . That is  $\langle V \rangle^2$  is only sensitive to the phase coherent part of the signal. The simplified experimental setup is shown in Fig. 4.9A.

The results are shown in Fig. 4.9B and C for Sample 1a and 1b, respectively. As expected, when the control signal is on, the probe power of the transmitted signal is increased and we see a corresponding decrease in the reflected probe signal. In Fig. 4.9C (B), 99% (90%) probe on-off ratio is achieved in both reflection and transmission for Sample 1b (1a). The ringing signal in Fig. 4.9B,C is an artifact from the digitizer. In Fig. 4.9C (D), we use a square (Gaussian) control pulse with a duration of 1  $\mu$ s (10ns) for Sample 1b. In Fig. 4.9D, the time resolution of our digitizer/arbitrary waveform generator is 5 ns, which prevents us from accurately measuring pulses less than about 10 ns. In Fig. 4.9E, we change the width of the control pulse from 50 ns to 1  $\mu$ s. We see that the on-off ratio does not depend on the control time. In the setup of Fig. 4.9A, we send  $\omega_{10}$  and  $\omega_{21}$  into opposite ports. We can also send pulses in the same port using a microwave combiner and we get the same result, as expected. Note that we use the on-off ratio  $[R_{p,1}(\Omega_c) + R_b]/[R_{p,1}(0) + R_b]$ , where  $R_{p,1}(\Omega_c)$  and  $R_{p,1}(0)$  respectively represents reflectance when the control is on and off, and  $R_b$  accounts for background reflections in the line and leakage through circulator 1 [Fig. 4.9(A)]. We note that this data was taken without canceling the leakage as shown in Fig. 4.3A. The on-off ratio of the transmittance is expressed as  $T_{p,1}(0)/T_{p,1}(\Omega_c)$ , where  $T_{p,1}(\Omega_c)$  and  $T_{p,1}(0)$  represents the transmittance when the control is on and off, respectively. Theoretically, for Sample 1b, according to Eq. (2.94), when the control signal is off, we have  $R_{p,1}(0) = |\Gamma_{10}/2\gamma_{10}|^2 \simeq 91\%$ ,  $T_{p,1}(0) = |1 - \Gamma_{10}/2\gamma_{10}|^2 \simeq 0.2\%$ ,  $D_{\phi,l}(0) \simeq 8.8\%$ . When the control signal is on, we have  $R_{p,1}(\Omega_c) \simeq 0$ ,  $T_{p,1}(\Omega_c) \simeq 1$ ,  $D_{\phi,l}(\Omega_c) \simeq 0$ , where  $D_{\phi,l}$  refers to the total dissipation associated with intrinsic losses and pure dephasing.

The speed of our router Sample 1a (b) is predicted to be  $1/\Gamma_{10} \sim 2$  ns (4 ns). We show that the router works well down to the time limit of our instruments. By engineering the relaxation rate, it should be possible to achieve even faster switching times in the subnanosecond regime. In addition, the routing efficiency,  $R_{p,1} = |r_0|^2$ , can be improved by further reducing  $\Gamma_{\phi,10}$ . The improvement in Sample 1b compared to Sample 1a was achieved by increasing the  $E_J/E_C$  ratio. This reduced the sensitivity of the transmon to charge noise and, therefore, the dephasing.

Our router can also easily be cascaded to distribute photons to many output channels. Fig. 4.10A shows 4 atoms (A,B,C,D) in series, each separated by a circulator. The  $\omega_{10}$  of the atoms are the same, while the  $\omega_{21}$  are different. This

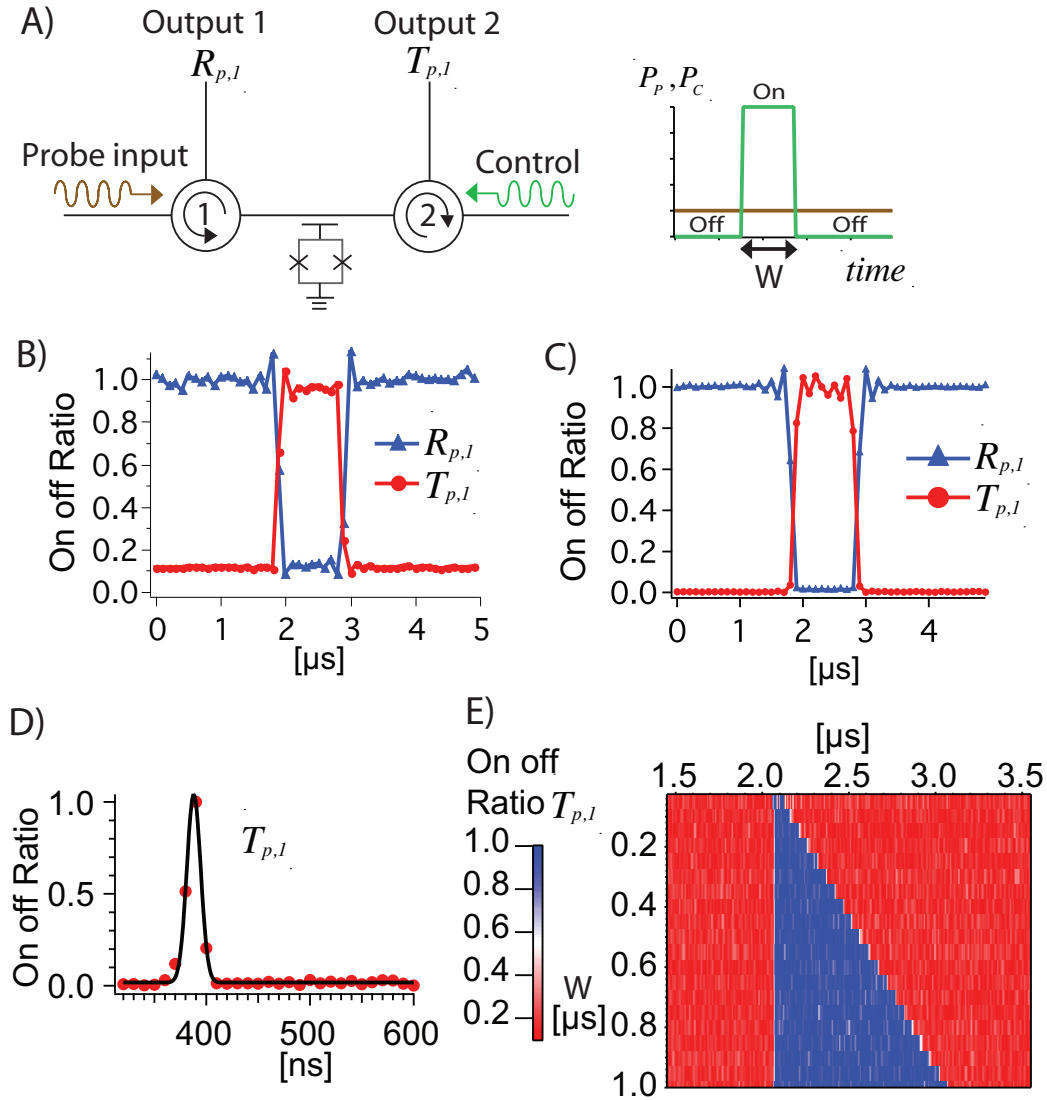


Figure 4.9: The Single-Photon Router, data in B, E for Sample 1a, data in C, D for Sample 1b. (A) Measurement setup and the control pulse sequence. A strong control pulse at  $\omega_c = \omega_{21}$  is used to route a weak continuous microwave  $\omega_p = \omega_{10}$ . Depending on whether the control pulse is on or off, the probe field is delivered to output port 2 or 1, respectively. (B) Normalized on-off ratio (see text) of the transmittance ( $T_{p,1}$ ) and reflectance ( $R_{p,1}$ ) of  $\omega_p$  measured simultaneously. (C) Same for Sample 1b, although normalized on-off ratio of  $T_{p,1}$  and  $R_{p,1}$  are measured separately. The control pulse is shaped as a square pulse with  $1 \mu s$  duration for both B) and C). (D) a Gaussian pulse with a duration of  $10 ns$ , we see up to 99% on-off ratio. The black curve in (D) is a Gaussian fit to the data. (E) Data for Sample 1a, Normalized on-off ratio of the transmittance ( $T_{p,1}$ ) as a function of pulse width,  $W$ , from  $50 ns$  to  $1 \mu s$ . We see  $T_{p,1}$  remain constant, regardless the width of the pulse.

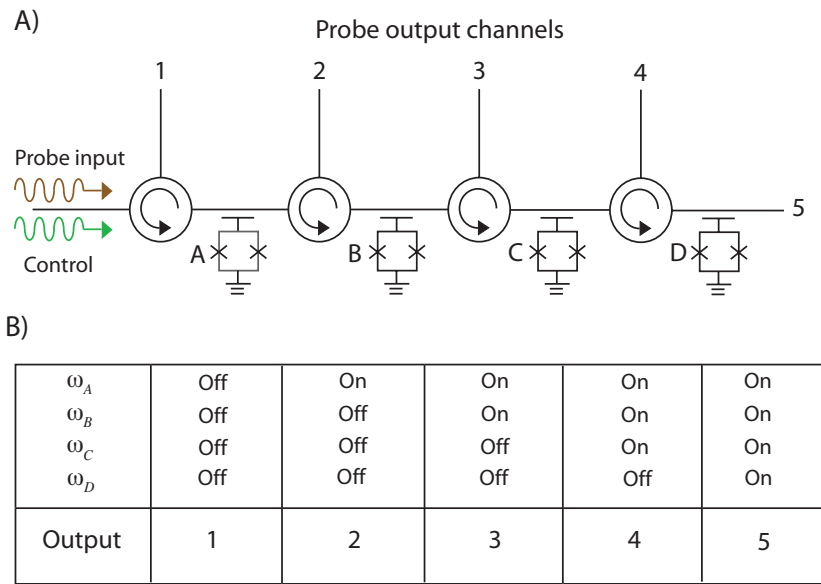


Figure 4.10: Multiport router. (A) Cartoon of a multiport router: single-photon routers cascaded to produce many output channels. Here we show a 5 port router using 4 atoms (A,B,C,D) in series, each separated by a circulator. The  $\omega_{10}$  of the atoms are the same, while the 1-2 transition frequencies,  $\omega_{21,A} \neq \omega_{21,B} \neq \omega_{21,C} \neq \omega_{21,D}$ , are different. By turning on and off control tones at the various 1-2 transition frequencies, we can determine the output channel of the probe field, according to the table in B).

arrangement can be designed in a straightforward manner by controlling the ratio of  $E_J/E_C$ . By turning on and off control tones at the various 1-2 transition frequencies, we can determine the output channel of the probe field, according to the table in Fig. 4.10B. For instance, if we want to send the probe field to channel 4, we apply three control tones at  $\omega_{21,A}$ ,  $\omega_{21,B}$  and  $\omega_{21,C}$ . Note that regardless of the number of output channels, all the control tones and the probe tone can be sent through the same input port. Theoretically, the maximum number of output channels depends on the ratio between the anharmonicity and the width of the 1-2 transition,  $\gamma_{21}$ . Thus, there is a trade off between efficiency and the number of outputs. The photon router can also be achieved by detuning  $\omega_{10}$  through an external magnetic flux,  $\Phi$ . However, in this scheme, an additional on-chip fast flux line is needed for each atom. This will increase the complexity of the system.

### 4.2.2 The Photon-Number Filter

In Fig. 4.1B, we demonstrated the nonlinear nature of the two-level artificial atom. This naturally comes from the fact that atoms can only reflect one photon at a time. To reveal the nonclassical character of the reflected field, we investigate its statistics in this section. In particular, we show that the reflected field is antibunched [49]. In addition, we also show that the transmitted field is superbunched [49]. The theoretical background was discussed in Chapter 2.5. The experimental results are based on Sample 1b.

The incident coherent state can be written in terms of a superposition of photon number states, with a poissonian distribution of probability (see Fig. 2.22B). For a weak probe field with  $\langle N_p \rangle < 0.5$ , this coherent field can be well approximated using a basis of just the first three photon-number states. Roughly speaking, when one-photon state is incident, the atom reflects it, leading to antibunching in the reflected field. Together with the zero-photon state, the reflected field still however maintains first-order coherence, as there is a well defined phase between the zero and one-photon states. Because the atom is not able to scatter more than one photon at a time, a two-photon incident state has a much higher probability of transmission, leading to superbunching in the transmitted field [49, 104]. In this sense, our single artificial atom acts as a photon-number filter, which filters and reflects the one-photon number state from a coherent state. This process leads to a photon-number redistribution between the reflected and the transmitted fields [104].

The measurement setup is shown in Fig. 3.4B. This allows us to measure Hanbury Brown-Twiss [100] type power-power correlations. We apply a resonant coherent microwave field at  $\omega_p = \omega_{10}$ . Depending on the choice of the input port, we measure the statistics of the reflected or transmitted field. The signal then propagates to a “beam splitter”, which in the microwave domain is realized

by a hybrid coupler, where the outputs of the beam splitter are connected to two nominally identical LNAs with system noise temperatures of approximately 7 K, as characterized in Table 3.2. We assume that the amplifier noise generated in the two independent detection chains is uncorrelated. After further amplification, the two voltage amplitudes of the outputs are captured by a pair of vector digitizers.

The second-order correlation function provides a statistical tool to characterize the field. According to appendix D, it can be expressed as

$$g^{(2)}(\tau) = 1 + \frac{\langle \Delta P_1(t) \Delta P_2(t + \tau) \rangle}{[\langle P_1(t) \rangle - \langle P_{1,N}(t) \rangle][\langle P_2(t) \rangle - \langle P_{2,N}(t) \rangle]},$$

where  $\tau$  is the delay time between the two digitizers and  $P_1, P_2$  are the output powers at ports 1 and 2, respectively (see Fig. 3.4B).  $P_{1,N}, P_{2,N}$  are the amplifier noise in ports 1 and 2 respectively, when the incident source is off. Therefore,  $[\langle P_i(t) \rangle - \langle P_{i,N}(t) \rangle]$  represents the net power of the field from output port  $i$ , where  $i = 1, 2$ .  $\langle \Delta P_1 \Delta P_2 \rangle$  is the covariance of the output powers in ports 1 and 2, defined as  $\langle (P_1 - \langle P_1 \rangle)(P_2 - \langle P_2 \rangle) \rangle$ . In Fig. 4.11A, we show  $g^{(2)}$  as a function of delay time,  $\tau$ , for a thermal state with two different filter bandwidths, and also for a coherent state. For the thermal states,  $g^{(2)}(0) = 2$  regardless of the filter bandwidth BW. The width of  $g^{(2)}(\tau)$  for the thermal state is determined by the filter function. For the single-pole filter we used, we have  $g^{(2)}(\tau) = 1 + e^{-2\pi BW|\tau|}$ . The solid curves of the thermal state in Fig. 4.11A show this equation with no free fitting parameters. The chaotic (thermal) state is generated by amplifying the room-temperature noise of a 50  $\Omega$  resistor. For a coherent state, we expect  $g^{(2)}(\tau) = 1$ . This is indeed what we find if our atom is off-resonance from our applied coherent source.

We had a trigger jitter of  $\pm 1$  sample between the two digitizers. To minimize the effect of this trigger jitter, we oversample and then digitally filter (average) the data in all the  $g^{(2)}$  measurements. Here, the sampling frequency is set to  $10^8$  samples/s with a digital filter with a bandwidth of  $BW = 55$  MHz applied to each digitizer for all the measurements.

After these initial calibration measurements, we measured the second-order correlations of the field transmitted through our qubit. In Fig. 4.11B, we see superbunching of the photons [49] with  $g^{(2)}(\tau = 0) = 2.31 \pm 0.09 > 2$  at  $P_p = -129$  dBm ( $\langle N_p \rangle \simeq 0.8$ ) for the transmitted field. Superbunching occurs because the one-photon state of the incident field has been selectively reflected and thus filtered out from the transmitted signal, while the two-photon state is more likely to be transmitted. The three-photon state and higher number states are neglected. The transmitted state generated from our qubit is thus bunched even more than a thermal state, which has  $g_{therm}^{(2)}(\tau = 0) = 2$ . Therefore, it is called a superbunched state. Fig. 4.11C shows the theoretical curves of  $g^{(2)}(\tau)$  for the transmitted field

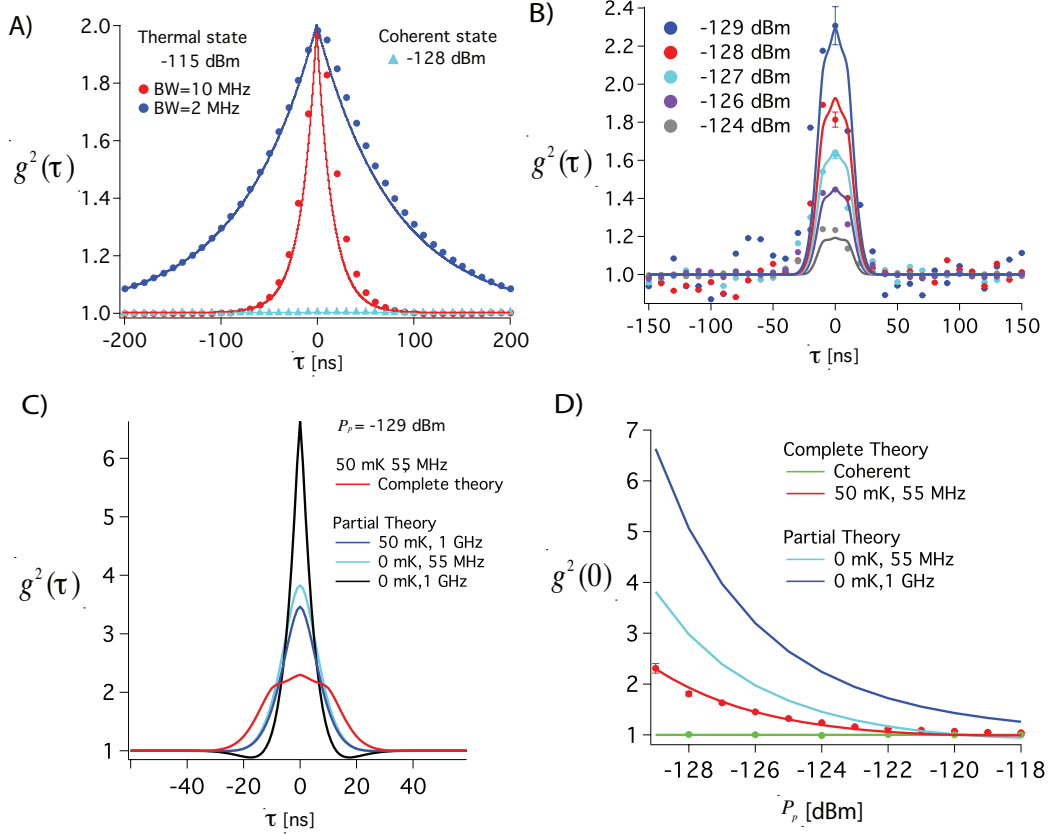


Figure 4.11: Second-order correlation function of the transmitted fields generated by the artificial atom (Sample 1b). A)  $g^{(2)}$  of a thermal state and a coherent state as a function of delay time  $\tau$ . B)  $g^{(2)}$  of the resonant transmitted microwaves as a function of delay time for five different incident powers. The peculiar feature of  $g^{(2)}$  around zero in the theory curves is due to the trigger jitter model. C) Influence of BW, temperature and jitter on superbunching. The red curve is the complete theory, which includes jitter. D)  $g^{(2)}(0)$  of resonant transmitted field as a function of incident power. The result for a coherent state is also plotted. We see that the transmitted field statistics (red curve) approaches that of a coherent field at high incident power, as expected. For BW=1 GHz at 0 mK, we see very strong superbunching at low incident power in the theory plot. The error bar indicated for each data (markers) set is the same for all the points. The solid curves in A), B), C) and D) are the theory curves. For all measurements shown here we find,  $g^{(2)}(\infty) = 1$ , as expected.

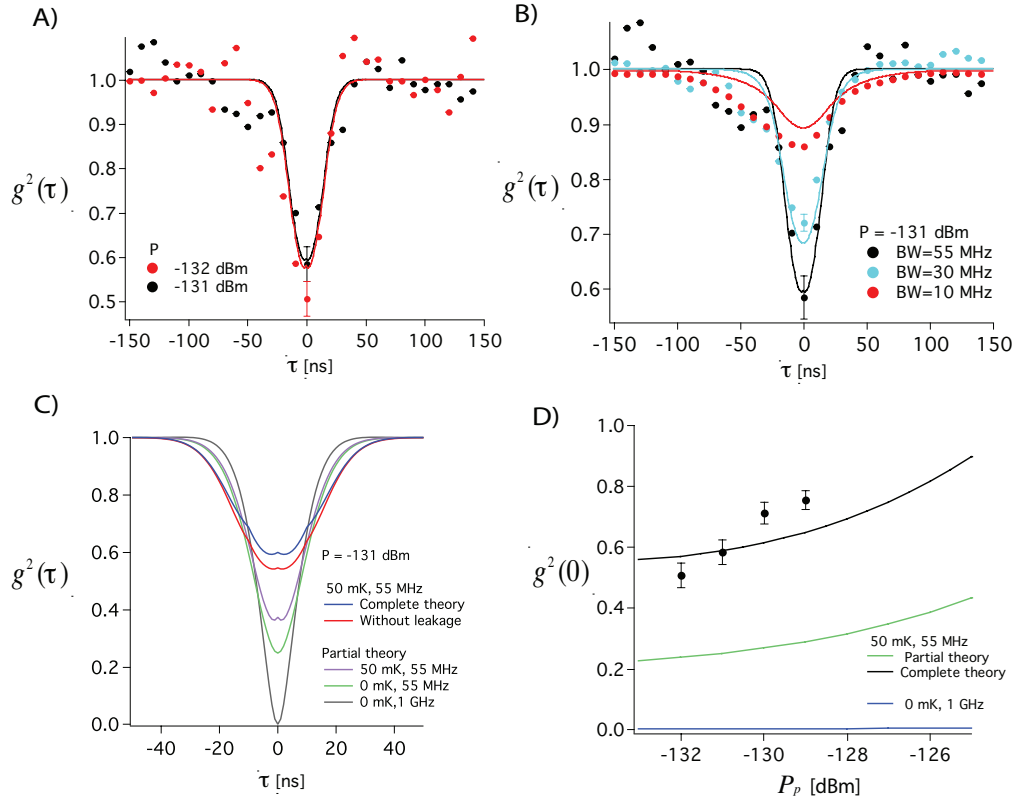


Figure 4.12: Second-order correlation function of reflected fields generated by the artificial atom (Sample 1b). A)  $g^{(2)}$  of a resonant reflected field as a function of delay time. We see the antibunched behavior of the reflected field. The error bar indicated for each data (markers) set is the same for all the points. B)  $g^{(2)}$  of a resonant reflected field as a function of delay time at  $-131$  dBm for different filter bandwidths. As the bandwidth decreases, the antibunching dip vanishes. C) Influence of BW, temperature, leakage and jitter on antibunching. D)  $g^{(2)}(0)$  as a function of incident power. The black curve, labeled “complete theory”, includes all four non-idealities (see text). The green curve, labeled “partial theory”, only includes a finite temperature and bandwidth. As the BW decreases or the incident power increases, the degree of antibunching decreases. The solid curves in A), B), C) and D) are the theory curves. Leakage arises from background reflections in the line and leakage through circulator. We assume the phase between the leakage and the field reflected by the atom is  $0.37\pi$ .

under the influence of various effects. For the case of BW=1 GHz at 0 mK, indicated by the black curve,  $g^{(2)}$  exhibits very strong bunching at  $\tau = 0$ . At a later delay,  $\tau \sim 15$  ns,  $g^{(2)}$  for the transmitted field even appears antibunched [49], this is however not resolved in the experimental data. For the other curves, we see the degrading of superbunching due to the influence of BW, temperature and jitter. In Fig. 4.11D, we plot  $g^{(2)}(0)$  as a function of incident power, and clearly see the (super)bunching behavior decreases as the incident power increases. For high powers, where  $\langle N_p \rangle \gg 1$ , we find  $g^{(2)}(\tau) = 1$ . This is because most of the coherent signal then passes through the transmission line without interacting with the qubit owing to the saturation of the atomic response. We also plot the theoretical curves at 0 mK for two different BW.

In Fig. 4.12, we plot the measured  $g^{(2)}(\tau)$  of the reflected field from our atom. At low powers, where  $\langle N_p \rangle \ll 1$ , we clearly observe antibunching of the field [49]. The trace here was averaged over  $2.4 \times 10^{11}$  measured quadrature field samples (2 Tbyte of data), computed and averaged over 17 hours. We correct for slow drifts, *e.g.* in the amplifier gain, every 5 minutes by switching on and off the incident source.

The antibunching behavior at  $P_p = -131$  dBm ( $\langle N_p \rangle \sim 0.4$ ),  $g^{(2)}(0) = 0.55 \pm 0.04$ , reveals the nonclassical character of the field. Ideally, we would find  $g^{(2)}(0) = 0$  as the atom can only reflect one photon at a time. The non-zero  $g^{(2)}(0)$  we measured originates from four effects: 1) a thermal field at 50 mK temperature, 2) a finite filter BW, 3) trigger jitter between the two digitizers and 4) stray fields including background reflections in the line and leakage through circulator 1 [Fig. 3.4B]. The effects of these factors on our measured antibunching are shown in the theory plot Fig. 4.12C. The complete theory curves include all four non-idealities. The partial theory curves include 1) and 2), but not 3), 4). For small BW, within the long sampling time, the atom is able to scatter multiple photons. If  $\text{BW} \ll \Gamma_{10}, \Omega_p$ , the antibunching dip vanishes entirely. This interplay between BW and  $\Omega_p$  produces a power dependent  $g^{(2)}(0)$ , as shown in Fig. 4.12D. In the ideal case, *i.e.* for a sufficiently wide BW (1 GHz) at 0 mK, the theory gives  $g^{(2)}(0) = 0$ , as expected.

A single-mode resonator is used to model the digital filter. The theoretical curves in Fig. 4.11 and Fig. 4.12 are based on a master equation describing both the transmon and the resonator using the formalism of cascaded quantum systems [83], described in Appended paper V. The trigger jitter is modeled by the following procedure: the value of  $g^{(2)}(\tau)$  at each point is replaced by the average value of  $g^{(2)}(\tau-10$  ns),  $g^{(2)}(\tau)$  and  $g^{(2)}(\tau+10$  ns). We extract 50 mK from all these fits, with no additional free fitting parameters.

As we have shown, the single artificial atom acts as a photon-number filter, which selectively filters out the one-photon number state from a coherent state. This provides a novel way to generate single microwave photons [103, 112, 113].

### 4.2.3 The Cross-Kerr Phase Shift

We realize a cross-Kerr interaction between two microwave fields by coupling a superconducting artificial atom (transmon) to a transmission line. As seen in Fig. 3.2, we use two configurations: a transmon in an open transmission line (Sample 1a) [22, 53, 54] and a transmon at the end of a transmission line (Sample 2). Due to the strong coupling between atom and field, we achieve average phase shifts up to 10 and 20 degrees per photon at the single-photon level for Sample 1a and Sample 2, respectively. This is six orders of magnitude larger than in optical systems [114, 115].

From a theoretical point of view, Sample 1a and Sample 2 are essentially the same, with one difference: the emitted field from the atom can propagate in two directions for Sample 1a, but only in one direction for Sample 2. In this way, for Sample 2 all the fields (probe and control) are being reflected. It is beneficial to have all information in the fields going out in a single channel, instead of distributed between two outputs. For both samples, the photon-photon interaction is mediated by the three-level artificial atom. As illustrated in Fig. 2.18, we apply two continuous tones, the probe at  $\omega_p \sim \omega_{10}$  and the control at  $\omega_c = \omega_{21}$ . We observe the induced amplitude and phase shift of the probe as the control tone is turned on and off. The response depends on four different parameters: the powers and the detunings of the probe and the control tones. We study the dependence of the response on these parameters on both Sample 1a and Sample 2.

For Sample 1a,  $t_{p,1}$  and  $r_{p,1}$  measure the *phase coherent* signal. Some of the input signal is *incoherently* transmitted or reflected, such that  $|r_{p,1}|^2 + |t_{p,1}|^2 < 1$ . Importantly, this does *not* necessarily imply any power dissipation in the sample (see Fig. 2.14 and Chapter 2.3.2).

We first characterize the samples with single-tone spectroscopically, which described in Section 4.1.1. Results for Sample 1a and 2 are presented in Fig. 4.2 and Fig. 4.4, respectively. The  $|1\rangle \leftrightarrow |2\rangle$  transition can then be directly measured using 2-tone spectroscopy (see Fig. 4.7A).

We can then explore the two-tone response in more detail. The response of both samples is qualitatively similar, so for clarity, we describe that of Sample 1a in more detail. Fig. 4.13 shows the magnitude (left) and phase (right) of  $t_{p,1}$  for Sample 1a with the control on,  $t_{p,1}^{(\text{on})}$ , and the control off,  $t_{p,1}^{(\text{off})}$ . We can clearly see the formation of the Autler-Townes doublet in  $|t_{p,1}^{(\text{on})}|$  [51, 111]. The doublet states appear as a pair of minima in the black curves of Fig. 4.13A with a separation given by  $\Omega_c$ .

Fig. 4.14A shows the measured amplitude response,  $\Delta t_{p,1}$ , defined as the difference between the magnitude of the probe transmission  $\Delta t_{p,1} = |t_{p,1}^{(\text{on})}| - |t_{p,1}^{(\text{off})}|$ . Fig. 4.14B shows the corresponding phase response,  $\Delta \varphi_{p,1}$ . For these measure-

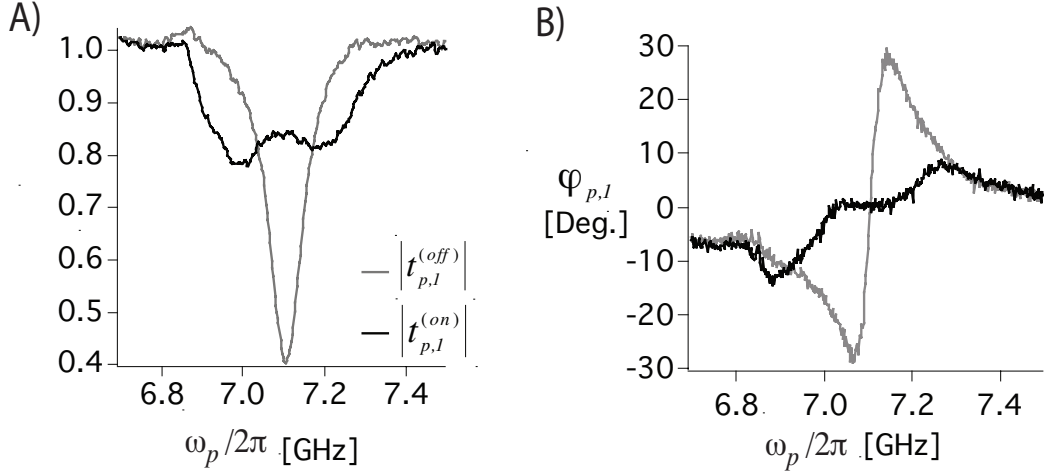


Figure 4.13: Transmission coefficient for the probe, as a function of  $\omega_p$  and control power,  $P_c$ , for low probe powers,  $\Omega_p \ll \gamma_{10}$  in Sample 1a. (A) Measured transmission coefficient with  $P_c = -116$  dBm,  $|t_{p,1}^{(on)}|$  (black), and  $P_c$  turned off,  $|t_{p,1}^{(off)}|$  (grey). (B) corresponding phase response.

ments, we use a weak probe, where  $\Omega_p \ll \gamma_{10}$ . The solid curves in the lower panels are calculated using Eq. (2.94) [51, 83]. This model includes the parameters  $\Gamma_{10}$ ,  $\Gamma_{\phi,10}$  and  $\gamma_{20}$  [51, 83]. The values for these parameters are given in the caption. As expected, the maximum induced amplitude response occurs when the probe is on resonance, and the induced phase response is maximized when the probe is detuned from resonance by an amount  $\delta\omega_p = \omega_p - \omega_{10} \approx 2\pi \times 20$  MHz.

Quantum applications of cross-Kerr media typically require large phase shifts at the single-photon level. Therefore, we now quantify the cross-Kerr phase shift in the limit of low control power [116]. In this limit, the cross-Kerr phase shift is given by Eq. (2.97). To convert this to a phase shift per control photon, we note that the average number of control photons  $\langle N_c \rangle$  per interaction time,  $2\pi/\Gamma_{21}$ , is given by  $\langle N_c \rangle = 2\pi P_c / (\hbar\omega_c\Gamma_{21})$ , so  $\Delta\varphi_p$  is proportional to  $\langle N_c \rangle$ . For reference,  $\langle N_c \rangle = 1$  corresponds to  $P_c = -122$  dBm ( $= 0.64$  fW) and  $\langle N_p \rangle = 1$  corresponds to  $P_p = -124.5$  dBm for Sample 1a. The corresponding numbers for Sample 2 are  $P_c = -123.4$  dBm and  $P_p = -126$  dBm.

Fig. 4.15B shows the probe phase response,  $\Delta\varphi_{p,1}$ , as a function of probe frequency for several very weak probe powers (with a control power of  $P_c = -127$  dBm, i.e.  $\langle N_c \rangle \simeq 0.3$ ). As in Fig. 4.14B, the maximum phase shift occurs at a probe detuning of  $\delta\omega_p/2\pi \approx 20$  MHz. At this point, we measure  $\Delta\varphi_p$  as a function of  $\langle N_c \rangle$ , with the results shown in Fig. 4.15C. For  $\langle N_c \rangle = 1$ , we observe a phase shift of approximately 20 degrees for Sample 2 and 10 degrees for Sample

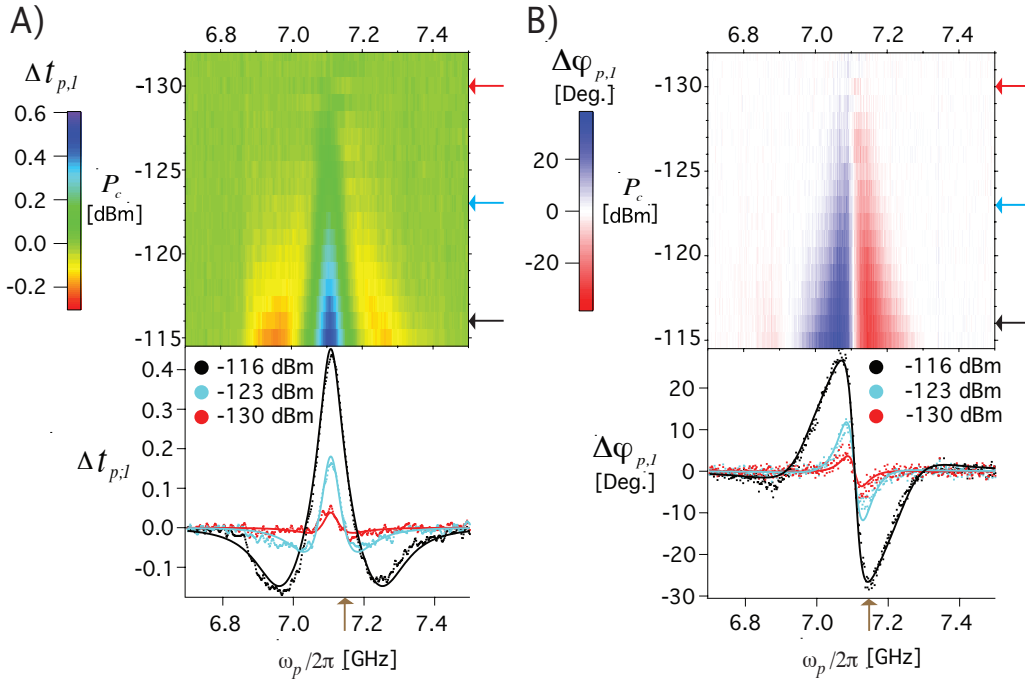


Figure 4.14:  $\Delta t_p$  as a function of  $P_c$  and  $\omega_p$  for low probe powers, where  $\Omega_p \ll \gamma_{10}$  in Sample 1a. (A) Measured amplitude response,  $\Delta t_{p,1}$ . (B) Measured phase response,  $\Delta\varphi_{p,1}$ . Top panels: as a function of probe frequency and control power. Bottom panels: horizontal line cuts (dots) and theory curves (solid lines). Brown arrows show the frequency that maximizes the phase response. The theory curves are fit simultaneously to extract  $\gamma_{20}/2\pi = 150$  MHz along with the control field coupling. The following other parameters, also used in the calculations, are independently measured with single-tone and two-tone spectroscopy:  $\omega_{10}/2\pi = 7.10$  GHz,  $\omega_{21}/2\pi = 6.38$  GHz,  $\Gamma_{10}/2\pi = 74$  MHz,  $\gamma_{10}/2\pi = 60$  MHz and the probe field coupling.

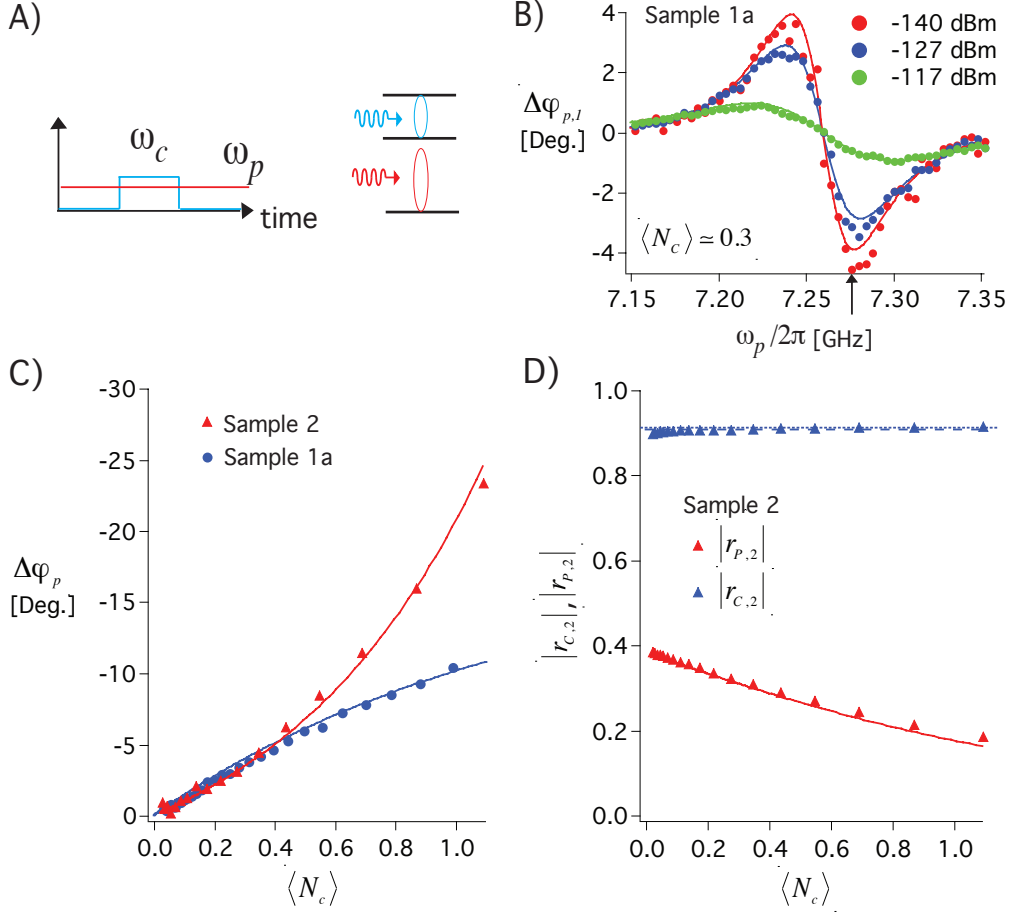


Figure 4.15: Probe phase shift,  $\Delta\varphi_p$ , induced by a weak control pulse. Solid curves are theoretical fits to the data, according to Appendix F. The fitting parameters for each Sample are  $\gamma_{20}$  and the control field coupling. Other parameters are measured independently through spectroscopy. All parameters are listed in Table 4.2. (A) The control pulse induces a phase shift,  $\Delta\varphi_p$ , of the continuous probe in the time domain. The length of the pulse is  $1 \mu\text{s}$  for Sample 1a and  $7 \mu\text{s}$  for Sample 2. (B)  $\Delta\varphi_p$  as a function of  $\omega_p$  for three different probe powers and  $\langle N_c \rangle \simeq 0.3$ , for Sample 1a. Note that here the  $|0\rangle \leftrightarrow |1\rangle$  transition is 7.26 GHz (due to a different external magnetic flux,  $\Phi$ ). (C)  $\Delta\varphi_p$  as a function of  $\langle N_c \rangle$  for a weak probe at a probe frequency that maximizes the probe phase shift. Each data point is an average over 2 million control pulses. An average phase shift of 10 degrees per control photon is observed in Sample 1a, and 20 degrees per control photon in Sample 2. (D)  $|r_{p,2}|$  and  $|r_{c,2}|$  as a function of  $\langle N_c \rangle$ . The dashed blue line indicates  $|r_{c,2}| = 0.9$ . Extensive measurements of  $r_{p,2}$  are presented in Fig. 4.8.

-	Spectroscopic						Kerr
Sample	$E_J/h$	$E_C/h$	$\omega_{10}/2\pi$	$\omega_{21}/2\pi$	$\Gamma_{10}/2\pi$	$\Gamma_{\phi,10}/2\pi$	$\gamma_{20}/2\pi$
1a	13.1	0.59	7.26	6.54	0.074	0.020	0.160
2	11.99	0.42	5.916	5.50	0.063	0.015	0.093

-	Derived				
Sample	$\Gamma_{21}/2\pi$	$\gamma_{10}/2\pi$	$E_J/E_C$	$\delta\omega_p/2\pi$	$ \Delta\varphi_p/\langle N_c \rangle $
1a	0.148	0.057	22.2	0.02	$10^\circ$
2	0.126	0.047	28.5	0.009	$20^\circ$

Table 4.2: Parameters for Sample 1a, 2. The first six parameters, labelled ‘‘Spectroscopic’’, are determined from single-tone and two-tone spectroscopy. The parameter  $\gamma_{20}$  is extracted from fitting the Kerr data in Fig. 4.15. These 7 parameters are used to derive the remaining quantities. All dimensional quantities are in GHz. Note that some parameters for Sample 1a are different than in Fig. 4.14 because the device was operated at a different flux bias.

1a<sup>1</sup>.

To further characterize the response of Sample 2, Fig. 4.15D shows the corresponding magnitudes  $|r_{p,2}|$  and  $|r_{c,2}|$  as a function of  $\langle N_c \rangle$ . The dependence of  $|r_{p,2}|$  and  $|r_{c,2}|$  on  $\langle N_c \rangle$  can be understood in terms of dephasing. In Fig. 4.15D, for a fixed  $\delta\omega_p/2\pi \approx 9$  MHz, the low control-power limit of  $|r_{p,2}| \approx 0.4$  is determined by  $\Gamma_{\phi,10}$  and  $\Gamma_{10}$ , inferred by Eq. (2.80). As  $\langle N_c \rangle$  increases, we see that  $|r_{p,2}|$  decreases. This effect is due to the power broadening of the linewidth of state  $|1\rangle$  induced by the control tone, which effectively increases the dephasing rate. Therefore, with phase-sensitive detection, the coherent signal  $|r_{p,2}|$  becomes weaker as  $\langle N_c \rangle$  increases. We also see  $|r_{c,2}| \sim 0.90$  is relatively constant, though it increases to unity as the transition saturates at high power,  $\Omega_c \gg \gamma_{21}$ . With a weak probe,  $\Omega_p \ll \gamma_{10}$ , there is a low probability of the atom being in the first excited state. As a result, the probability of the atom scattering a control photon is very low, and the dephasing is small. Note that the reduction of  $|r_{p,2}|$  in Fig. 4.15D is not due to dissipation but instead due to a loss of phase coherence in the signal. Indeed, both  $\langle N_c \rangle$  and  $\langle N_p \rangle$  are *conserved*, which has been confirmed in Fig. 4.3.

We have demonstrated a Kerr medium working in the semiclassical regime

<sup>1</sup>We comment that there is a systematic uncertainty, of order 20%, in the calibration of  $\langle N_c \rangle$  for Sample 1a in Fig. 4.15C. For small probe and control powers, the parameters  $\gamma_{20}$  and  $\Omega_c$  cannot be determined independently with high precision. At high control powers, the resolved Autler-Townes splitting enables an independent calibration of  $\Omega_c$ . This high-power calibration was unfortunately not repeated for Sample 1a for the flux-bias point in Fig. 4.15. It was, however, done for Sample 2.

(see the Hamiltonian in Eq. (2.81)), showing good performance and good agreement with theory. Cross-Kerr media have long been proposed for quantum applications such as the QND measurement of photon number [117]. Therefore, it is interesting to estimate what the performance of the device would be in this application. To achieve QND photon counting, the phase shift of the probe produced by a single photon in the control mode (i.e. the *signal*) must be resolved above the probe phase noise, that is, the signal-to-noise ratio (SNR) should be greater than 1. Following the approach of Ref. [92], we calculate the optimum SNR using the parameters of Sample 2. We consider also whether the performance is enhanced by exchanging the role of probe and control. In fact, we find this arrangement ( $\omega_p \approx \omega_{21}$  and  $\omega_c \approx \omega_{10}$ ) to be best, giving a SNR of 0.38 measuring a single-photon Fock state and assuming the only noise is vacuum noise. (With the probe and control as in Fig. 4.15A, the SNR is about a factor of 2 lower.) However, as discussed in Chapter 2.4.3, due to a subtle interplay between transmon saturation and vacuum noise, the probe phase noise for a single transmon *always* dominates the cross-Kerr induced phase shift, and it is found that  $\text{SNR} \lesssim 0.6$  under very general assumptions (see Fig. 2.21). Thus, our device is quite close to the theoretical optimum for cross-Kerr phase shifts. It, therefore, potentially offers an important platform on which to test proposals for cross-Kerr based protocols.

In conclusion, we have investigated the nonlinear interaction between two microwave fields at the single-photon level induced by a three-level superconducting transmon. In particular, we observed an average cross-Kerr phase shift of 20 degrees per photon between two coherent microwave fields. Compared to cavity-based systems [118], this system has the advantage of being tunable *in-situ* over a wide range of frequencies. Such giant Kerr phase shifts may find applications in quantum information applications.

# Chapter 5

## Conclusion and Future Work

In this thesis, we have investigated both fundamental and applied aspects of how propagating microwave photons interact with an artificial atom in the form of a superconducting transmon qubit.

A three-level artificial atom, a superconducting transmon type qubit, in a 1D open space was designed and fabricated. We investigated the following quantum-optical effects. We observed extinction of up to 99% of the forward propagating microwave power and measured the elastic and inelastic scattering by the artificial atom. We observed the strong nonlinearity of this artificial atom. By applying a strong driving tone, we observed the Mollow Triplet. By applying a second control tone, we observed Autler-Townes splitting and the giant cross-Kerr effect.

We further developed the following key elements for controlling and creating propagating photons based on the observed quantum-optical effects. By using the Autler-Townes splitting, we demonstrated a single-photon router, which can route quantum information on nanosecond timescales with 91% efficiency and the possibility of multiple outputs. By utilizing the strong nonlinearity of this artificial atom, we demonstrated a photon-number filter, which can generate flying microwave photons. Using the cross-Kerr effect, we demonstrated strong photon-photon interaction at the single-photon level.

### Future work

There is a lot of interesting future work to be done with our system. We will illustrate some ideas in this section. From the application point of view, tunable coupling is very beneficial for a quantum network. For example, we want to generate quantum information (photons) at an adjustable rate. Fig. 5.1A shows the micrograph of a tunable-coupling qubit embedded in a 1D open transmission line. The tunable-coupling qubit is two strongly coupled transmons [119, 120]. The tunability is achieved by tuning on resonance or off-resonance with these two

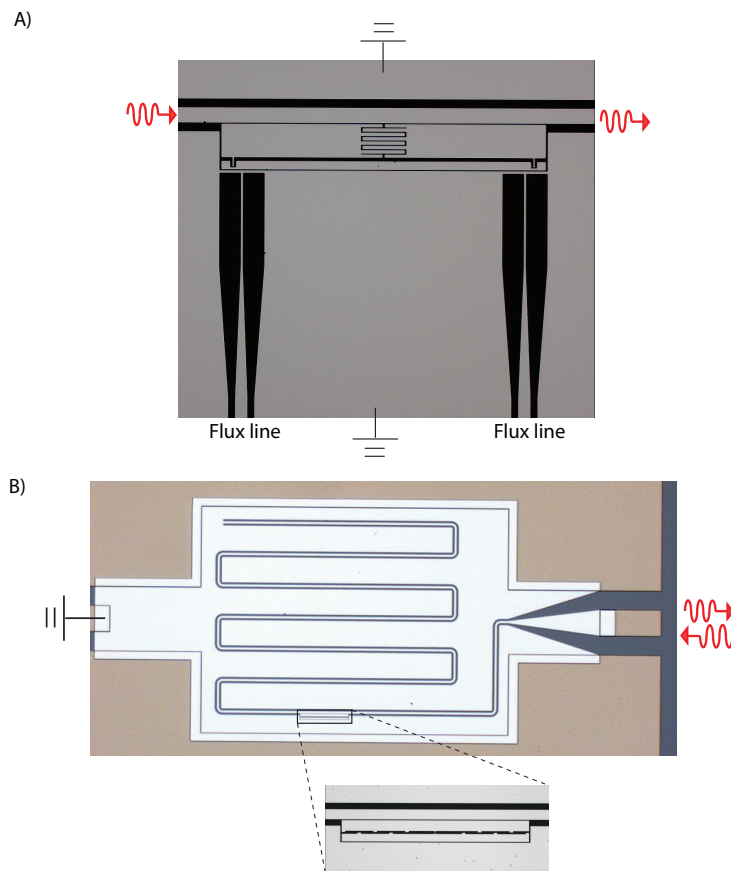


Figure 5.1: Micrograph of tunable-coupling samples. A) Tunable-coupling qubit coupled to an open transmission line. The dc current which passes through the on-chip flux line is used to tune the dipole moment of the tunable-coupling qubit. B) Atom in front of a mirror. The relaxation rate of the atom can be tuned by the transition wavelength of the atom.

transmons by on-chip flux lines. This creates either cancellation or enhancement of the dipole moment of the coupled atoms [119, 120]. We can also embed the tunable coupling qubit at the end of a transmission line. This would be a better scheme for a single photon source, since all the field will be emitted in one direction.

Another approach of tunable coupling is as follows. Instead of tuning the dipole moment of the atom, we change the EM field structure experienced by the atom. Fig. 5.1B shows a micrograph of a sample fabricated for that purpose. In this system, we introduce a perfect mirror, *i.e.* ground. The relaxation (coupling) rate of the atom can be tuned by the distance between the mirror (ground) and the atom [91]. In other words, if the atom stays at the antinode, it experience

---

maximum coupling. Whereas, if the atom stays at the node, there is no coupling. Or equivalently, the coupling can be tuned by the transition wavelength of the atom (effective distance) by flux through the SQUID loop.

Entanglement is also a unique resource in quantum applications. We can create entangled atoms in the following scheme. In Fig. 5.2A, we see a transmission line terminated with a tunable boundary condition (SQUID) [41]. We can also embed two atoms in the system. As shown in ref [37], two-mode squeezed pairs of photons will be generated by moving the boundary condition very fast using the flux pumping line, the so-called dynamical Casimir effect. If these two entangled photons are on resonance with the two artificial atoms, respectively, these two atoms become entangled. In addition, with the same sample, we can also investigate the influence of the atom driven by a coherent squeezed vacuum [121]. This state can be generated by pumping the SQUID.

As I have shown in my thesis, a two-level atom acts as a mirror for a weak resonant field. We can embed two atoms at a distance of half the transition wavelength, as shown in Fig. 5.2B. With a weak resonance field, the two atoms form a cavity. We can probe the cavity with the probe line, which is coupled to the transmission line at the antinode.

In Fig. 5.2C, by fabricating a periodic array of atoms in the 1D waveguide, we expect to see photonic band gap structures [122].

In addition, we can investigate an atom in an open waveguide coupled to other degree of freedom, such as surface acoustic waves. In this scheme, we can couple the superconducting atom with propagating phonons, as proposed in [123]. It creates a new platform to investigate and engineer phonons in the quantum regime.

Finally, the development of a hybrid quantum network in Fig. 1.5 would combine both advantages of superconducting circuits and optical photons. The early stages of an optical-microwave interface have been demonstrated [124, 125, 126, 127].

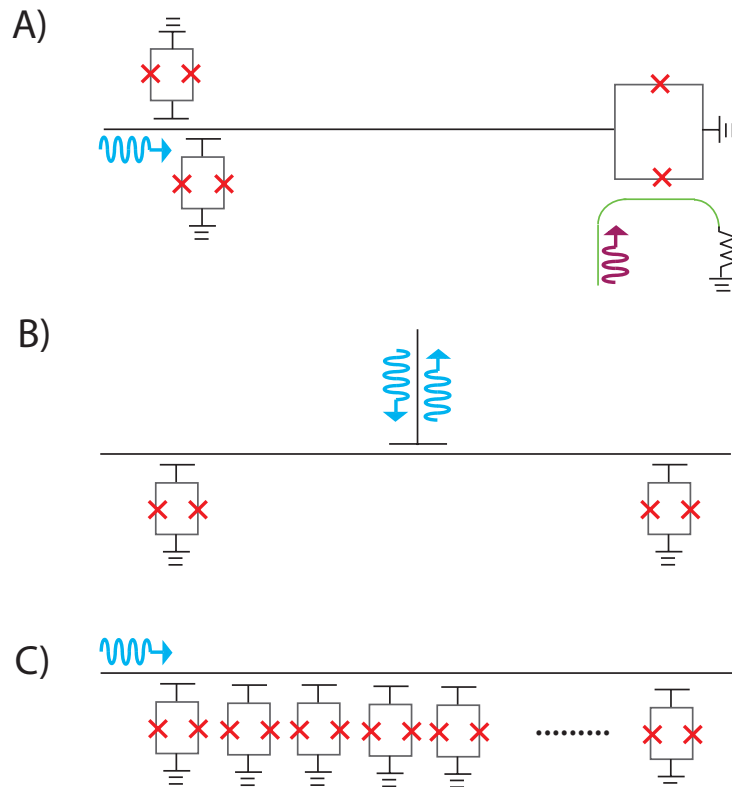


Figure 5.2: Proposed future work in quantum optics with propagating microwaves. A) Dynamical Casimir sample with two superconducting atoms. The green curve represent the fast flux pumping line terminated with a 50 ohm resistor. The purple microwave represents the pump tone. B) The two atoms coupled to the same open transmission line with a separation of half a wavelength. With a weak probe, the two atoms form a cavity. The probe line is coupled to the transmission line at the antinode of the atomic cavity. C) Periodic array of atoms in a 1D waveguide, each atom separated by a distance  $l$ .



---

# Appendix A

## Symbols & Abbreviations

### Abbreviations

QC	Quantum Computer
SC	Superconductivity
TL	Transmission line
CW	Continous wave
EIT	Electromagnetically Induced Transparency
ATS	Autler-Townes Splitting
HWHM	Half-width-at-half maximum
AWG	Arbitrary waveform generator
EM	Electromagnetic
1D/3D	One dimension/Three dimensions
CPW	Coplanar waveguide
TEM	Transverse Electromagnetic
RBW	Resolution bandwidth
BW	Bandwidth
LNA	Low noise amplifier
SQUID	Superconducting quantum interference device
PCB	Printed circuit board
SCB	Single-Cooper-pair box
QED	Quantum electrodynamics
QND	Quantum nondemolition
MW	Microwave
RF	Radio frequency
SNR	Signal-to-noise ratio
$N_f$	Noise factor
RWA	Rotating wave approximation
Al, Au	Aluminum, gold
IVC	Inner vacuum chamber
GZ	Gardiner Zoller, Quantum Noise [84]
dc	Direct current
ac	Alternating current

## Constants

$e$	Electron charge
$\hbar$	Planck constant
$k_B$	Boltzmann constant
$c$	Velocity of the light in vacuum
$\Phi_0$	Magnetic flux quantum ( $h/2e$ )
$R_k$	Quantum resistance ( $h/e^2$ )
$a_0$	Bohr radius

## Artificial Atom

$ 0\rangle,  1\rangle,  2\rangle$	Ground state, first and second excited state
$E_m$	Energy of level $m$
$\omega_{ij}$	Resonance frequency of the i-j transition
$\omega_p, \omega_c, \omega_{pump}$	Probe frequency, control frequency and Pump frequency
$\delta\omega_p, \delta\omega_c$	Probe, control detuning ( $\delta\omega_p = \omega_p - \omega_{ij}$ , $\delta\omega_c = \omega_c - \omega_{jk}$ )
$\Gamma_{ij}, \Gamma_{\phi,ij}$	Relaxation rate, pure dephasing rate of the i-j transition
$\Gamma_l$	Loss rate
$\gamma_{ij}$	Decoherence rate of the i-j transition
$\Omega_p, \Omega_c$	Rabi frequency of probe field and control field
$d$	Electric dipole moment
$\varepsilon_m$	Charge dispersion
$\alpha_n, \alpha_r$	Anharmonicity, where $\alpha_r = \alpha_n/E_{10}$
$R_n$	Resistance of transmon test structure
$\mathbb{P}, \zeta$	Polarization and polarizability

## General qubit

$T_1, T_2$	Relaxation time, decoherence time
$\Gamma_1, \Gamma_2$	Relaxation rate, decoherence rate
$\Gamma_+, \Gamma_-$	Absorption rate, emission rate
$\omega_x, \omega_y, \omega_z$	Rotation frequency around x,y,z axis of the Bloch sphere
$\sigma_x, \sigma_y, \sigma_z$	Pauli spin matrices
$\sigma_+, \sigma_-$	Qubit raising and lowering operator
$ \Psi\rangle$	Wave function
$\mathbb{I}, \rho$	Identity matrix and density matrix
$\rho_{ij}$	The i-j element of the density matrix
$\mu_{01}$	Magnetic dipole moment
$\theta$	Angles of state relative to z axis of the Bloch sphere
$\varphi$	Angles of state on x-y plane of the Bloch sphere
$u_i$	A vector on or inside the Bloch sphere. $\langle\sigma_i\rangle = u_i$
$\mathbb{R}$	Operation on states
$S_{\perp}(\omega_z)$	Spectral density perpendicular to the z axis
$S_z(\omega \simeq 0)$	Spectral density along the z axis
$\Theta$	Thermal equilibrium temperature

## SC circuit

$E_c, E_J, E_L$	Charging energy, Josephson energy and inductive energy
$E_{ch}, E_Q$	Electrostatic energy, Cooper-pair charging energy( $4E_c$ )
$C, L, Z$	Capacitance, inductance and characteristics impedance
$C_c, C_g$	Coupling capacitance and gate capacitance
$C_\Sigma, \beta$	Total capacitance and coupling coefficient ( $C_c/C_\Sigma$ )
$C_J, C_s, C_{JS}$	Junction capacitance, shunt capacitance and their sum
$C_0, L_0$	Capacitance, inductance per unit length
$G_0, R_0$	Shunt conductance, series resistance per unit length
$Z_0$	Characteristic impedance of TL ( $50 \Omega$ )
$Z_{atom}$	Impedance of the artificial atom (classical circuit)
$L_s$	SQUID inductance

## Circuit analysis

$H, \mathcal{H}, \mathcal{L}$	Classical/Quantum Hamiltonian and Lagrangian
$\hat{n}$	Number operator for Cooper pairs
$V_g, n_g$	Gate voltage and normalized gate charge
$Q, \Phi, \Phi_{ext}$	Charge, magnetic flux, applied external flux
$\phi, p$	Generalized phase, generalized charge
$\tau_{RC}$	Characteristics time constant of the SCB-TL circuit
$V_{\mu\omega}$	MW voltage drive
$A, A'$	MW amplitude and normalized MW amplitude
$\phi_{R/L}^{in/out}$	Generalized phase input (output) from the Right (Left)
$V^+, I^+$	Voltage/current wave in forward direction
$V^-, I^-$	Voltage/current wave in backward direction
$\vartheta$	Phase of reflection coefficient
$V_{in}, V_R, V_T$	Incident, reflected and transmitted voltage field
$t, r$	Complex transmission and reflection coefficient
$r_0$	Maximum reflection of atom in open transmission line
$t_{p,i}, r_{p,i}$	$t$ or $r$ of the probe field for Sample $i$
$t_{c,i}, r_{c,i}$	$t$ or $r$ of the control field for Sample $i$
$\varphi_{p,i}$	Probe phase for Sample $i$
$\Delta\varphi_{p,i}$	Probe phase shift for Sample $i$
$T, R$	Transmittance, reflectance
$T_{p,i}, R_{p,i}$	Transmittance or reflectance of the probe for Sample $i$
$R_b$	Background reflection in power
$P_p, P_c$	Incident power of probe and control field
$P_N$	Noise power
$\langle N_p \rangle$	Average number of probe photons per relaxation time
$\langle N_c \rangle$	Average number of control photons per relaxation time
$K$	Kerr coefficient
$v$	Velocity of the waves in the TL
$\xi$	Propagation constant in the TL

**SC**

$I_c$	Critical current
$B$	Magnetic flux density
$\Delta_s$	Superconducting gap energy
$\Lambda$	Parameter describing the asymmetry of the SQUID

**Others**

$a^\dagger, a$	Creation and annihilation operator
$ \alpha\rangle, \alpha$	Coherent state and its amplitude
$ \beta_T\rangle$	Thermal state
$ N\rangle$	Photon number state $N$
$\langle N \rangle$	Average photon number
$P(N)$	Probability of photon number state $N$
$g^{(2)}$	Second order correlation function
$\tau$	Delay time between two paths
$g$	Qubit-photon coupling strength
$U$	Potential energy
$m$	Mass of a particle
$\omega_m$	Mechanical resonance frequency
$x, p_m$	Position and momentum of a particle
$T_N$	Noise temperature
$T_m$	Measurement time
$G_i$	Gain of amplifier $i$
$F_i^\dagger, F_i$	Creation and annihilation noise operator of amplifier $i$
$b_i^\dagger, b_i$	Creation and annihilation operator after amplifier $i$
$\varepsilon_r$	Relative dielectric constant
$W$	Width of pulse
$k_c, k_p$	Coupling constant, $\Omega_i = k_i \times 10^{P_i/20}$ , where $P_i$ is given in dBm
$k_n$	Number of emission channels for the transmon

# Appendix B

## Three-level Rotating-Wave Approximation

This section follows the derivation in reference [128]. The Hamiltonian of a three-level atom can be written as

$$H_{atom} = \begin{pmatrix} E_0 & 0 & 0 \\ 0 & E_1 & 0 \\ 0 & 0 & E_2 \end{pmatrix}. \quad (1)$$

The probe field with angular frequency  $\omega_p$  and amplitude  $A_p$  couples to the 0-1 transition with the dipole moment  $d_{01}$ . In addition, the control field with angular frequency  $\omega_c$  and amplitude  $A_c$  couples to the 1-2 transition with the dipole moment  $d_{12}$ . The coupling Hamiltonian can be written as,

$$H_{drive} = A_p \cos \omega_p t \begin{pmatrix} 0 & d_{01} & 0 \\ d_{10} & 0 & 0 \\ 0 & 0 & 0 \end{pmatrix} + A_c \cos \omega_c t \begin{pmatrix} 0 & 0 & 0 \\ 0 & 0 & d_{12} \\ 0 & d_{21} & 0 \end{pmatrix}, \quad (2)$$

where  $\hbar\omega_{10} = E_1 - E_0$  and  $\hbar\omega_{21} = E_2 - E_1$ . The total Hamiltonian is then

$$H = H_{atom} + H_{drive}. \quad (3)$$

The time evolution of the state vector  $\Psi$  obeys

$$H\Psi = i\hbar\partial_t\Psi, \quad (4)$$

where  $\Psi = c_0 |0\rangle + c_1 |1\rangle + c_2 |2\rangle$ . We can rewrite this expression in the following form,

$$\begin{pmatrix} H_{00} & H_{01} & H_{02} \\ H_{10} & H_{11} & H_{12} \\ H_{20} & H_{21} & H_{22} \end{pmatrix} \begin{pmatrix} c_0 \\ c_1 \\ c_2 \end{pmatrix} = i\hbar \begin{pmatrix} \partial_t c_0 \\ \partial_t c_1 \\ \partial_t c_2 \end{pmatrix}; \quad (5)$$

$$i\hbar\partial_t c_0 = H_{00}c_0 + H_{01}c_1 + H_{02}c_2; \quad (6)$$

$$i\hbar\partial_t c_1 = H_{10}c_0 + H_{11}c_1 + H_{12}c_2; \quad (7)$$

$$i\hbar\partial_t c_2 = H_{20}c_0 + H_{21}c_1 + H_{22}c_2. \quad (8)$$

Considering the time dependent transformation, we have

$$\tilde{c}_i = e^{i\phi_i(t)} c_i, \quad (9)$$

where  $i = 0, 1, 2$ . The state vector becomes

$$\tilde{\Psi} = \tilde{c}_0 |0\rangle + \tilde{c}_1 |1\rangle + \tilde{c}_2 |2\rangle, \quad (10)$$

which are the solutions of

$$\tilde{H}\tilde{\Psi} = i\hbar\partial_t\tilde{\Psi}. \quad (11)$$

From Eq. (9), Eq. (6), we have

$$i\hbar\partial_t\tilde{c}_0 = i\hbar e^{i\phi_0}\partial_t c_0 - \hbar\partial_t\phi_0 c_0 e^{i\phi_0} \quad (12)$$

$$= (H_{00} - \hbar\partial_t\phi_0)\tilde{c}_0 + H_{01}e^{i(\phi_0-\phi_1)}\tilde{c}_1 + H_{02}e^{i(\phi_0-\phi_2)}\tilde{c}_2 \quad (13)$$

$$\tilde{H}_{00} = H_{00} - \hbar\partial_t\phi_0; \tilde{H}_{01} = H_{01}e^{i(\phi_0-\phi_1)}; \tilde{H}_{02} = H_{02}e^{i(\phi_0-\phi_2)}. \quad (14)$$

Using the same procedure for  $\tilde{c}_1$  and  $\tilde{c}_2$ , we get

$$\tilde{H}_{10} = H_{10}e^{i(\phi_1-\phi_0)}; \tilde{H}_{11} = H_{11} - \hbar\partial_t\phi_1; \tilde{H}_{12} = H_{12}e^{i(\phi_1-\phi_2)}; \quad (15)$$

$$\tilde{H}_{20} = H_{20}e^{i(\phi_2-\phi_0)}; \tilde{H}_{21} = H_{21}e^{i(\phi_2-\phi_1)}; \tilde{H}_{22} = H_{22} - \hbar\partial_t\phi_2. \quad (16)$$

We can rewrite (14), (15), (16) in the matrix form,

$$\tilde{H} = \begin{pmatrix} H_{00} - \hbar\partial_t\phi_0 & H_{01}e^{i\phi_{01}} & H_{02}e^{i\phi_{02}} \\ H_{10}e^{i\phi_{10}} & H_{11} - \hbar\partial_t\phi_1 & H_{12}e^{i\phi_{12}} \\ H_{20}e^{i\phi_{20}} & H_{21}e^{i\phi_{21}} & H_{22} - \hbar\partial_t\phi_2 \end{pmatrix}, \quad (17)$$

where  $e^{i\phi_{kj}} = e^{i(\phi_k-\phi_j)}$ ,  $k, j = 0, 1, 2$ . We choose  $\phi_0 = E_0t/\hbar$ ,  $\phi_1 = (E_0/\hbar + \omega_p)t$ ,  $\phi_2 = (E_0/\hbar + \omega_c + \omega_p)t$ . From Eq. (14), (15) and (16), we then have,

$$\tilde{H}_{00} = E_0 - E_0 = 0; \quad (18)$$

$$\tilde{H}_{01} = A_p \cos\omega_p t d_{01} e^{-i\omega_p t} = \frac{1}{2} A_p d_{10} (1 + e^{-2i\omega_p t}); \quad (19)$$

$$\tilde{H}_{02} = \tilde{H}_{20} = 0; \quad (20)$$

$$\tilde{H}_{11} = E_1 - (E_0 + \hbar\omega_p) = \hbar(\omega_{10} - \omega_p); \quad (21)$$

$$\tilde{H}_{12} = \frac{1}{2} A_p d_{12} (1 + e^{-2i\omega_p t}); \quad (22)$$

$$\tilde{H}_{22} = \hbar(\omega_{10} + \omega_{21}) - \hbar(\omega_p + \omega_c). \quad (23)$$

Next, we define the two Rabi frequencies for the transitions,

$$\hbar\Omega_p = -A_p d_{10}; \hbar\Omega_c = -A_c d_{12}, \quad (24)$$

and the detunings,

$$\delta\omega_p = \omega_p - \omega_{10}; \delta\omega_c = \omega_c - \omega_{21}.$$

From Eq. (18) to Eq. (23), we can derive

$$\tilde{H} = -\frac{\hbar}{2} \begin{pmatrix} 0 & \Omega_p & 0 \\ \Omega_p & 2\delta\omega_p & \Omega_c \\ 0 & \Omega_c & 2(\delta\omega_p + \delta\omega_c) \end{pmatrix} - \frac{\hbar}{2} \begin{pmatrix} 0 & \Omega_p e^{-2i\omega_p t} & 0 \\ \Omega_p e^{2i\omega_p t} & 0 & \Omega_c e^{-2i\omega_c t} \\ 0 & \Omega_c e^{2i\omega_c t} & 0 \end{pmatrix}.$$

Finally, we make the rotating wave approximation, where we ignore fast rotating terms containing  $2\omega_p$  and  $2\omega_c$ . This means that the second term can be neglected, since it only contains these high frequency components. Thus we get the following Hamiltonian

$$\tilde{H} = -\frac{\hbar}{2} \begin{pmatrix} 0 & \Omega_p & 0 \\ \Omega_p & 2\delta\omega_p & \Omega_c \\ 0 & \Omega_c & 2(\delta\omega_p + \delta\omega_c) \end{pmatrix}. \quad (25)$$

# Appendix C

## Deviation of $t$ and $r$ in Section 2.3.2

This appendix follows reference [83] in append paper V. We start by writing down the Lagrangian and Hamiltonian of SCB  $\mathcal{L}_{SCB}$ ,  $H_{SCB}$  in terms of the generalized velocities  $\dot{\phi}_0$ ,  $\dot{\phi}_J$ , and the generalized position  $\phi_0$ ,  $\phi_J$ ,

$$\mathcal{L}_{SCB} = \frac{1}{2}C_c(\dot{\phi}_0 - \dot{\phi}_J)^2 + C_c\dot{\phi}_J^2 + E_J \cos\left(\frac{2e}{\hbar}\phi_J\right); \quad (26)$$

$$H_{SCB} = \frac{1}{2}C_c(\dot{\phi}_0 - \dot{\phi}_J)^2 + C_c\dot{\phi}_J^2 - E_J \cos\left(\frac{2e}{\hbar}\phi_J\right). \quad (27)$$

The generalized momentum represents the charge and is given by the derivative of the  $\mathcal{L}_{SCB}$  in Eq. (26), with respect to the corresponding generalized velocities, we have the following relations,

$$p_0 = \frac{\partial \mathcal{L}_{SCB}}{\partial \dot{\phi}_0} = C_c(\dot{\phi}_0 - \dot{\phi}_J); p_J = \frac{\partial \mathcal{L}_{SCB}}{\partial \dot{\phi}_J} = (C_c + C_J)\dot{\phi}_J - C_c\dot{\phi}_0. \quad (28)$$

To get the SCB Hamiltonian in terms of charge  $p$ , we need to write  $\dot{\phi}_0$  and  $\dot{\phi}_J$  in terms of  $p_J$  and  $p_0$ . From (28), we have

$$\dot{\phi}_0 = \frac{p_J + p_0}{C_J} + \frac{p_0}{C_c}; \quad \dot{\phi}_J = \frac{p_J + p_0}{C_J}. \quad (29)$$

If we substitute Eq. (29) into Eq. (27), we have

$$H_{SCB} = \frac{p_0^2}{2C_c} + \frac{(p_J + p_0)^2}{2C_J} - E_J \cos\left(\frac{2e}{\hbar}\phi_J\right). \quad (30)$$

The total Hamiltonian of the system (Fig. 2.12A) is the sum of the Hamiltonian of the transmission line and SCB in Eq. (30),

$$H = \int_{x \neq 0} dx \left( \frac{p(x, t)^2}{2C_0} + \frac{1}{2L_0} \left( \frac{\partial \phi(x, t)}{\partial x} \right)^2 \right) + H_{SCB}. \quad (31)$$

At  $x = 0$ , the total left (right) phase is the sum of left (right) input phase and left (right) output phase, we can write it in the following way,

$$\phi(0) = \phi_L^{in} + \phi_L^{out} = \phi_R^{in} + \phi_R^{out}. \quad (32)$$

From the expressions in Eq. (32) and by introducing a DC voltage bias to the microwave field, we can rewrite  $\phi_0 = V_{DC}t + (\phi^{in} + \phi^{out})/2$ . This leads to

$$\partial_t \phi_0 = V_{DC} + \partial_t(\phi^{in} + \phi^{out})/2. \quad (33)$$

From Eq. (28), (29) and Eq. (33), we can rewrite

$$p_0 = \frac{C_c C_J}{C_c + C_J} [V_{DC} + \partial_t(\phi^{in} + \phi^{out})/2] - p_J \frac{C_c}{C_c + C_J}. \quad (34)$$

From Eq. (29) and Eq. (34), we have

$$\partial_t \phi_J = \frac{p_J + C_c [V_{DC} + \partial_t(\phi^{in} + \phi^{out})/2]}{C_c + C_J}. \quad (35)$$

With the Hamiltonian in Eq. (31), we get the corresponding Lagrangian  $\mathcal{L}$ . The equation of motion therefore becomes,

$$\dot{p}_J = -\frac{\partial \mathcal{L}}{\partial \phi_J} = -E_J \frac{2e}{\hbar} \sin\left(\frac{2e}{\hbar} \phi_J\right); \quad (36)$$

$$\dot{p}_0 = -\frac{\partial \mathcal{L}}{\partial \phi_0}; \quad \frac{\partial p_0}{\partial t} = \frac{1}{L_0} (\partial_x \phi(0^+) - \partial_x \phi(0^-)) = I_{in} - I_{out}. \quad (37)$$

Since the current is voltage divided by the impedance and the voltage is the time derivative of the phase, from Eq. (37), we have

$$\frac{\partial p_0}{\partial t} = \frac{\partial_t(\phi^{in} - \phi^{out})}{Z_0}, \quad (38)$$

which can be rewritten as,

$$\partial_t \phi^{out} = \partial_t \phi^{in} - Z_0 \partial_t p_0. \quad (39)$$

If we put (34) into (39), the output/input field equation becomes,

$$\partial_t \phi^{out} = \partial_t \phi^{in} + Z_0 \partial_t p_J \frac{C_c}{C_c + C_J} - \frac{C_c C_J Z_0}{2(C_c + C_J)} [\partial_t^2(\phi^{in} + \phi^{out})]. \quad (40)$$

We define the characteristic time constant,

$$\tau_{RC} = \frac{C_c C_J Z_0}{2(C_c + C_J)}. \quad (41)$$

Then, Eq. (40) becomes

$$\partial_t \phi^{out} = \partial_t (\phi^{in} + 2p_J \frac{\tau_{RC}}{C_J}) - \tau_{RC} [\partial_t^2 (\phi^{in} + \phi^{out})]. \quad (42)$$

Eq. (42) can be recognized as a recursive equation for  $\partial_t (\phi^{in} + \phi^{out})$ . By adding  $\partial_t \phi^{in}$  in both sides, and recursively filling in  $\partial_t (\phi^{in} + \phi^{out})$  at the end, a series expansion is obtained,

$$\frac{\partial_t (\phi^{in} + \phi^{out})}{2} = (\partial_t - \tau_{RC}^2 \partial_t^2 + \dots)(\phi^{in} + p_J \frac{\tau_{RC}}{C_J}). \quad (43)$$

For  $Z_0 \simeq 50 \Omega$ ,  $C_c \sim C_J \sim 25$  fF, we find  $1/\tau_{RC} \sim 1$  THz, around 20 times higher than the relevant frequency of  $\phi^{in}$  and  $p_J$ , which is set by the qubit frequency  $2\pi \times 7.5$  GHz  $\sim 50$  GHz. For our current sample, we can limit ourselves to the lowest order approximation and ignore the higher orders, Eq. (42) becomes

$$\phi^{out} = \phi^{in} + 2p_J \frac{\tau_{RC}}{C_J}. \quad (44)$$

Substituting Eq. (44) into Eq. (35), we have

$$\partial_t \phi_J = \frac{C_c V_{DC} + p_J}{C_c + C_J} + \frac{C_c \tau_{RC}}{C_J (C_J + C_c)} \partial_t p_J + \frac{C_c}{C_c + C_J} \partial_t \phi^{in}(t). \quad (45)$$

From Eq. (29), we get

$$p_0 = \frac{C_c (C_J V_0 - p_J)}{C_c + C_J}, \quad (46)$$

where  $V_0 = \dot{\phi}_0$ . Putting Eq. (46) into Eq. (30), we get

$$H_{SCB} = \frac{(C_c V_0 + p_J)^2}{2(C_c + C_J)} - E_J \cos \left( \frac{2e}{\hbar} \phi_J \right). \quad (47)$$

In summary, we get three important equations/Hamiltonian, from Eq. (44), (45), (47),

$$\partial_t \phi_J = \frac{C_c V_{DC} + p_J}{C_c + C_J} + \frac{C_c \tau_{RC}}{C_J (C_J + C_c)} \partial_t p_J + \frac{C_c}{C_c + C_J} \partial_t \phi^{in}(t); \quad (48)$$

$$\phi^{out} = \phi^{in} + 2p_J \frac{\tau_{RC}}{C_J}; \quad \phi_{R/L}^{out} = \phi_{L/R}^{in} + p_J \frac{\tau_{RC}}{C_J}, \quad (49)$$

$$H_{SCB} = \frac{(C_c V_0 + p_J)^2}{2(C_c + C_J)} - E_J \cos \left( \frac{2e}{\hbar} \phi_J \right). \quad (50)$$

Eq. (48) relates the time derivative of Josephson junction phase in terms of circuit

parameters, the time derivative of Josephson junction charge and time derivative of input field. Eq. (49) relates the output field in terms of input fields, Josephson junction charge and circuit parameters. Eq. (50) is the simplified Hamiltonian of SCB. In two level approximation, electrostatic energy is the  $\sigma_z$ , while the Josephson energy is the  $\sigma_x$ . Therefore, we have

$$H_{sys} = \frac{1}{2} \hbar \omega_{10} \sigma_z; \quad (51)$$

$$p_J = -e \sigma_x. \quad (52)$$

From (52) and (49), we have

$$\phi_{R/L}^{out} = \phi_{L/R}^{in} - e \langle \sigma_x \rangle \frac{\tau_{RC}}{C_J}. \quad (53)$$

The  $\langle \sigma_x \rangle$  is derived from the separate subsection. From Eq. (78), we have

$$\langle \sigma_x \rangle = - \frac{2A' \gamma_{10} [\cos \omega_p t + (\delta \omega_p / \gamma_{10}) \sin \omega_p t]}{\gamma_{10}^2 + \delta \omega_p^2 + 2A'^2}, \quad (54)$$

where  $\omega_p$  is the probe frequency,  $\delta \omega_p = \omega_p - \omega_{10}$  is the detuning between probe and 0-1 transition,  $\gamma_{10}$  is the decoherence rate and  $A'$  is the normalized drive amplitude. Substituting (54) into (53), this leads to

$$\phi_{R/L}^{out} = \phi_{L/R}^{in} + \frac{A [\cos \omega_p t + (\delta \omega_p / \gamma_{10}) \sin \omega_p t]}{1 + \delta \omega_p^2 / \gamma_{10}^2 + 2A'^2 / \gamma_{10}^2}, \quad (55)$$

where

$$A = \frac{2e\tau_{RC}}{\gamma_{10} C_J} A', \quad (56)$$

$A$  is the drive amplitude, see the subsection below. Taking the time derivative of (55), and substituting  $\partial_t \phi_{R/L}^{out} = V_{R/L}^{out}$ ,  $\partial_t \phi_{R/L}^{in} = V_{R/L}^{in}$ , Eq. (55) becomes,

$$V_R^{out} = V_L^{in} + \frac{V_d [-\sin \omega_p t + (\delta \omega_p / \gamma_{10}) \cos \omega_p t]}{1 + \delta \omega_p^2 / \gamma_{10}^2 + 2A'^2 / \gamma_{10}^2}, \quad (57)$$

where  $V_p = A \omega_p = V_L^{in}$  is the input voltage drive from the left. Back to the derivation in subsection below, we consider sine part as the input wave, so the sine part can be defined as in phase, and the cosine part is defined as the quadrature signal. The voltage transmission coefficient  $t$  can then be expressed in the following way,

$$\frac{V^{out}}{V^{in}} \equiv t = 1 - \frac{1 - i(\delta \omega_p / \gamma_{10})}{1 + \delta \omega_p^2 / \gamma_{10}^2 + \Omega_p^2 / \gamma_{10}^2}. \quad (58)$$

We also get the reflection coefficient  $r$ ,

$$r = -\frac{1 - i(\delta\omega_p/\gamma_{10})}{1 + \delta\omega_p^2/\gamma_{10}^2 + \Omega_p^2/\gamma_{10}^2}, \quad (59)$$

where

$$\Omega_p = \sqrt{2}A' = \frac{\sqrt{2}eC_c}{2\hbar(C_c + C_J)}V_p; \quad (60)$$

$$\gamma_{10} = \frac{e^2\omega_{10}C_c^2Z_0}{2\hbar(C_c + C_J)^2} = \frac{\Gamma_{10}}{2}, \quad (61)$$

where  $\Gamma_{10}$  and  $\gamma_{10}$  are the 0-1 relaxation rate and 0-1 decoherence rate of the atom, respectively.  $\Omega_p$  is the Rabi frequency.

### Derivation of $\langle\sigma_x\rangle$

Here we follow the derivation [83] in append paper V. Our approach includes the following steps.

1. Apply the Gardiner Zoller notation [84].
2. Derive the master equations.
3. Find the solution for the density matrix in the steady state.
4. Compute  $\langle\sigma_x\rangle$ .

In Gardiner Zoller [84], they consider that a general system with Hamiltonian  $H_{\text{sys}}$ , interacts with a one dimensional electromagnetic field,  $A(t)$ , under influence of a heat bath, which consists of an assembly of harmonics oscillator. The input field and the output field denote as,  $A_{in}(t)$  and  $A_{out}(t)$ , respectively.  $Y$  and  $X$  are the operator of the system that interact with the heat bath. The following section shows Eqs. (48), (49), (50) are equivalent to the Gardiner Zoller Notation [84], GZ in short. We identify the definition of each parameters in [84] corresponding to our system:

$$Y = \phi_J; X = -p_J; H_{SCB} = H_{\text{sys}}, \quad (62)$$

$$A_{in}(t) = \sqrt{\frac{C_0}{2}}\phi^{in}(t); A_{out}(t) = \sqrt{\frac{C_0}{2}}\phi^{out}(t). \quad (63)$$

From GZ (3.2.25), we have the equation of motion for the system operator  $Y$ ,

$$\dot{Y} = \frac{i}{\hbar}[H_{\text{sys}}, Y] + \frac{i}{2\hbar}[\gamma\dot{X} - 2\sqrt{\gamma c}\dot{A}_{in}(t), [X, Y]]_+, \quad (64)$$

where  $c$  is the velocity of light and  $\gamma$  is the damping rate. Substituting the notation above, together using the following commutation relations,  $[\phi_J, p_J] = i\hbar$ ,

$[X, Y] = i\hbar$ , we have

$$\left[ \frac{(C_c V_{DC} + p_J)^2}{2(C_c + C_J)}, \phi_J \right] = -2i\hbar \frac{(C_c V_{DC} + p_J)}{C_c + C_J}. \quad (65)$$

We use the Hamiltonian Eq. (50) and we substitute Eq. (62), Eq. (63) and Eq. (65) into Eq. (64), we get

$$\partial_t \phi_J = \frac{p_J + C_c V_{DC}}{C_c + C_J} + \gamma \partial_t p_J + \sqrt{2\gamma c C_0} \partial_t \phi^{in}(t). \quad (66)$$

If we identify,

$$\gamma = \frac{C_c}{C_c + C_J} \frac{\tau_{RC}}{C_J} = \frac{Z_0}{2} \frac{C_c^2}{(C_c + C_J)^2},$$

this leads to

$$\sqrt{2\gamma c C_0} = \frac{C_c}{C_c + C_J} \sqrt{Z_0 \frac{1}{\sqrt{L_0 C_0}}} C_0 = \frac{C_c}{C_c + C_J}.$$

We recover Eq. (48) from Eq. (66). From GZ (3.2.27), we have

$$A_{out}(t) = A_{in}(t) - \sqrt{\frac{\gamma}{c}} X(t).$$

We substitute this into our identification Eq. (62), (63),

$$\begin{aligned} \sqrt{\frac{C_0}{2}} \phi^{out}(t) &= \sqrt{\frac{C_0}{2}} \phi^{in}(t) + \sqrt{\frac{\frac{C_c^2 Z_0}{2(C_c + C_J)^2}}{\frac{1}{\sqrt{L_0 C_0}}}} p_J; \\ \phi^{out} &= \phi^{in} + 2p_J \frac{\tau_{RC}}{C_J}. \end{aligned} \quad (68)$$

Thus we recover Eq. (49). As I have shown, in Eq. (66) and Eq. (68), making the substitution above Eq. (62), (63), we can map our system onto the system with Hamiltonian  $H_{sys}$ , interacts with a one dimensional electromagnetic field,  $A(t)$ , under influence of a heat bath, which consists of an assembly of harmonics oscillator, discussed in GZ [84].

In our system, we follow the quantum optical case in GZ, page 85. A simplified quantum Langevin equation can be written as,

$$\dot{\rho}(t) = -\frac{i}{\hbar} [H_{sys}, \rho]$$

$$-\frac{1}{\hbar} \sum_m (\gamma_m \omega_m [\rho X_m^+ - X_m^- \rho, X]) + \frac{i}{\hbar} \sqrt{2\gamma_m c C_0} \partial_t \Phi_p [X, \rho],$$

where  $\rho$  is the density matrix of the system. And note that we decomposed the  $X$  operator into eigen-operators of  $H_{sys}$ , that is  $X^+ + X^- = X$ , where  $[H_{sys}, X_m^\pm] = \pm \hbar \omega_m X_m^\pm$ . The first term contains the qubit system, the second term contains the relaxation and the third term contains the driving field. This master equation can be solved in a specific case, say, we consider a two level system,  $m=1$ , driven by the sine voltage wave

$$V = \partial_t \Phi_p = (A\omega_p) \sin \omega_p t,$$

where  $V_p = A\omega_p$ . In two-level approximation, we have

$$H_{sys} = \frac{1}{2} \hbar \omega_{10} \sigma_z;$$

$$X^+ + X^- = X = -p_J = e\sigma_x = e(\sigma^+ + \sigma^-).$$

Here, we assume the SCB limit, where electrostatic energy is in the  $\sigma_z$  direction, while the Josephson energy is in the  $\sigma_x$  direction. Thus, we can arrive to the next master equation associated to the quantum Langevin equation of the SCB transmission line system:

$$\begin{aligned} \dot{\rho}(t) = & -\frac{i\omega_{10}}{2} (\sigma_z \rho - \rho \sigma_z) \\ & + \frac{e^2 \gamma \omega_{10}}{\hbar} (2\sigma^- \rho \sigma^+ - \rho \sigma^+ \sigma^- - \sigma^+ \sigma^- \rho + \sigma^- \rho \sigma^- + \sigma^+ \rho \sigma^+) \\ & + \frac{ie\omega_p \sqrt{2\gamma c C_0}}{\hbar} A \sin(\omega_p t) (\sigma^+ \rho - \rho \sigma^+ + \sigma^- \rho - \rho \sigma^-). \end{aligned}$$

For small damping and small drive amplitude,  $\omega_{10} \gg \gamma, A$ , we can perform the RWA, leading to the following master equation,

$$\begin{aligned} \dot{\rho}(t) = & -\frac{i\omega_{10}}{2} (\sigma_z \rho - \rho \sigma_z) \\ & + \frac{e^2 \gamma \omega_{10}}{\hbar} (2\sigma^- \rho \sigma^+ - \rho \sigma^+ \sigma^- - \sigma^+ \sigma^- \rho) \\ & + \frac{e\omega_p \sqrt{2\gamma c C_0}}{2\hbar} A (e^{-i\omega_p t} (\rho \sigma^+ - \sigma^+ \rho) + e^{i\omega_p t} (\sigma^- \rho - \rho \sigma^-)). \end{aligned}$$

We define the relaxation rate  $\Gamma_{10}$  and the normalized drive amplitude  $A'$

$$\gamma_{10} = \frac{e^2 \gamma \omega_{10}}{\hbar};$$

$$A' = \frac{e\omega_p}{2\hbar} A \sqrt{2\gamma C_0} = \frac{C_J \gamma_{10}}{2e\tau_{RC}} A.$$

Then, the above expressions becomes,

$$\begin{pmatrix} \partial_t \rho_{00} & \partial_t \rho_{01} \\ \partial_t \rho_{10} & \partial_t \rho_{11} \end{pmatrix} = i\omega_{10} \begin{pmatrix} 0 & -\rho_{01} \\ \rho_{10} & 0 \end{pmatrix} + \gamma_{10} \begin{pmatrix} -2\rho_{00} & -\rho_{01} \\ -\rho_{10} & 2\rho_{00} \end{pmatrix} \\ + A' e^{-i\omega_p t} \begin{pmatrix} -\rho_{10} & \rho_{00} - \rho_{11} \\ 0 & \rho_{10} \end{pmatrix} + A' e^{i\omega_p t} \begin{pmatrix} -\rho_{01} & 0 \\ \rho_{00} - \rho_{11} & \rho_{01} \end{pmatrix}.$$

We introduce the following new variables to solve the equations,

$$S^+ = \rho_{01} e^{i\omega_p t}; S^- = \rho_{10} e^{-i\omega_p t}, S^z = \rho_{00} - \rho_{11}. \quad (69)$$

For the steady state, we have

$$\partial_t \rho_{ij} = 0, \quad (70)$$

where  $i, j = 0, 1$ . Using the normalization requirement,  $\rho_{00} + \rho_{11} = 1$ , the master equation becomes,

$$A' S_z - [\gamma_{10} - i(\omega_p - \omega_{10})] S^+ = 0; \quad (71)$$

$$A' S_z - [\gamma_{10} + i(\omega_p - \omega_{10})] S^- = 0; \quad (72)$$

$$\gamma_{10}(1 + S_z) + A'(S^+ + S^-) = 0. \quad (73)$$

We define  $\delta\omega_p = \omega_p - \omega_{10}$  and solve these three equations. We get

$$S^+ = -\frac{A'(\gamma_{10} + i\delta\omega_p)}{\gamma_{10}^2 + \delta\omega_p^2 + 2A'^2}; \quad (74)$$

$$S^- = -\frac{A'(\gamma_{10} - i\delta\omega_p)}{\gamma_{10}^2 + \delta\omega_p^2 + 2A'^2}. \quad (75)$$

Recalling from the definition (69), we finally get the expectation value for  $\sigma_x$ ,

$$\langle \sigma_x \rangle = Tr(\rho \sigma_x) = S^+ e^{-i\omega_p t} + S^- e^{i\omega_p t}; \quad (76)$$

$$\langle \sigma_x \rangle = \cos(\omega_p t)(S^+ + S^-) + i \sin(\omega_p t)(S^- - S^+); \quad (77)$$

$$\langle \sigma_x \rangle = -\frac{2A'\gamma_{10} [\cos \omega_p t + (\delta\omega_p/\gamma_{10}) \sin \omega_p t]}{\gamma_{10}^2 + \delta\omega_p^2 + 2A'^2}. \quad (78)$$

# Appendix D

## $g^{(2)}$ measurements using linear amplifiers

This section follows the notes from Tauno Palomaki, who did the derivation. Fig. 3 shows the notations in this section. The quadratures of the field and the power after amplifier  $i$  are given by

$$I_i = \frac{1}{2}(b_i + b_i^\dagger); \quad Q_i = \frac{1}{2i}(b_i - b_i^\dagger); \quad (79)$$

$$\langle P_i \rangle = (\langle I_i \rangle^2 + \langle Q_i \rangle^2) = \langle b_i^\dagger b_i + 1/2 \rangle. \quad (80)$$

We can express the output operators in terms of the input state and a noise operator:

$$b = \sqrt{G}a + F; \quad b^\dagger = \sqrt{G}a^\dagger + F^\dagger. \quad (81)$$

Since the noise and the signal are not correlated, we have

$$\langle F \rangle = \langle Fa \rangle = \langle Fa^\dagger \rangle = [F, a] = [F, a^\dagger] = 0. \quad (82)$$

The power output from a single amplifier gives,

$$\langle P \rangle = \langle (\sqrt{G}a^\dagger + F^\dagger)(\sqrt{G}a + F) + 1/2 \rangle. \quad (83)$$

Removing terms that average to zero since they are uncorrelated, this leads to

$$\langle P \rangle = \langle Ga^\dagger a + F^\dagger F + 1/2 \rangle. \quad (84)$$

We can measure the covariance of two powers,

$$\langle \Delta P_i \Delta P_j \rangle = \langle P_i P_j \rangle - \langle P_i \rangle \langle P_j \rangle. \quad (85)$$

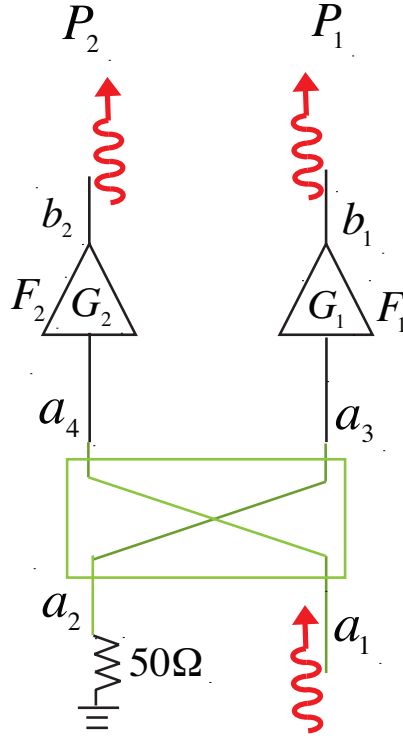


Figure 3:  $P_{i(j)}$  is the power out of amplifier  $i(j)$ .  $b_{i(j)}$  is the annihilation operator after the  $i(j)$  amplifier.  $F_{i(j)}$  is the amplifier noise operator for  $i(j)$ .  $a_3, a_4$  are the annihilation operators after the beam splitter and before the amplifiers.  $G_{i(j)}$  is the gain for amplifier  $i(j)$ .  $a_1$  is the annihilation operator from the signal port of the beam splitter.  $a_2$  is the annihilation operator from the vacuum port ( $50 \Omega$ ) of the beam splitter.

$$\begin{aligned} \langle \Delta P_i \Delta P_j \rangle &= [\langle (b_i^\dagger b_i + 1/2)(b_j^\dagger b_j + 1/2) \rangle - \langle b_i^\dagger b_i + 1/2 \rangle \langle b_j^\dagger b_j + 1/2 \rangle] \\ &= [\langle b_i^\dagger b_i b_j^\dagger b_j \rangle - \langle b_i^\dagger b_i \rangle \langle b_j^\dagger b_j \rangle]. \end{aligned}$$

This gives us 16 terms minus 16 terms. We know that  $a_{3,4}$  is uncorrelated with  $F_{1,2}$ ,  $F_1$  is uncorrelated with  $F_2$ . We can thus remove the following terms:

$$\langle Fa \rangle, \langle Fa^\dagger \rangle, \langle a^\dagger a a^\dagger F \rangle, \langle a^\dagger F a^\dagger F \rangle,$$

and simplify

$$\langle F_i^\dagger F_i a_k^\dagger a_k \rangle = \langle F_i^\dagger F_i \rangle \langle a_k^\dagger a_k \rangle.$$

This leaves

$$\langle \Delta P_1 \Delta P_2 \rangle = G_1 G_2 [\langle a_3^\dagger a_3 a_4^\dagger a_4 \rangle - \langle a_3^\dagger a_3 \rangle \langle a_4^\dagger a_4 \rangle].$$

We can normalize the covariance by dividing this expression by the power of each input:

$$\frac{\langle \Delta P_1 \Delta P_2 \rangle}{[\langle P_1 \rangle - \langle P_{1,N} \rangle][\langle P_2 \rangle - \langle P_{2,N} \rangle]} = \frac{G_1 G_2 [\langle a_3^\dagger a_3 a_4^\dagger a_4 \rangle - \langle a_3^\dagger a_3 \rangle \langle a_4^\dagger a_4 \rangle]}{\langle G_1 a_3^\dagger a_3 \rangle \langle G_2 a_4^\dagger a_4 \rangle},$$

where

$$\langle P_{i,N} \rangle = \langle F_i^\dagger F_i + 1/2 \rangle.$$

The expression becomes,

$$\frac{\langle \Delta P_1 \Delta P_2 \rangle}{[\langle P_1 \rangle - \langle P_{1,N} \rangle][\langle P_2 \rangle - \langle P_{2,N} \rangle]} = \frac{\langle a_3^\dagger a_3 a_4^\dagger a_4 \rangle}{\langle a_3^\dagger a_3 \rangle \langle a_4^\dagger a_4 \rangle} - 1.$$

For a  $90^\circ$  hybrid-coupler (Fig. 4) [81], the expressions for the output fields in terms of the input fields are the same as a 50/50 beam splitter. The operators can then be written as,

$$\begin{pmatrix} a_3 \\ a_4 \end{pmatrix} = \begin{pmatrix} r & t \\ t & r \end{pmatrix} \begin{pmatrix} a_1 \\ a_2 \end{pmatrix} = \frac{1}{\sqrt{2}} \begin{pmatrix} -i & 1 \\ 1 & -i \end{pmatrix} \begin{pmatrix} a_1 \\ a_2 \end{pmatrix}. \quad (86)$$

We know that the second input port is vacuum, this leads to

$$\langle a_1^\dagger a_2 \rangle = \langle a_2^\dagger a_2 \rangle = \langle a_2^\dagger a_1 \rangle = 0.$$

For a 50/50 hybrid coupler, we then have

$$\langle a_3^\dagger a_3 \rangle = \langle a_4^\dagger a_4 \rangle = \langle a_1^\dagger a_1 \rangle / 2.$$

Using the commutation relations  $[a_i, a_j^\dagger] = \delta_{ij}$ , we can simplify the following expression,

$$\begin{aligned} \langle a_3^\dagger a_3 a_4^\dagger a_4 \rangle &= \frac{1}{4} \langle (a_1^\dagger a_1 + i a_1^\dagger a_2 - i a_2^\dagger a_1 + a_2^\dagger a_2)(a_1^\dagger a_1 - i a_1^\dagger a_2 + i a_2^\dagger a_1 + a_2^\dagger a_2) \rangle \\ &= \langle a_1^\dagger a_1^\dagger a_1 a_1 \rangle / 4. \end{aligned}$$

The second-order correlation function can then be defined as,

$$g^{(2)} = 1 + \frac{\langle \Delta P_1 \Delta P_2 \rangle}{[\langle P_1 \rangle - \langle P_{1,N} \rangle][\langle P_2 \rangle - \langle P_{2,N} \rangle]} = \frac{\langle a_1^\dagger a_1^\dagger a_1 a_1 \rangle}{\langle a_1^\dagger a_1 \rangle \langle a_1^\dagger a_1 \rangle}.$$



*Figure 4: A 90° hybrid-coupler used in the experiment.*

# Appendix E

## Fabrication recipes

### Wafer preparation

A 3-inch silicon wafer with native oxide is used to fabricate chips with dimensions of  $5\text{ mm} \times 5\text{ mm}$ . Before any processing, the wafer has to be cleaned by putting it inside the ultrasonic bath with S1165 remover at  $75^{\circ}\text{C}$  for 20 mins. Then, the wafer is rinsed in a bath of isopropanol (IPA), followed by rinsing with deionized water (DI). Finally, we dry the wafer using a flow of nitrogen and perform reactive ion etching using an oxygen ash process with 50W for 30 s.

### Photolithography

To do the photolithography, we spin HMDS Primer on the wafer at 3000 rpm and then baked it on a hotplate at  $110^{\circ}\text{C}$  for 1 min. LOR3B was spun on the wafer at 3000 rpm for 1 min, and then it was baked on a hotplate at  $200^{\circ}\text{C}$  for 5 mins. We then spin S1813 positive photoresist on top of the LOR3B layer at 3000 rpm for 2 mins. Then, we bake it on the hotplate at  $110^{\circ}\text{C}$  for 2 mins. After that, we use the UV 400 nm mask aligner and an optical mask to expose the resist for 35 s at an intensity of  $6\text{ mW}/\text{cm}^2$ . Finally, we develop the resist using MF319 for 40 s and clean it with DI water, drying it with a flow of nitrogen.

### Deposition of the gold pads

The following deposition of gold was performed in a high vacuum chamber using an e-gun evaporator. A 3 nm layer of Ti was served as a sticking layer between the wafer and gold. Then, 90 nm thick gold was deposited on the top of the Ti layer. We want to deposit Al on the gold pads later, in order to prevent the gold and the aluminum from interdiffusing, we also deposit a 10 nm thick layer Pd on of the top of gold. The multilayers are lifted off using Remover 1165 at a temperature of  $75^{\circ}\text{C}$ .

### **Pre-dicing on the backside of the wafer**

We spin a protective resist layer (S1813) on the top of the wafer (2000 rpm) and bake it for 2 minutes at  $110^{\circ}\text{C}$ . This resist layer is used for protection of the gold structure when the wafer is diced. The thickness of the wafer is 380  $\mu\text{m}$ . We pre-cut the wafer into  $5\text{ mm} \times 5\text{ mm}$  array of chips on the backside, the depth of the cut is 120  $\mu\text{m}$ . This makes it easy to separate the chips at a later stage.

### **E-beam lithography**

The e-beam lithography is done with a two layer resist. We spin PMMA EL10 as the bottom layer at 500 rpm for 5 s and 3000 rpm for 45 s, and bake it at  $175^{\circ}\text{C}$  for 5 minutes. We spin the top e-beam resist Zep 520A dissolved 1:1 in anisol, at 2000 rpm for 45 s and bake it with  $150^{\circ}\text{C}$  for 5 minutes. The transmission line, part of the ground plane and the transmon are patterned by e-beam lithography using 10 nA, 70 nA and 1 nA beam currents, respectively. The dose for the resist is  $100\text{ uC/cm}^2$ . After exposure (Fig. 3.1, step 1), the top resist was developed using O-Xylene HPLC 96% for 2 minutes. We then break the wafer into chips along the precuts on the backside. We develop the bottom layer using IPA mixed with DI water in 4:1 proportion until an undercut greater than 0.2  $\mu\text{m}$  emerges. The development time typically is around 6 min. This leads to the formation of suspended bridges, so-called Dolan bridges (Fig. 3.1, step 2). These suspended resist bridges are used for making Josephson junctions below, which are the main components of the transmon.

### **Double angle evaporation of Al**

Before evaporation, we perform an oxygen ash with 50 W for 10 s. We then deposit a 20 nm thick aluminum layer with an angle of  $30^{\circ}$  (Fig. 3.1, step 3) on the chip inside a high vacuum ( $< 5 \times 10^{-7}\text{ mBar}$ ) chamber. Then, we let oxygen into the vacuum chamber. With an  $\text{O}_2$  pressure of 0.2 mBar for 20 minutes (Fig. 3.1, step 4), a few nm aluminum oxide grows on the top of the aluminum. We pump out the oxygen and evaporate 40nm of Al on the aluminum oxide at an angle of  $-30^{\circ}$  (Fig. 3.1, step 5). The Josephson junctions are formed with an overlap area of  $0.16 \times 0.1\ \mu\text{m}^2$ . After this, we use S1165 to remove the resist and the excess Al film at  $75^{\circ}\text{C}$  and rinse in IPA and DI water (Fig. 3.1, step 6). Fig. 3.3 B shows the actual chip made. The yellow ground plane is the gold pad, while the white part is Al.

# Appendix F

## Calculations on Cross-Kerr Effect

### Weak probe limit

According to Eq. 2.87, we have

$$\rho_{20} = A\rho_{10} + B\rho_{21}, \quad (87)$$

where

$$A = \frac{i\Omega_c}{2[\gamma_{20} - i(\delta\omega_p + \delta\omega_c)]};$$

$$B = -\frac{i\Omega_p}{2[\gamma_{20} - i(\delta\omega_p + \delta\omega_c)]}.$$

With a weak probe, where  $\Omega_p \ll \gamma_{10}$ , we can approximate  $\rho_{22} \simeq 0$ ,  $\rho_{11} \simeq 0$ ,  $\rho_{00} \simeq 1$ . From Eq. 2.84, we have

$$\rho_{10} = C\rho_{20} + D, \quad (88)$$

where

$$C = \frac{i\Omega_c/2}{\gamma_{10} - i\delta\omega_p};$$

$$D = \frac{i\Omega_p/2}{\gamma_{10} - i\delta\omega_p}.$$

From Eq. 2.86, we have

$$\rho_{21} = E\rho_{20}, \quad (89)$$

where

$$E = \frac{\Omega_p/2}{\delta\omega_p + i\gamma_{21}}.$$

Combining Eq. 87, 88 and 89, we have

$$\rho_{10} = \frac{ADC}{1 - AC - BE} + D. \quad (90)$$

For a transmon in an open transmission line, according to Eq. (2.92), the complex transmission coefficient for the probe is

$$t_{p,1} = 1 + i \frac{\Gamma_{10} \rho_{10}}{\Omega_p}. \quad (91)$$

Similarly, for a transmon at end of a transmission line, according to Eq. (2.95), the complex reflection coefficient for the probe is

$$r_{p,2} = 1 + 2i \frac{\Gamma_{10} \rho_{10}}{\Omega_p}, \quad (92)$$

The cross-Kerr phase shift is defined as  $\Delta\varphi_{p,i} = \varphi_{p,i}(\Omega_c) - \varphi_{p,i}(\Omega_c = 0)$ , where  $i = 1, 2$ ,  $\varphi_{p,1}(\Omega_c) = \arg(t_{p,1})$ ,  $\varphi_{p,2}(\Omega_c) = \arg(r_{p,2})$ . The only assumption in this section is  $\Omega_p \ll \gamma_{10}$ . All the parameters for the theory include:  $\omega_{10}$ ,  $\omega_{21}$ ,  $\gamma_{20}$ ,  $\gamma_{10}$ ,  $\Gamma_{10}$ ,  $\gamma_{21}$ ,  $k_c$  and  $k_p$ , where  $k_c$  and  $k_p$  are the control and probe field coupling, defined in Table 1. From the single tone and two tone spectroscopy, we can extract  $\omega_{10}$ ,  $\omega_{21}$ ,  $\gamma_{10}$ ,  $\Gamma_{10}$  and  $k_p$ . The theory curve is insensitive to  $\gamma_{21}$ , one can use the theoretical derived value (see Table 1). In summary, the free fitting parameters are  $\gamma_{20}$  and  $k_c$ .

Fig. 5 shows  $r_{p,2}$  as a function of  $P_c$  and  $\omega_p$  for a weak probe. The magnitudes  $|r_{p,2}|$  and phase  $\Delta\varphi_{p,2}$  response are shown in Fig. 5A and B, respectively.

Fig. 4.15C shows  $\Delta\varphi_p$  as a function of  $\langle N_c \rangle$  for a weak probe at a probe frequency that maximizes the probe phase shift. Fig. 6B shows the corresponding magnitude response for Sample 1a.

### Control field at Single-Photon Level

In this section we depart from the approximations made above and treat the system in the regime where the control field is considered to be at the single-photon level, but the probe field is arbitrary. In this case, we solve the master equation in the steady state, the  $\rho_{10}$  depends on the full set of physical parameters,  $\omega_{10}$ ,  $\omega_{21}$ ,  $\Omega_p$ ,  $\Omega_c$ ,  $\Gamma_{\phi,ij}$ ,  $\gamma_{ij}$ ,  $\Gamma_{ij}$ , where  $i, j = 0, 1, 2$  and  $j > i$ , in total, 13 parameters. Note that  $\omega_{10}$ ,  $\omega_{21}$ ,  $\Gamma_{\phi,10}$ ,  $\Gamma_{10}$  can be measured from single-tone, two-tone spectroscopy. Some parameters can be derived according to Table 1. This leaves  $\gamma_{20}$ ,  $k_c$  and  $k_p$  as free parameters which has been fitted to the data in Fig. 4.15B and Fig. 6A.

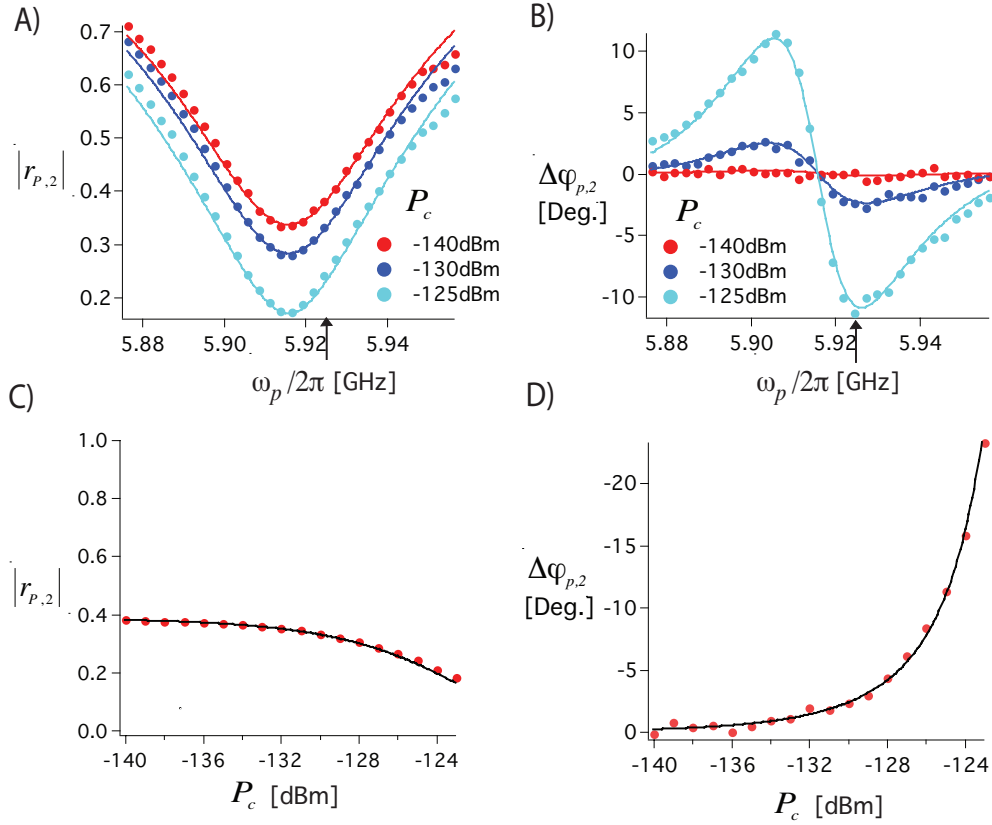


Figure 5:  $r_{p,2}$  as a function of  $P_c$  and  $\omega_p$  for low probe powers, where  $\Omega_p \ll \gamma_{10}$  in Sample 2. A)  $|r_{p,2}|$  for three different values of  $P_c$ . B) Corresponding phase response,  $\Delta\varphi_{p,2}$ . C)  $|r_{p,2}|$  as a function of  $P_c$  for  $\delta\omega_p = 9$  MHz, indicated by the arrow in (A). The arrow also indicates the maximal phase shift in (B). D) The phase response corresponding to the data in C. All the markers are experimental data. Solid curves are the theory fits based on Eq. 92. The theory curves are fitted simultaneously to extract the parameters in Table 4.2 Sample 2. Plot C) and D) are displayed in the units of  $\langle N_c \rangle$  in Fig. 4.15 C and D, respectively.

Parameters	Expression
$\gamma_{10}$	$\Gamma_{10}/2+\Gamma_{\phi,10}$
$\Gamma_{21}$	$2\Gamma_{10}$
$\Gamma_{\phi,21}$	$\Gamma_{\phi,10}$
$\gamma_{21}$	$\Gamma_{21}/2+\Gamma_{20}/2+\Gamma_{10}/2+\Gamma_{\phi,21}$
$\Gamma_{20}$	0
$\Gamma_{\phi,20}$	$\gamma_{20}-\Gamma_{20}/2-\Gamma_{21}/2$
$\Omega_p$	$k_p \times 10^{P_p/20}$
$\Omega_c$	$k_c \times 10^{P_c/20}$

Table 1: Expressions for different parameters. The blue, black and red coding represent measured, derived and fitted parameters, respectively. Note that  $P_c$  and  $P_p$  are given in dBm. We consider the main noise source to be flux noise. We have  $\Gamma_{\phi,21} \simeq \Gamma_{\phi,10}$  [66].

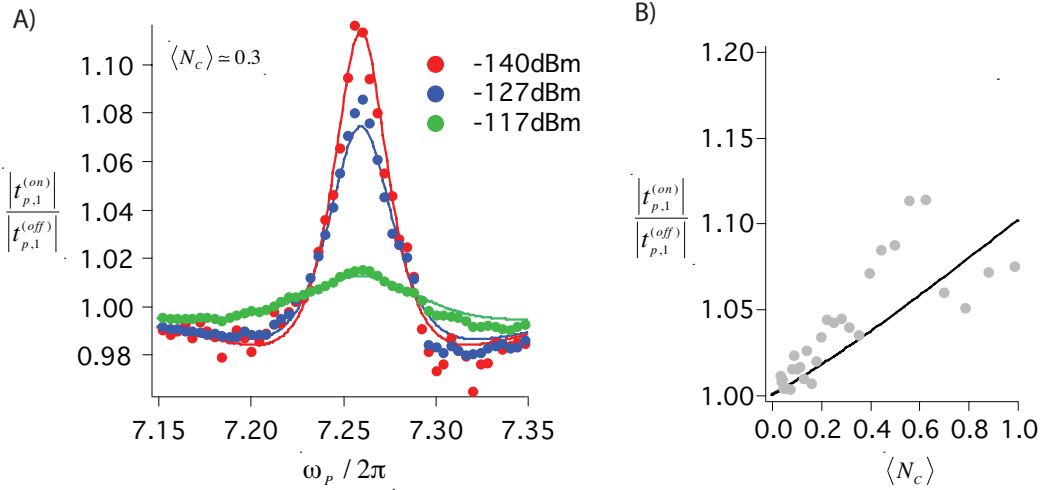


Figure 6: Probe response,  $|t_{p,1}^{(on)}|/|t_{p,1}^{(off)}|$ , induced by a weak control pulse for Sample 1a. A) Magnitude corresponds to the phase response in Fig. 4.15B, with the same parameters. B) Magnitude corresponds to the phase response in Fig. 4.15C, with the same parameters.

# Acknowledgements

This exciting work took place at Experimental Mesoscopic Physics Group, Quantum Device Physics Laboratory, Microtechnology and Nanoscience Department, Chalmers University of Technology, Gothenburg, Sweden from 2008 to 2013. I have been fortunate to work in the group.

I would like to thank my supervisor Per Delsing for giving me such a fantastic project, guidance, encouragement, discussion and careful reading of my thesis and our papers. And thanks my co-supervisor, Chris Wilson, for enduring support, guidance, help on the Lab, sharing his knowledge, discussion, encouragement and careful reading of my thesis and our papers. More importantly, I acknowledge that Per and Chris helped me to grow as a person as well as a scientist over last 5 years.

Thanks to Göran Johansson, Lars Tornberg, Anton Frisk Kockum, Joel Lindkvist, Borja Peropadre and Sankar Sathyamoorthy for derivation of the theory behind this project and give me support on understanding the theory. Especially, I would like to acknowledge Lars and Anton for careful reading the theory section of my thesis.

Thanks to Tauno Palomaki, Fredrik Persson and Martin Sandberg, for helping me getting started at the early stage of the project.

I would like to thank Bixuan Fan, Thomas Stace and Gerard Milburn for hosting me during my visit to the University of Queensland, Australia. I also want to thank Tim Duty for fruitful discussion during my visit to University of New South Wales, Australia.

I also want to thank all people in the QDP Lab: Arsalan Pourkabirian, Philip Krantz, Simon Abay, Martin Gustafsson, Michaël Simoen, Thilo Bauch, Samuel Lara Avila, Matthias Staudt, Mathieu Pierre, Jan Jacobsson, Jie Sun, Jalali Jafari Behdad, Reza Baghdadi, Ida-Maria Svensson and all the others in the group.

Last but not least, thanks to my parents, sister, brother and my girl friend for enduring support.

# Bibliography

- [1] R. P. Feynman. Simulating physics with computers. *International Journal of Theoretical Physics*, 21:467, 1982.
- [2] D. Deutsch. Quantum theory, the church-turing principle and the universal quantum computer. *Proceedings of The Royal Society of London, Series A*, 400:97, 1985.
- [3] P. W. Shor. Algorithms for quantum computation: discrete logarithms and factoring. *Proceedings of 35th Annual Symposium on Foundations of Computer Science*, page 124, 1994.
- [4] P. W. Shor. Scheme for reducing decoherence in quantum computer memory. *Physical Review A*, 52:R2493, 1995.
- [5] L. K. Grover. A fast quantum mechanical algorithm for database search. *Proceedings of the twenty-eighth annual ACM symposium on Theory of computing*, page 212, 1996.
- [6] D. P. DiVincenzo. The physical implementation of quantum computation. *Fortschritte der Physik*, 48:771, 2000.
- [7] M. A. Nielsen and I. L. Chuang. *Quantum Computation and Quantum Information*. Cambridge University Press, 2000.
- [8] J. J. Sakurai. *Modern quantum mechanics*. Addison-Wesley, 1994.
- [9] J. Bardeen, L. N. Cooper, and J. R. Schrieffer. Theory of superconductivity. *Physical Review*, 108:1175, 1957.
- [10] H. K. Onnes. The resistance of pure mercury at helium temperatures. *Commun. Phys. Lab. Univ. Leiden*, 12:120, 1911.
- [11] W. Meissner and R. Ochsenfeld. Ein neuer effekt bei eintritt der supraleitfähigkeit. *Die Naturwissenschaften*, 21:787, 1933.

- 
- [12] F. London and H. London. Electromagnetic equations of the superconductor. *Proceedings of the Royal Society of London*, 149A:71, 1935.
- [13] B. D. Josephson. Possible new effects in superconductive tunnelling. *Physics Letters*, 1:251, 1962.
- [14] J. G. Bednorz and K. A. Müller. Possible high  $T_c$  superconductivity in the Ba-La-Cu-O system. *Z. Physik B*, 64:189, 1986.
- [15] B. D. Josephson. Coupled superconductors. *Reviews of Modern Physics*, 36:216, 1964.
- [16] M. Tinkham. *Introduction to Superconductivity*. Dover Publications Inc, 2004.
- [17] R. Jaklevic. Quantum interference effects in Josephson tunneling. *Physical Review Letters*, 12:159, 1964.
- [18] M. H. Devoret. Linneaus summer school in quantum engineering. 2010.
- [19] Y. Nakamura, Yu. A. Pashkin, and J. S. Tsai. Coherent control of macroscopic quantum states in a single-Cooper-pair box. *Nature*, 398:786, 1999.
- [20] A. Wallraff, D. I. Schuster, A. Blais, L. Frunzio, R. S. Huang, J. Majer, S. Kumar, S. M. Girvin, and R. J. Schoelkopf. Strong coupling of a single photon to a superconducting qubit using circuit quantum electrodynamics. *Nature*, 431:162, 2004.
- [21] M. Hofheinz, H. Wang, M. Ansmann, R. C. Bialczak, E. Lucero, M. Neeley, A. D. O'Connell, D. Sank, J. Wenner, J. M. Martinis, and A. N. Cleland. Synthesizing arbitrary quantum states in a superconducting resonator. *Nature*, 459:546, 2009.
- [22] O. Astafiev, A. M. Zagoskin, A. A. Abdumalikov, Y. A. Pashkin, T. Yamamoto, K. Inomata, Y. Nakamura, and J. S. Tsai. Resonance fluorescence of a single artificial atom. *Science*, 327:840, 2010.
- [23] D. Ristè, C. C. Bultink, M. J. Tiggelman, R. N. Schouten, K. W. Lehnert, and L. DiCarlo. Millisecond charge-parity fluctuations and induced decoherence in a superconducting transmon qubit. *Nature communications*, 4:1913, 2013.
- [24] V. Sandoghdar. Stockholm summer school on quantum optics and nanophotonics. 2010.

- 
- [25] R. J. Schoelkopf and S. M. Girvin. Wiring up quantum systems. *Nature*, 451:664, 2008.
- [26] J. Clarke and F. K. Wilhelm. Superconducting quantum bits. *Nature*, 453:1031, 2008.
- [27] G. Wendin and V. S. Shumeiko. Quantum bits with josephson junctions. *Low Temperature Physics*, 33:724, 2007.
- [28] J. M. Martinis, M. H. Devoret, and J. Clarke. Energy-level quantization in the zero-voltage state of a current-biased josephson junction. *Physical Review Letters*, 55:1543, 1985.
- [29] M. H. Devoret, J. M. Martinis, and J. Clarke. Measurements of macroscopic quantum tunneling out of the zero-voltage state of a current-biased josephson junction. *Physical Review Letters*, 55:1908, 1985.
- [30] D. Vion, A. Aassime, A. Cottet, P. Joyez, H. Pothier, C. Urbina, D. Esteve, and M. H. Devoret. Manipulating the quantum state of an electrical circuit. *Science*, 296:886, 2002.
- [31] D. I. Schuster, A. A. Houck, J. A. Schreier, A. Wallraff, J. M. Gambetta, A. Blais, L. Frunzio, J. Majer, B. Johnson, M. H. Devoret, S. M. Girvin, and R. J. Schoelkopf. Resolving photon number states in a superconducting circuit. *Nature*, 445:515, 2007.
- [32] O. Astafiev, K. Inomata, A. O. Niskanen, T. Yamamoto, Y. Nakamura Yu. A. Pashkin and, and J. S. Tsai. Single artificial-atom lasing. *Nature*, 449:588, 2007.
- [33] M. D. Reed, L. DiCarlo, S. E. Nigg, L. Sun, L. Frunzio, S. M. Girvin, and R. J. Schoelkopf. Realization of three-qubit quantum error correction with superconducting circuits. *Nature*, 482:382, 2012.
- [34] A. Fedorov, L. Steffen, M. Baur, M. P. da Silva, and A. Wallraff. Implementation of a toffoli gate with superconducting circuits. *Nature*, 481:7280, 2011.
- [35] R. Vijay, C. Macklin, D. H. Slichter, S. J. Weber, K. W. Murch, R. Naik, A. N. Korotkov, and I. Siddiqi. Stabilizing rabi oscillations in a superconducting qubit using quantum feedback. *Nature*, 490:77, 2012.
- [36] M. Mariantoni, H. Wang, T. Yamamoto, M. Neeley, R. C. Bialczak, Y. Chen, M. Lenander, E. Lucero, A. D. O’Connell, D. Sank, M. Weides, J. Wenner, Y. Yin, J. Zhao, A. N. Korotkov, A. N. Cleland, and J. M.

- Martinis. Implementing the quantum von neumann architecture with superconducting circuits. *Science*, 334:61, 2011.
- [37] C. M. Wilson, G. Johansson, A. Pourkabirian, M. Simoen, J. R. Johansson, T. Duty, F. Nori, and P. Delsing. Observation of the dynamical Casimir effect in a superconducting circuit. *Nature*, 479:367, 2011.
- [38] M. A. Castellanos-Beltran, K. D. Irwin, G. C. Hilton, L. R. Vale, and K. W. Lehnert. Amplification and squeezing of quantum noise with a tunable josephson metamaterial. *Nature Physics*, 4:929, 2008.
- [39] N. Bergeal, F. Schackert, M. Metcalfe, R. Vijayand, V. E. Manucharyan, L. Frunzio, D. E. Prober, R. J. Schoelkopf, S. M. Girvin, and M. H. Devoret. Phase-preserving amplification near the quantum limit with a Josephson ring modulator. *Nature*, 465:64, 2010.
- [40] M. Sandberg, F. Persson, I.-C. Hoi, C. M. Wilson, and P. Delsing. Exploring circuit quantum electrodynamics using a widely tunable superconducting resonator. *Physica Scripta*, T137:014018, 2009.
- [41] M. Sandberg, C. M. Wilson, F. Persson, T. Bauch, G. Johansson, V. Shumeiko, T. Duty, and P. Delsing. Tuning the field in a microwave resonator faster than the photon lifetime. *Applied Physics Letters*, 92:203501, 2008.
- [42] M. Wallquist, V. S. Shumeiko, and G. Wendin. Selective coupling of superconducting charge qubits mediated by a tunable stripline cavity. *Physical Review B*, 74:224506, 2006.
- [43] A. Palacios-Laloy, F. Nguyen, F. Mallet, P. Bertet, D. Vion, and D. Esteve. Tunable resonators for quantum circuits. *J Low Temp Phys*, 151:1034, 2008.
- [44] M. K. Tey, Z. L. Chen, S. A. Aljunid, B. Chng, F. Huber, G. Maslennikov, and C. Kurtsiefer. Strong interaction between light and a single trapped atom without the need for a cavity. *Nature Physics*, 4:924, 2008.
- [45] J. Hwang, M. Pototschnig, R. Lettow, G. Zumofen, A. Renn, S. Gotzinger, and V. Sandoghdar. A single-molecule optical transistor. *Nature*, 460:76, 2009.
- [46] G. Wrigge, I. Gerhardt, J. Hwang, G. Zumofen, and V. Sandoghdar. Efficient coupling of photons to a single molecule and the observation of its resonance fluorescence. *Nature Physics*, 4:60, 2008.

- [47] I. Gerhardt, G. Wrigge, P. Bushev, G. Zumofen, M. Agio, R. Pfab, and V. Sandoghdar. Strong extinction of a laser beam by a single molecule. *Physical Review Letters*, 98:033601, 2007.
- [48] J. T. Shen and S. H. Fan. Coherent single photon transport in a one-dimensional waveguide coupled with superconducting quantum bits. *Physical Review Letters*, 95:213001, 2005.
- [49] D. E. Chang, A. S. Sorensen, E. A. Demler, and M. D. Lukin. A single-photon transistor using nanoscale surface plasmons. *Nature Physics*, 3:807, 2007.
- [50] O. V. Astafiev, A. A. Abdumalikov, A. M. Zagoskin, Y. A. Pashkin, Y. Nakamura, and J. S. Tsai. Ultimate on-chip quantum amplifier. *Physical Review Letters*, 104:183603, 2010.
- [51] A. A. Abdumalikov, O. Astafiev, A. M. Zagoskin, Y. A. Pashkin, Y. Nakamura, and J. S. Tsai. Electromagnetically induced transparency on a single artificial atom. *Physical Review Letters*, 104:193601, 2010.
- [52] A. A. Abdumalikov, O. V. Astafiev, Yu. A. Pashkin, Y. Nakamura, and J. S. Tsai. Dynamics of coherent and incoherent emission from an artificial atom in a 1D space. *Physical Review Letters*, 107:043604, 2011.
- [53] I.-C. Hoi, C.M. Wilson, G. Johansson, T. Palomaki, B. Peropadre, and P. Delsing. Demonstration of a single-photon router in the microwave regime. *Physical Review Letters*, 107:073601, 2011.
- [54] I.-C. Hoi, T. Palomaki, G. Johansson, J. Lindkvist, P. Delsing, and C. M. Wilson. Generation of nonclassical microwave states using an artificial atom in 1D open space. *Physical Review Letters*, 108:263601, 2012.
- [55] I.-C. Hoi, A. F. Kockum, T. Palomaki, T. M. Stace, B. Fan, L. Tornberg, S. R. Sathyamoorthy, G. Johansson, P. Delsing, and C.M. Wilson. Giant cross-Kerr effect for propagating microwaves induced by an artificial atom. *Physical Review Letters*, 111:053601, 2013.
- [56] I.-C. Hoi, C. M. Wilson, G. Johansson, J. Lindkvist, B. Peropadre, T. Palomaki, and P. Delsing. Microwave quantum optics with an artificial atom in one-dimensional open space. *New Journal of Physics*, 15:025011, 2013.
- [57] K. Koshino, H. Terai, K. Inomata, T. Yamamoto, W. Qiu, Z. Wang, and Y. Nakamura. Observation of the three-state dressed states in circuit quantum electrodynamics. *Physical Review Letters*, 110:263601, 2013.

- [58] V. Scarani. The security of practical quantum key distribution. *Reviews of Modern Physics*, 81:1301, 2009.
- [59] H. J. Kimble. The quantum internet. *Nature*, 453:1023, 2008.
- [60] K. Lehnert, K. Bladh, L. F. Spietz, D. Gunnarsson, D. I. Schuster, P. Delsing, and R. J. Schoelkopf. Measurement of the excited-state lifetime of a microelectronic circuit. *Physical Review Letters*, 90:027002, 2003.
- [61] K. Bladh, T. Duty, D. Gunnarsson, and P. Delsing. The single Cooper-pair box as a charge qubit. *New Journal of Physics*, 7:180, 2005.
- [62] T. Duty, D. Gunnarsson, K. Bladh, and P. Delsing. Coherent dynamics of a Josephson charge qubit. *Physical Review B*, 69:140503, 2004.
- [63] Y. Nakamura, Yu. A. Pashkin, and J. S. Tsai. Rabi oscillations in a Josephson-junction charge two-level system. *Physical Review Letters*, 87:246601, 2001.
- [64] V. Bouchiat, D. Vion, P. Joyez, D. Esteve, and M. H. Devoret. Quantum coherence with a single Cooper pair. *Physica Scripta*, T76:165, 1998.
- [65] M. Büttiker. Zero-current persistent potential drop across small-capacitance Josephson junctions. *Physical Review B*, 36:3548, 1987.
- [66] J. Koch, T. M. Yu, J. Gambetta, A. A. Houck, D. I. Schuster, J. Majer, A. Blais, M. H. Devoret, S. M. Girvin, and R. J. Schoelkopf. Charge-insensitive qubit design derived from the Cooper pair box. *Physical Review A*, 76:042319, 2007.
- [67] L. DiCarlo, M. D. Reed, L. Sun, B. R. Johnson, J. M. Chow, J. M. Gambetta, L. Frunzio, S. M. Girvin, M. H. Devoret, and R. J. Schoelkopf. Preparation and measurement of three-qubit entanglement in a superconducting circuit. *Nature*, 467:574, 2010.
- [68] A. A. Houck, D. I. Schuster, J. M. Gambetta, J. A. Schreier, B. R. Johnson, J. M. Chow, L. Frunzio, J. Majer, M. H. Devoret, S. M. Girvin, and R. J. Schoelkopf. Generating single microwave photons in a circuit. *Nature*, 449:328, 2007.
- [69] J. M. Fink, M. Goeppl, M. Baur, R. Bianchetti, P. J. Leek, A. Blais, and A. Wallraff. Climbing the Jaynes-Cummings ladder and observing its square root of  $n$  nonlinearity in a cavity QED system. *Nature*, 454:315, 2009.

- [70] A. Fragner, M. Goppl, J. M. Fink, M. Baur, R. Bianchetti, P. J. Leek, A. Blais, and A. Wallraff. Resolving vacuum fluctuations in an electrical circuit by measuring the lamb shift. *Science*, 322:1357, 2008.
- [71] L. S. Bishop, J. M. Chow, J. Koch, A. A. Houck, M. H. Devoret, E. Thuneberg, S. M. Girvin, and R. J. Schoelkopf. Nonlinear response of the vacuum Rabi resonance. *Nature Physics*, 9:105, 2009.
- [72] M. Ansmann, H. Wang, R. C. Bialczak, M. Hofheinz, E. Lucero, M. Neeley, A. D. O’Connell, D. Sank, M. Weides, J. Wenner, A. N. Cleland, and J. M. Martinis. Violation of Bell’s inequality in Josephson phase qubits. *Nature*, 461:504, 2009.
- [73] V. E. Manucharyan, J. Koch, L. I. Glazman, and M. H. Devoret. Fluxonium: Single Cooper-pair circuit free of charge offsets. *Science*, 326:113, 2009.
- [74] D. Vion, A. Aassime, A. Cottet, P. Joyez, H. Pothier, C. Urbina, D. Esteve, and M. H. Devoret. Manipulating the quantum state of an electrical circuit. *Science*, 296:886, 2010.
- [75] J. M. Martinis, K. B. Cooper, R. McDermott, M. Steffen, M. Ansmann, K. D. Osborn, K. Cicak, S. Oh, D. P. Pappas, R. W. Simmonds, and C. C. Yu. Decoherence in Josephson qubits from dielectric loss. *Physical Review Letters*, 95:210503, 2005.
- [76] F. Bloch. Nuclear induction. *Physical Review*, 70:460, 1946.
- [77] P. A. M. Dirac. The quantum theory of the emission and absorption of radiation. *Proceedings of the Royal Society of London. Series A*, 114:243, 1927.
- [78] T. Duty, K. Bladh, D. Gunnarsson, and P. Delsing. Measurements of decoherence times in a Josephson charge qubit using fast pulses. *Journal of Low Temperature Physics*, 136:453, 2004.
- [79] J. A. Schreier, A. A. Houck, J. Koch, D. I. Schuster, B. R. Johnson, J. M. Chow, J. M. Gambetta, J. Majer, L. Frunzio, M. H. Devoret, S. M. Girvin, and R. J. Schoelkopf. Suppressing charge noise decoherence in superconducting charge qubits. *Physical Review B*, 77:180502, 2008.
- [80] J. Mathews and R. L. Walker. *Mathematical methods of physics*. Addison Wesley, 1964.
- [81] D. M. Pozar. *Microwave engineering*. J. Wiley, 2005.

- 
- [82] C. C. Gerry and P. L. Knight. *Introductory Quantum Optics*. Cambridge University Press, 2005.
- [83] B. Peropadre, J. Lindkvist, I.-C. Hoi, C.M. Wilson, J. Garcia-Ripoll, P. Delsing, and G. Johansson. Scattering of coherent states on a single artificial atom. *New Journal of Physics*, 15:03500, 2013.
- [84] C. W. Gardiner and P. Zoller. *Quantum Noise*. Springer, 2004.
- [85] G. Johansson and T. Bauch. *Decoherence and the Bloch equations*. A lecture in Quantum Informatics, 2012.
- [86] J. Grynberg and G. Cohen-Tannoudji. *Atom-Photon Interactions*. Wiley, New York, 1992.
- [87] G. Johansson and T. Bauch. *Quantized electromagnetic field and the Jaynes-Cummings Hamiltonian*. A lecture in Quantum Informatics, 2008.
- [88] C. Wilson, T. Duty, F. Persson, M. Sandberg, G. Johansson, and P. Delsing. Coherence times of dressed states of a superconducting qubit under extreme driving. *Physical Review Letters*, 98:257003, 2007.
- [89] B. R. Mollow. Power spectrum of light scattered by two-level systems. *Physical Review*, 188:1969, 1969.
- [90] M. Baur, S. Filipp, R. Bianchetti, J. M. Fink, M. Goppl, L. Steffen, P. J. Leek, A. Blais, and A. Wallraff. Measurement of Autler-Townes and Mollow transitions in a strongly driven superconducting qubit. *Physical Review Letters*, 102:243602, 2009.
- [91] K. Koshino and Y. Nakamura. Control of the radiative level shift and linewidth of a superconducting artificial atom through a variable boundary condition. *New Journal of Physics*, 14:043005, 2012.
- [92] Bixuan Fan, A. F. Kockum, J. Combes, G. Johansson, I.-C. Hoi, C. M. Wilson, P. Delsing, G. J. Milburn, and T. M. Stace. Breakdown of the cross-Kerr scheme for photon counting. *Physical Review Letters*, 110:053601, 2012.
- [93] L. Slodicka, G. Hetet, S. Gerber, M. Hennrich, and R. Blatt. Electromagnetically induced transparency from a single atom in free space. *Physical Review Letters*, 105:153604, 2010.

- 
- [94] Q. A. Turchette, C. J. Hood, W. Lange, H. Mabuchi, and H. J. Kimble. Measurement of conditional phase shifts for quantum logic. *Physical Review Letters*, 75:4710, 1995.
- [95] G. J. Milburn. Quantum optical Fredkin gate. *Physical Review Letters*, 62:2124, 1989.
- [96] K. J. Resch, J. S. Lundeen, and A. M. Steinberg. Conditional-phase switch at the single-photon level. *Physical Review Letters*, 89:037904, 2002.
- [97] E. A. Tholen, A. Ergül, E. M. Doherty, F. M. Weber, F. Gregis, and D. B. Haviland. Nonlinearities and parametric amplification in superconducting coplanar waveguide resonators. *Applied Physics Letters*, 90:253509, 2007.
- [98] P. Grangier, J. A. Levenson, and J.-P. Poizat. Quantum non-demolition measurements in optics. *Nature*, 396:537, 1998.
- [99] Sankar R. Sathyamoorthy, L. Tornberg, Anton F. Kockum, Ben Q. Baragiola, Joshua Combes, C.M. Wilson, Thomas M. Stace, and G. Johansson. Quantum nondemolition detection of a propagating microwave photon. <http://arxiv.org/pdf/1308.2208>, 2013.
- [100] R. H. Brown and R. Q. Twiss. Correlation between photons in two coherent beams of light. *Nature*, 177:27, 1956.
- [101] M. Barth. Lecture for ESONN. 2010.
- [102] R. Loudon. *The Quantum Theory of Light*. Oxford science publications, 2010.
- [103] D. Bozyigit, C. Lang, L. Steffen, J. M. Fink, C. Eichler, M. Baur, R. Bianchetti, P. J. Leek, S. Filipp, M. P. da Silva, A. Blais, and A. Wallraff. Antibunching of microwave-frequency photons observed in correlation measurements using linear detectors. *Nature Physics*, 7:154, 2011.
- [104] H. Zheng, D. J. Gauthier, and H. U. Baranger. Waveguide QED: Many-body bound-state effects in coherent and Fock-state scattering from a two-level system. *Physical Review A*, 82:063816, 2010.
- [105] J. B. Majer. *Superconducting Quantum Circuits*. PhD thesis, Delft University, 2002.
- [106] M. Sandberg. *Fast-tunable resonators and quantum electrical circuits*. PhD thesis, Chalmers University of Technology, 2009.

- [107] S. A. Campbell. *The science and engineering of microelectronic fabrication*. Oxford University Press, 2001.
- [108] C. M. Caves. Quantum limits on noise in linear amplifiers. *Physical Review D*, 26:1817, 1982.
- [109] Lafe Spietz, K. W. Lehnert, I. Siddiqi, and R. J. Schoelkopf. Primary electronic thermometry using the shot noise of a tunnel junction. *Science*, 300:1929, 2003.
- [110] G. Zumofen, N. M. Mojarad, V. Sandoghdar, and M. Agio. Perfect reflection of light by an oscillating dipole. *Physical Review Letters*, 101:180404, 2008.
- [111] S. H. Autler and C. H. Townes. Stark effect in rapidly varying fields. *Physical Review*, 100:703, 1955.
- [112] F. Mallet, M. A. Castellanos-Beltran, H. S. Ku, S. Glancy, E. Knill, K. D. Irwin, G. C. Hilton, L. R. Vale, and K. W. Lehnert. Quantum state tomography of an itinerant squeezed microwave field. *Physical Review Letters*, 106:220502, 2011.
- [113] C. M. Wilson, T. Duty, M. Sandberg, F. Persson, V. Shumeiko, and P. Delsing. Photon generation in an electromagnetic cavity with a time-dependent boundary. *Physical Review Letters*, 105:233907, 2010.
- [114] N. Matsuda, R. Shimizuand, Y. Mitsumori, H. Kosaka, and K. Edamatsu. Observation of optical-fibre Kerr nonlinearity at the single-photon level. *Nature Photonics*, 3:95, 2009.
- [115] V. Venkataraman, K. Saha, and A. L. Gaeta. Phase modulation at the few-photon level for weak-nonlinearity-based quantum computing. *Nature Photonics*, 7:138, 2013.
- [116] H. Schmidt and A. Imamoglu. Giant Kerr nonlinearities obtained by electromagnetically induced transparency. *Optics Letters*, 21:1936, 1996.
- [117] W. J. Munro, Kae Nemoto, R. G. Beausoleil, and T. P. Spiller. High-efficiency quantum-nondemolition single-photon-number-resolving detector. *Physical Review A*, 71:033819, 2005.
- [118] S. Rebic, J. Twamley, and G. J. Milburn. Giant Kerr nonlinearities in circuit quantum electrodynamics. *Physical Review Letters*, 103:150503, 2009.

- [119] S. J. Srinivasan, A. J. Hoffman, J. M. Gambetta, and A. A. Houck. Tunable coupling in circuit quantum electrodynamics using a superconducting charge qubit with a V-shaped energy level diagram. *Physical Review Letters*, 106:083601, 2011.
- [120] J. M. Gambetta, A. A. Houck, and A. Blais. Superconducting qubit with purcell protection and tunable coupling. *Physical Review Letters*, 106:030502, 2011.
- [121] K. W. Murch, S. J. Weber, K. M. Beck, E. Ginossar, and I. Siddiqi. Reduction of the radiative decay of atomic coherence in squeezed vacuum. *Nature*, 499:62, 2013.
- [122] D. Witthaut and A. S. Sorensen. Photon scattering by a three-level emitter in a one-dimensional waveguide. *New Journal of Physics*, 12:043052, 2010.
- [123] M. V. Gustafsson, P. V. Santos, G. Johansson, and P. Delsing. Local probing of propagating acoustic waves in a gigahertz echo chamber. *Nature Physics*, 8:338, 2012.
- [124] Y. Kubo, C. Grezes, A. Dewes, T. Umeda, J. Isoya, H. Sumiya, N. Morishita, H. Abe, S. Onoda, T. Ohshima, V. Jacques, A. Dréau, J.-F. Roch, I. Diniz, A. Auffeves, D. Vion, D. Esteve, and P. Bertet. Hybrid quantum circuit with a superconducting qubit coupled to a spin ensemble. *Physical Review Letters*, 107:220501, 2011.
- [125] D. Schuster, A. P. Sears, E. Ginossar, L. DiCarlo, L. Frunzio, J. J. L. Morton, H. Wu, G. A. D. Briggs, B. B. Buckley, D. D. Awschalom, and R. J. Schoelkopf. High-cooperativity coupling of electron-spin ensembles to superconducting cavities. *Physical Review Letters*, 105:140501, 2010.
- [126] H. Wu, R. E. George, J. H. Wesenberg, K. Molmer, D. I. Schuster, R. J. Schoelkopf, K. M. Itoh, A. Ardavan, J. J. L. Morton, and G. A. D. Briggs. Storage of multiple coherent microwave excitations in an electron spin ensemble. *Physical Review Letters*, 105:140503, 2010.
- [127] M. U Staudt, I.-C. Hoi, P. Krantz, M. Sandberg, M. Simoen, P. Bushev, N. Sangouard, M. Afzelius, V. S. Shumeiko, G. Johansson, P. Delsing, and C. M. Wilson. Coupling of an Erbium spin ensemble to a superconducting resonator. *Journal of Physics B: At. Mol. Opt. Phys.*, 45:124019, 2012.
- [128] S. K. Dutta. *Characterization of Josephson Devices for use in Quantum Computation*. PhD thesis, University of Maryland, 2006.